NUMERICAL STUDY OF PLUNGING WAVE

IN DEEP WATER

DAO MY HA

(M.Eng., SMA, NUS)

A THESIS SUBMITTED

FOR THE DEGREE OF DOCTOR OF PHILOSOPHY

DEPARTMENT OF CIVIL ENGINEERING

NATIONAL UNIVERSITY OF SINGAPORE

2010

Acknowledgements

I would like to convey my special thanks to my supervisor, Professor Chan Eng Soon. Prof. Chan has been there with me through numerous discussions on this challenging topic. His continuous guidance and valuable advices through the years are deeply appreciated. My research work would not have been possible without the supervision and direction given by him.

My second supervisor, A.Prof. Pavel Tkalich, has been playing an important role in my research pursuance. Without his guidance and encouragement, the completion of this research work might have been much more difficult. I would like to thank him for what he has done for me.

I would like to say 'thank you" to my friends, my colleagues at Tropical Marine Science Institute, especially the "IT guys", for having been always supporting me in numerous ways, helping me with those heavy tasks running on Linux clusters.

I'm deeply thankful to my family who has been by my side all the time, encouraged me in the most stressful and desperate moments. Mum and dad have been caring about me, loving me, giving me strength to pursue my work. Sincere thanks to my loving wife for her understanding throughout the years. Stress is always there at work, and sometimes was brought home unknowingly. Without her sympathy and encouragement, this work would have been thousand times more difficult. With the birth of my little daughter two years ago, life has been much more challenging but fulfilling. Being next to her after work has helped me to relief stress and energized me to get back to my working table every night.

Table of Contents

Abstract

Wave breaking, a common occurrence in the oceans, plays an important role in air-sea interactions including the transfer of energy and mass across the air-sea interface, turbulent mixing in the surface layer of the ocean, and ambient noise generated during breaking. It is a highly non-linear, intermittent three-dimensional phenomenon involving two-phase flows and turbulent mixing. Despite numerous studies in the past, there is still a need for a deeper understanding of the wave breaking process. Due to the complexity of the breaking process, studies of wave breaking (both experimental and numerical) are limited by the methodologies available and there remain significant gaps in fully understanding the mechanics of wave breaking. In this thesis, a detailed numerical study of wave breaking has been carried to examine the local physics of the wave plunging process, with an emphasis on the mechanics of the plunging jet, air entrapment, subsequent breakdown of the entrapped air, vertical sprays and turbulent mixing.

An enhanced Smoothed Particle Hydrodynamics (SPH) methodology has been developed for the numerical study. The key controlling parameters of the SPH model are carefully selected through calibration and sensitivity studies to minimize errors at the air-water interface. At the solid boundaries, an enhanced "ghost particle" method is developed to improve the consistency of the flow field near the boundaries. Within the fluid domains, flow regularization techniques including the velocity correction and the 1st order density re-initialization are applied. These methods are modified to account for large differences in the density and pressure gradient across the air-water interface and the conservation of momentum. The SPH code is also coded to run in a parallel computing cluster, hence increasing the computational speed and resolution. As the simulation is still compute-intense, even with parallel computation, a multi-scale nesting approach is also developed to reduce the overall computational cost.

The developed SPH code is validated through well-known benchmarks including water slosh-ing, dame break with impact on vertical wall and rising bubble in a water column. The code is also calibrated through sensitivity studies of sinusoidal wave propagation in long water flume and modulation and focusing of a wave packet. A horizontal moving wave paddle is modelled in the SPH code to simulate the actual wave generation processes.

Verification studies showed that the enhanced SPH model is able to simulate complex wave breaking adequately. An experimentally simulated plunging wave (Kway 2000), generated through wave-wave interactions, is simulated in this study and this forms the basis for the de-tailed studies of the wave plunging process. Both the air and water layers are modelled in the simulation, hence permitting a more accurate description of the air-water interaction. The study has been conducted with very high temporal and spatial resolutions. This is necessary in order to pick up the finer details that have been observed in the experiments but not cap-tured in the past numerical simulations.

The numerical results of the 2D plunging wave in deep water obtained in this study compare well with the experimental results of Kway (2000). These include details of the plunging jet, jet impingement, air entrapment, disturbances on the surface of the entrapped air tube, for-ward splash, vertical jet ahead of the plunging jet, upward water sprays, collapse of the en-trapped air tube and bubble generation in the water column. The numerical results have also helped to elucidate finer details of the wave breaking process. These include the bifurcation of the flow field relative to the crest velocity, especially on the wave front near the crest, cir-culations coupled to the air entrapment process, the air tube "rolling" forward, vertical jet col-lapsing in conjunction with air "squirting" out from the entrapped air pocket generating the characteristic vertical water spray, distributions of pressure, acceleration and vorticity in the vicinity of the plunging crest, and the dissipation of wave energy associated with the plung-ing.

List of notations

(Only frequently used notations are listed)

ρ	Density
p	Pressure
$\mathbf{x}$	Position
$\mathbf{u}$	Velocity
V	Velocity magnitude
$\mathbf{a}$	Acceleration
C	Wave speed
c_s	Sound speed
$\mathbf{g}, g$	Gravitational acceleration
W	Kernel function
h	Smoothing length
D	Water depth
H	Wave height
T	Wave period
$t_w = t(g/D)^{1/2}$	Dimensionless time
$p/\rho g D$	Dimensionless pressure
V/C	Dimensionless velocity magnitude
u/C	Dimensionless horizontal velocity
w/C	Dimensionless vertical velocity
Subscript $_{a,b}$	Particle a,b
Subscript $_{W,A}$	Water and Air

List of figures

List of tables

Chapter 1.   Introduction

1.1   Background and motivation of the study

The breaking of surface waves is a common occurrence in the oceans. Generally, surface wave breaking is defined as the irreversible transformation from irrotational to rotational motion, generating air bubbles, vorticity and turbulence in the water column. Wave breaking may occur at any water depth as a random, intermittent and highly unsteady process. Theoretically, a wave would remain stable only if the water particle velocity at the crest is less than the wave celerity or phase velocity (Stokes, 1880). If the wave height is to become so large that the water particle velocity at the crest exceeds the wave celerity, the wave would become unstable and break.

In the ocean, the wave length (or height) of breaking waves can range from millimeters for capillary-gravity waves to meters for gravity waves. Large breaking waves of tens of meter in height usually occur in shallow water under storm conditions. Large waves can also build up and break in relatively calm and deep waters due to energy concentration over in both space and time, enhanced by the nonlinearity (Brandini and Grilli, 2000). The concentration of wave energy could be the result of transformation processes such as wave-current interaction, modulation instability, effect of bottom topography (shoals, ridges, refraction), and directional focusing (superposition of different wave components with different frequencies, phases, directions).

Wave breaking plays an important role in the air-sea-structure interactions. It dissipates a large amount of the wave energy and limits the height of ocean wave. The energy lost in the breaking process at deep water is mainly transferred into surface current and turbulence in the water column. Energy is also transferred to the air through the air-sea interactions at the interface. The turbulence generated during wave breaking is responsible for the strong mixing in the surface layer of the ocean, down to the depth of an order of one wave height. Near the shore, the generated current and turbulence are among the main driving forces for the sediment erosion and transport.

Wave breaking generates air bubbles and entrains them into the water body. The dynamics of the entrained air significantly influences the turbulence intensity that in turn affects the energy dissipation and other turbulence related processes. Sprays of water droplets and the disengagement of tiny water particles which are subsequently transported away by wind, on the other hand, are crucial factors in far-field transport of pollutant. Air bubbles also contribute to the ambient noise generated during the breaking process.

Given its significant role in oceanic processes and air-sea interactions, there is clearly a need for a deep understanding of the wave breaking process. Wave breaking, however, is a highly non-linear, intermittent three-dimensional phenomenon which involves two-phase flows and strong turbulences and "white-caps". Due to the complexity of the breaking process, studies of wave breaking (both experimental and numerical) are still limited by inability to quantity specific near-field details of the breaking and mixing. Despite numerous studies already pursued in the past, there remain many gaps in the understanding the phenomenon.

In this thesis, we have chosen to conduct a numerical study of the wave plunging process, an extreme wave breaking process that includes jet formation, air entrainment, sprays and turbu-

lent mixing. A novel numerical method and advance computing technique are developed to reach quantify the complex process and to gain further insights on the breaking phenomenon.

1.2 Reviews of wave breaking study

The wave breaking phenomenon covers a wide range of scales and intensities, from small and gentle spilling waves to large and violent plunging waves. Commonly, breaking waves have been classified into four different types based on the physical changes of the surface profile during the breaking process. These four types are named spilling, plunging, collapsing, and surging. There is no distinct quantitative criterion to distinguish the breaker types. Instead, they are often progressing from one type to the next in the above order. Some descriptions of these breaker types are as follows:

- Spilling breaker: the white foam, consisting of turbulent air-water mixing, appears at the wave crest and spills down the front face of the propagating wave. The turbulence is uniformly dissipating wave energy, resulting in a continual decrease in the wave height.

- Plunging breaker: the front face of the wave steepens and overturns. A plunging jet ejects from the wave crest and splashes near the base of the wave. The energy dissipation is more confined than for a spilling breaker. The plunging jet impingement may regenerate smaller more irregular waves that propagate forward.

- Collapsing breaker: the front face of the wave steepens at incipient breaking, the lower portion of the face plunges forward and the wave collapses. The collapsing breaker is an intermediate form between the plunging and surging.

- Surging breaker: the crest of the steepening wave remains unbroken and advances up the beach slope and retreats.

Waves break in the ocean usually in the form of spilling and plunging breakers in both deep and shallow water, but most common in shallow water. Collapsing and surging breakers however only occur in shallow water. In deep water, spilling breakers are most common and the "white-capping" occurs if accompanied with strong wind. Extreme plunging waves with heights of tens of meters were observed in deep water and reported as "freak" or "rogue" waves.

Many studies of wave breaking have been focusing on the plunging breakers since they are the most powerful, generate more violent fragmentation of water, generate more turbulence, trap a larger amount of air and create much greater air entrainment than other types. In shallow water, turbulence and strong current generated by plunging breakers are the main driving forces behind the beach erosion.

Typical plunging breakers in the nature are shown in Figure 1.1. Plunging breakers are classically characterized by a visible curling over of a steepened wave crest with an inner core and falling jet impacting on the front water surface. The general process involved in the wave steepening and subsequence breaking of plunging wave has been described in details by numerous authors through field observations, laboratory experiments (Galvin, 1968; Longuet-Higgins, 1982; Peregrine, 1983; Rapp, 1986; Bonmarin, 1989; Chanson and Lee, 1997; Li, 2000; Kway, 2000; Chanson et al., 2002; Li and Raichlen, 2003) and numerical simulations (Longuet-Higgins and Cokelet, 1976; Cokelet, 1979; Peregrine et al., 1980; Grilli et al., 1997; Chen et al., 1999; Lubin et al., 2003; Colagrossi and Landrini, 2003; Gotoh et al., 2005).

Figure 1.1. Breaking of plunging waves in the nature. Left: side view; Right: front view.

1.2.1 Experimental studies of plunging breaking waves

Among the first to study the evolution shape of the breaking wave, Galvin (1968) presented the classification of breaker types based on their appearance. The overturning motion of the plunging breakers was later reported in the theoretical studies of Longuet-Higgins (1982), New (1983), where analytical solutions to characterize the shape of front face of the overturning wave were suggested. A more realistic mathematical solution to describe the front, loop, jet and rear face of the wave was suggested by Greenhow (1983). These formulations are limited to the stage of jet formation and development.

More recently, innovative high-speed photography and videography technologies were used to capture entire evolution of a plunging breaker from different view angles. These photographs and videos allowed detail two- and three-dimensional analyses of the plunging breakers to be performed. At certain angles, the "white-cap" effect of air-bubbles is greatly reduced which allows us to observe clearly the internal structures of the wave breaking and gives better description of the complex flow field.

Typical photos of plunging breakers in shallow water and deep water are shown in Figure 1.2 and Figure 1.3. In both cases, the breaking begins with the curling of the steepened crest. Due

to a quicker propagation of the upper part of the wave and the gravity, the crest overturns creating a sharp plunging jet that impinges upon the front water surface. New et al. (1985) examined the velocities and accelerations of particles in the free surface of periodic overturning waves on finite (shallow) depth and observed maximum horizontal velocities almost twice the linear phase speed and maximum accelerations up to six times that of gravity. Upon impingement, the jet reconnection with the front face of the wave gives rise to two important processes which were clearly observed from experiments: the generation of a splash-up cycle and the air entrainment process from formation through collapse of an air tube.
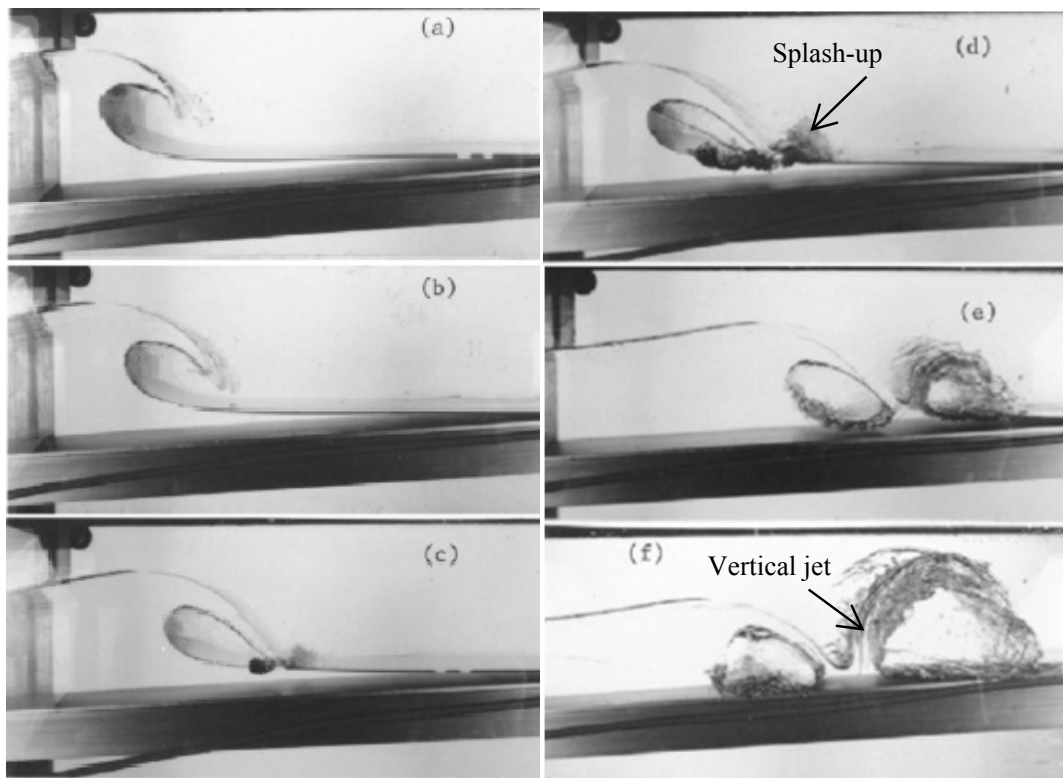
Figure 1.2. Side view of a breaking sequence of a solitary wave on a plane slope. Wave height is much larger than water depth at the breaking point. Very strong vertical jet is generated. Photographs from Li (2000).
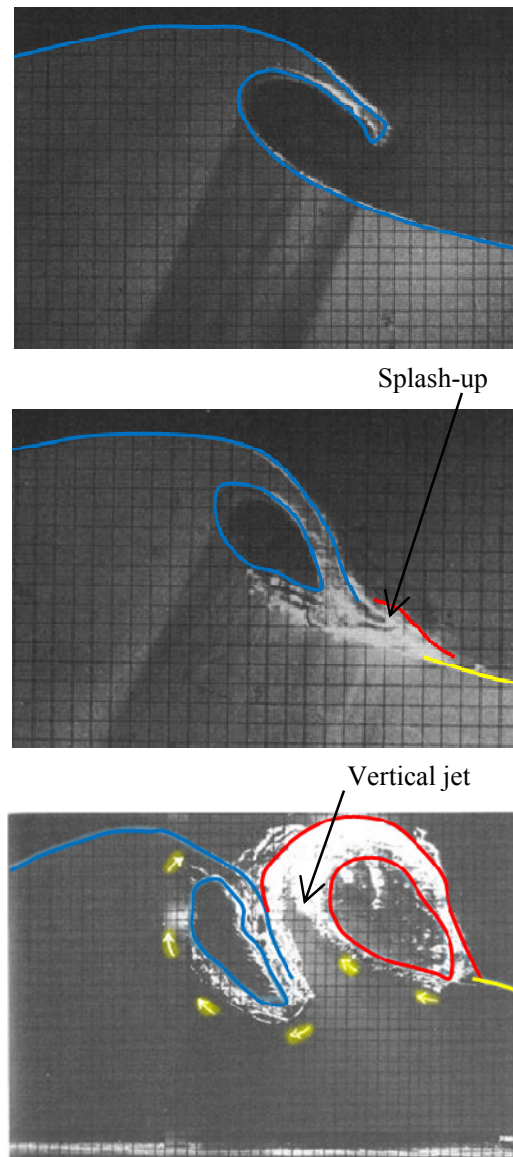
Figure 1.3. Breaking of a solitary wave over a flat bed showing curling over and impact on front water of plunging tip and the circulation of the plunging jet (blue), and the splash-up and vertical jet (red). Photographs from Miller (1976).

In the splashing process, where the plunging jet penetrates the front water surface, a large amount of the water in the front is pushed up by the plunging jet to form a jet of water, called splash-up in Miller (1976). This splash-up, which looks like a vertical jet, can rise higher than the preceding wave. The front part of the vertical jet creates a second plunging jet which, in turn, impinges on the front water surface and creates another splash-up down-stream. These

sequences of the splash-up were first described in Miller (1976). Unlike the first sharp plunging jet, these subsequent splash-up consist of fragmented water and entrained air.

The mechanics of the splash-up formation including the penetration of the plunging jet into the wave front and the composition of the emerging water mass ahead of the wave front are still poorly understood. Reviews of shallow plunging breaker in Peregrine (1983) proposed three schemes of splash-up occurrences (see Figure 1.4). In scheme (a) the plunging jet is totally reflected from the free surface and generates the splash-up. Scheme (b) suggests that the plunging jet totally penetrates into the water and the splash-up consists of water from the base in the front being pushed by the plunging jet. The last scheme is an intermediate between (a) and (b) where water from both the plunging jet and the base compose the splash-up. In all schemes, the plunging jet does not penetrate deeply into the water. There could be a similarity in deep-water plunging breaker. Discussions in Bonmarin (1989) based on snapshots of deep water breaking waves suggested that all three schemes could occur. The location of plunging jet impact with the front surface is always above the still water level and the angle of the plunging jet with the front surface is about 31 degrees (Chanson and Lee, 1997).
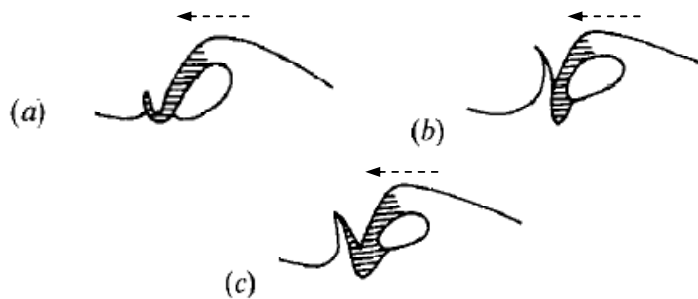
Figure 1.4. Possible modes of splash-up generation by Peregrine (1983). Water in and from the plunging jet is shaded.

In the air entrainment process, when the plunging jet is penetrating the front water surface, it closes over the air beneath it to form a tube of air with circulation motion due to the friction

at the contact surface with the surrounding water (see Figure 1.5, where the camera was positioned behind the wave and below the water surface). The formation of the air tube and the circulation motion were also described in Peregrine (1983). During the early stages, the surface of the air tube is relative smooth except some disturbances near the contact region (Figure 1.5a). As the wave continues to propagate forward, the air tube rolls forward and the entrapped air is carried along with the tube. Instabilities set in and the surface of the tube becomes wavy (Figure 1.5e, f). The phenomena were described in Kway (2000). It is not clear where the instability came from but the series of photographs in Figure 1.5 suggests that the disturbance near the contact area rolls up and eventually spread over the tube. Eventually, the tube loses its momentum and breaks abruptly. It was discussed in Peregrine (1983) that the air pressure and the centrifugal acceleration usually balance the inward pressure gradient and prevents the rapid collapse of the tube. The noncircular initial state and three-dimensional instabilities both contribute to this tube having a relatively short life. Sometimes the trapped air vents through the surface with a sudden spout of spray. It was also mentioned in Miller (1976) and clearly observed from photographs in Figure 1.6 that some water jets spout out from the top of the breaking wave, creating upward sprays near the crest (Figure 1.6). It is clear that the sprays and collapse of the air tube occur simultaneously. The remaining trapped air being broken down into smaller bubbles which eventually resurface due to the buoyancy. Once at the water surface the bubbles break up, releasing air and creating foamy water surface (observed in Mutsuda and Yasuda, 2000).

How the upward sprays are generated during the plunging wave breaking is still not fully understood. It may be associated with the jets of air squirting out from the entrapped air tube. If this is the case, the air tube must be highly compressed during the collapsing of the air tube before being squirted out.
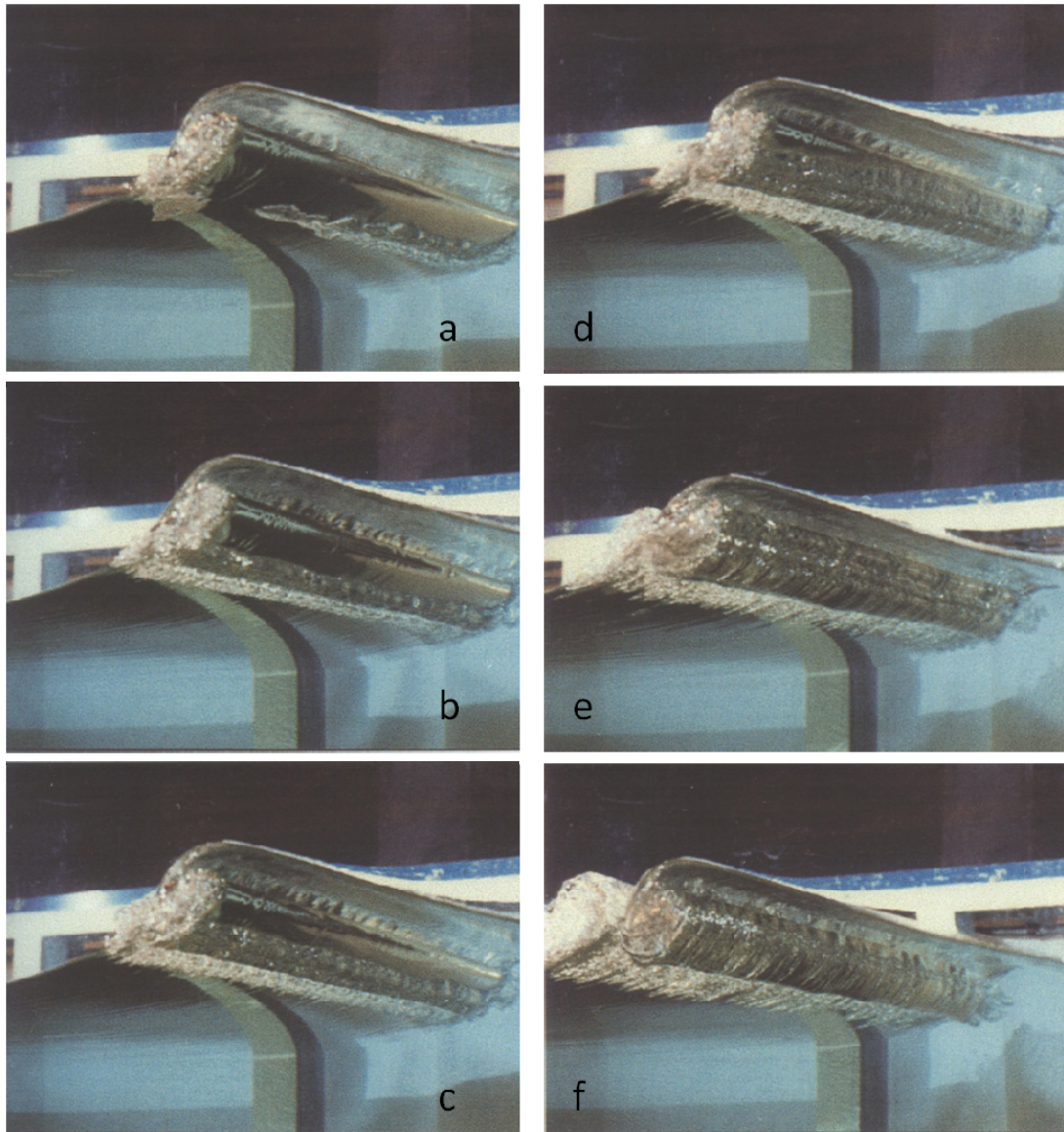
Figure 1.5. The formation of an elliptical air tube when the plunging jet closes up with the front water (Kway, 2000). Photos taken from low, behind view.
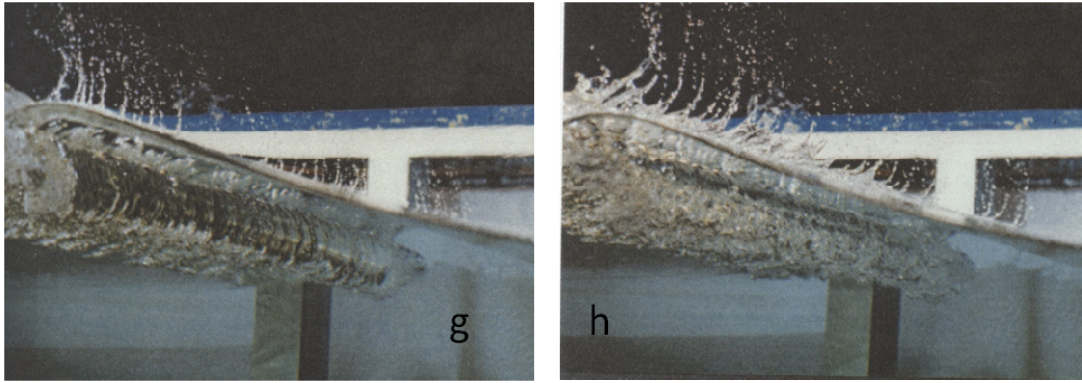
Figure 1.6. The collapsing of the air tube and upward sprays near the crest (Kway, 2000)

Bonmarin (1989) described an additional entrainment process. In this process, air is en-trapped during the interaction between the plunging jet and the rear of the vertical jet, which looks like two water masses turning in opposite directions. This interaction between the breaking crest and the vertical jet can display two modes: either the rear part of the vertical jet flows over the falling crest, or the rear part of the vertical jet looks like a falling water jet moving backwards and 'penetrating' the front of the original breaking crest as it moves forward. This air entrainment process appears at each successive splash-up/vertical jet cycle and the amount of air entrained decreasing logically from one vertical jet to the next one. This process is difficult to resolve due to the presence of a large foamy region generated.

A study by Battjes (1988) indicated that the impingements of the plunging and vertical jets on the front water surface and the collapse of the trapped air pocket result in a region with vertical motion and high concentration of a large amount air bubbles rising gradually to the surface. Due to the difficulties in measuring flow conditions in the aerated and fully turbulent part of breaking waves, measurements of flow field such as velocity, acceleration, pressure are not reliable. Thus studies of the flow field during and post-breaking through laboratory experiment is limited.

1.2.2 Numerical studies of plunging breaking waves

Over the past few decades, numerical studies have proven to be an excellent alternative to laboratory experiments for the study of breaking waves. Advance numerical models are now able to reproduce many complex features associated with the wave breaking process. The earliest numerical models used in the study of wave breaking were based on potential flow. Longuet-Higgins and Cokelet (1976) developed the mixed Eulerian-Lagrangian method combined with a boundary integral equation which was later used by Cokelet (1979) and Peregrine et al. (1980) to study the details of internal flow before breaking. Grilli et al. (1997) developed a high order Boundary Element Method (BEM) to solve the problem of nonlinear wave evolution with high accuracy. The high order BEM was subsequently extended to three-dimension (Grilli et al., 2001) and applied in the simulation of shoaling and overturning of a solitary wave. Due to the limitation in resolving fragmentation and coalescence of its computational mesh, all BEM simulations have to stop at the stage when the impinging jet touches the front water surface. Even though limited by the potential theory's assumptions and numerical implementation, BEM is still very useful in capturing and verifying key features prior to the instant of jet impingement. Chan and Melville (1988) and Dommermuth et al., (1988) used Boundary Integral Method to simulate deep-water plunging breakers and the results compared very well with experiments. The results also showed that the maximum velocity amplitude occurs in the cusp of the wave and is roughly twice as large as the linear phase speed based on a central frequency of the wave spectrum. The maximum Lagrangian acceleration is of the order of 6 g, occurring inside the loop and directs radially inward. The acceleration in the plunging jet is approximately 1 g and directs downward, suggesting that the tip of this overhanging wave is essentially in free fall.

Recently, grid based Navier-Stokes solvers coupled with a mathematical treatment for free surface have become very popular. These free surface techniques which are much more ver-

satile in modeling complex flows include Marker-And Cell, Volume of Fluid, and Level Set. The Marker-And-Cell was firstly used in Harlow and Welch (1965) to track the position of free surface using a large number of weightless markers. Subsequently, Sakai et al. (1986) extended the methodology to simulate plunging breakers on a sloping beach. The method was further improved in the Simplified Marker-And-Cell by Takikawa et al. (1997) and the Surface Marker by Christensen (1996) and Christensen and Deigaard (2001).

The Volume of Fluid (VOF) developed by Hirt and Nichols (1981) is currently the most common method used for modelling wave breaking. In VOF, the air-water interface is typically treated using interface reconstruction techniques. These include the Donor-Acceptor, also referred to as the Simple Linear Interface Reconstruction technique (Lemos, 1992; Lin and Liu, 1998; and Zhao et al., 2004), the Piecewise Linear Interface Construction technique (Chen et al., 1999) and the Defined Donating Region technique (Hieu et al., 2004). More recent implemented methods used an additional function to track the interface such as the Level Set (LS) method (Iafrati et al., 2001) or the Lax-Wendroff Total Variation Diminishing scheme (Lubin et al., 2003).

Depending on the Navier-Stokes solvers, turbulence associated with wave breaking has been modelled differently. The most direct approach is the Direct Numerical Simulation (DNS) where the turbulent mixing is directly modelled. The limitation, however, is that length-scales of the flow smaller than the grid scale will not be captured (see Chen et al., 1999; Iafrati et al., 2001; Abadie, 2001; Guignard et al., 2001; Watanabe and Saeki, 2002; Iafrati and Campana, 2003; Song and Sirviente, 2004). Another approach is the Reynolds Averaged Navier-Stokes (RANS) (see Lemos, 1992; Takikawa et al., 1997; Lin and Liu, 1998; Bradford, 2000) where the turbulence is captured through a closure model. Yet another approach is the Large Eddy Simulation (LES) where the flow characteristics that have length scale of the order of a

grid size is modelled directly in the governing equations (Zhao and Tanimoto, 1998). Features that are smaller than a grid size are approximated using a turbulence closure model.

In most of the above studies, the air entrainment was not taken into account and the simulations were carried out in two-dimension in which turbulence was not fully modelled. Recently, a few simulations were performed in three-dimension (Watanabe and Saeki, 1999; Christensen and Deigaard, 2001; Lubin et al., 2003; Biausser et al., 2004) and some have also included the dynamics of entrapped air (Mutsuda and Yasuda, 2000; Lubin, 2004; Lubin et al., 2006). Study by Lubin (2004) has described the overturning motion of the plunging jet, the air pocket and the splash-up process. The plunging jet is formed in the upper half of the fornt face of the steepened wave the tip of the jet has a shape of a rounded finger tip. An air vortex above the crest is generated and follows the wave during its motion. The falling crest includes a mixture of air and water and the tip of the jet mainly comprises of water droplets. When it hits the front water surface, the plunging jet does not penetrate very deep. The plunging jet closes over the air to form an air tube. The pressure in the air pocket increases while the entrapped air tries to escape. The splash-up is seen created partly from the rebounding plunging crest and partly from the front surface of the wave. These results also agreed with the conclusion of Chen et al. (1999) and the observation in Peregrine (1983). Impingement of the splash-up on the water surface generates another splash-up downstream that has smaller size. The entrainment and formation of air bubbles were captured in the model including the presence of large air bubbles that rise to and the free surface, generating sprays in the process. Lubin (2004) noted, however, that some large discrepancies could appear between two- and three-dimensional results and illustrated the importance of taking a turbulence model into account. These studies suggested that three-dimensionality of the flows is very important not only for correct simulation of the interface but also to depict 3D structure of turbulence. The dynamics of entrapped air has a significant role.

Although two-phase and three-dimension flows have been successfully simulated, studies with both features included are still a very big challenge due to the limitation in computation power. Moreover, the above grid-based methods suffer from unavoidable numerical smearing: the so-called numerical diffusion. The diffusion becomes even more severe when the steepness of the free surface is very large, which is a common feature in wave breaking. Spatial resolution is also a limiting factor of these grid based methods. A highly refined local mesh is typically required in order to capture small portions of fragmented water. Because of the existence of strong numerical diffusion and limitation in resolving fine features, grid-based methods fail to accurately reproduce the splash-up, the mixed air-water droplet sprays or the formation of tiny air bubbles. As the result, the subsequent processes such as turbulence generation and energy dissipation may not be accurately simulated.

The limitations of strong numerical diffusion and resolution could be resolved with mess-free particle methods such as the Smoothed Particle Hydrodynamics (SPH). Classical incompressible flows have been simulated withparticle methods using a Poisson equation for pressure and these are referred to as the Incompressible SPH (ISPH) or Moving Particle Semi-implicit (MPS) method. Koshizuka et al. (1998) has used MPS to simulate a breaking wave. Gotoh et al. (2005a) applied MPS to simulate wave overtopping process on vertical seawall. Khayyer and Gotoh (2007) and Khayyer et al. (2008) used the incompressible SPH to simulate a plunging jet without the effect of entrapped air. The ISPH method agreed well with the BEM and VOF (at an equivalent resolution) and the experiments during the early stage of the breaking process. At the later stage when the vertical jet is forming, the grid-based methods deviated significantly from the experiment while the ISPH reproduced the vertical jet shape very well. The use of Poison equation in two-phase flow however is not straightforward. The concept of slightly compressible flow with an appropriate equation of state in SPH has also been used to simulate classical incompressible flows. The method is commonly called SPH

(Monaghan, 1994; Morris et al., 1997). Colagrossi and Landrini (2003), Ikari et al. (2005) applied SPH to simulate a wave plunger in two-dimensional dam break problem taking into account the air dynamics. The SPH calculation of the evolution shape of the plunger showed good agreement with the BEM up to a limit (when the plunging jet is about to touch the water surface in the front), and thereafter the SPH method gave good agreement with the results of LS method and experiment. It was pointed out that, at an equivalent resolution the LS results were much smoother than those from SPH, and LS failed to capture some details smaller than a grid size such as water droplets and air bubbles. In these ISPH and SPH simulations, turbulence was modelled using LES.

Three-dimensional simulations of plunging breakers have been successfully achieved by Gotoh et al. (2005b) using MPS. In total, 180,000 particles of 0.002 m diameter were used in a 0.8 m long and 0.04 m deep flume. Periodic boundary condition was applied in the transverse direction. Results obtained showed that the plunging jet was not uniform in the transverse direction although the initial waves were uniform in this direction. Only fluid velocity across a water column was compared with the experiment. The velocity distribution agreed with the experiment but the magnitude of the velocity components deviated significantly from the experiment. In the simulation the dynamics of air and turbulence was not included in the governing equations and the resolution was rather coarse.

Based on the above studies using SPH, it is evident that SPH has significant advantages over grid-based methods especially if the surface displacements are complex. In problems involving very small perturbations, however, SPH is less accurate and that makes grid-based methods preferable. In the SPH method, the governing equations can be discretized using a Lagrangian method. As a result, the advection is treated more exactly by tracking the motion of the particles and hence the numerical diffusion can be reduced. Furthermore, due to the fact that the particles represent the fluid particles, with problems involving more than one material

such as air, water and sediment, each medium is described by its own set of particles and properties. Hence the multiphase interface tracking problems, which are difficult for classical gridded methods, become straightforward for particle methods. The third advantage is that particle methods treat the continuum, fragmentation and coalescence of the materials in a natural way through the interaction among particles. Therefore particle methods are very useful for solving problems involving fragmentation and coalescence of the bodies such as violent breaking wave surface. Representing the real materials by particles also leads to a computational advantage since the particles are only required at the areas where presences the material. The resolution can be made to depend on position and time. This saves the storage and calculation efforts. Since the discretization of the high order derivatives in SPH method is much simpler than that in gridded Eulerian methods and because of the close similarity between particle methods and molecular dynamics, it is possible to include more complex physical processes easier and the extension to three-dimension is more straightforward.

There are limitations in using SPH. Past studies indicated that the accuracy of SPH may reduce when the particle locations are unstructured. The problem becomes more severe when the so-called "tensile instability" or particle clumping occurs (Monaghan, 1992). There are gaps in the use of SPH and further development would be necessary.

1.3   Scope and objective of the present study

The scope of the wave breaking study covers the generation of the air tube, splash-up, vertical jet, collapsing of the air tube and sprays of water droplets. Based on reviews of the past studies, it is evident that most of the above listed features have already been observed and described. However, it is also clear that some specific details of these features are still inadequately quantified and not clearly explained nor fully understood. These include:

- the formation of the splash-up (three possibilities have been suggested by Peregrine (1983));

- the forces that keep the entrapped air tube intact;

- the sources of instability on the surface of the entrapped air tube and the subsequent transformation of these surface roughness;

- the process of air tube collapse and collision with the splash-up;

- the mechanism leading to the water sprays observed in Figure 1.6; and

- the dissipation of wave energy.

While controlled laboratory experiments and advanced instrumentation have helped to elucidate the physics of wave plunging, the quantification of finer details in the near-field of the entrapped air tube and mixing are limited by the complex air-water mixture. Most grid-based numerical methods, on the other hand, are too dispersive to capture the features that are at the scales of the grid resolution. The Smoothed Particle Hydrodynamics method, however, appears to be promising and has the potential to be refined to adequately capture the detail physics of wave plunging.

The overall objective of this thesis is to develop an enhanced Smoothed Particle Hydrodynamics methodology and to numerically reproduce all the finer features of wave plunging including the collapse of the entrapped air tube and the upward water sprays. The latter has not been numerically simulated in the past. More specifically, the objectives are to:

- Develop an enhanced SPH program to simulate the wave plunging.

  The SPH program will be developed from the basic SPH serial code SPHysics v1.0 (http://wiki.manchester.ac.uk/sphysics) which has been used for general free surface flows. Selective developments from other researchers will be modified and incorporated in to the code. These include the two-phase flow formulation, sharpness control

for interface from Collagrossi and Landrini (2003), high order kernel functions from Liu and Liu (2003), velocity regularization (XSPH) modified for two-phase flow to prevent particle penetration from Monaghan (1992), the density regularization modified for two-phase flow to reduce pressure oscillation from Belytschko et al. (1998), turbulence model using the concept of LES from Gotoh et al. (2004). Additional developments are also needed to further enhance the accuracy, stability and simulation capacity of the SPH code. These include an enhanced "ghost particle" method to improve the consistency of the flow field near solid boundaries, the code parallelization and the multi-scale nesting approach that allow very large problem to be simulated.

- Calibrate and validate the SPH program against benchmarking problems (analytical solutions and measurements). The key controlling parameters of the SPH model are carefully selected through the calibration of the SPH program.

- Development and verification of a numerical wave tank using the SPH program.

- Simulation of a 2D plunging wave breaking using the SPH program.

- Detailed studies of the near-field physics of wave plunging.

1.4   Structure of the thesis

Chapter 2 presents the details of the SPH methodology used in this thesis and the enhancement developed to refine the methodology. These include the formulation of the SPH methodology, the numerical treatment, implementation of the model, code parallelization and nesting, and the development of numerical wave tank.

Chapter 3 presents the calibration and validation of the developed code through most important test cases, the verification of a numerical wave tank.

Chapter 4 focuses on the detailed simulation of the wave plunging process and a detailed analysis of the physics of wave plunging, including the plunging jet formation, jet impinge-

ment, air entrapment, disturbances on the surface of the entrapped air tube, forward splash, vertical jet ahead of the plunging jet, upward water sprays, collapse of the entrapped air tube and bubble generation in the water column.

Key observations are concluded in Chapter 5.

Chapter 2.   Methodology

2.1   The wave breaking problem for the study

2.1.1   Plunging breaking waves over a flat bottom

A schematic presentation of a plunging breaking wave over a flat bottom is proposed as in Figure 2.1. Choosing a suitable well-defined set of initial condition and boundary conditions is crucial for the successfulness of generating correct plunging breakers.
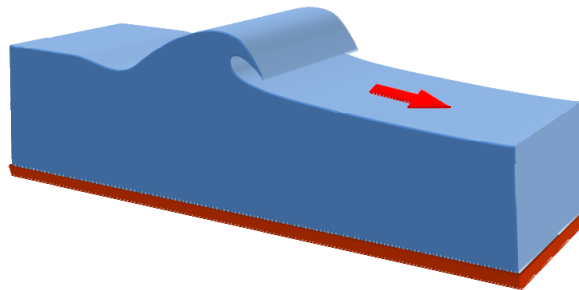
Figure 2.1. Schematic presentation of a plunger in a long, flat bottom water flume.

Cokelet (1979), Chen et al. (1999), Lubin et al. (2006) used a periodic sinusoidal wave of large amplitude as the initial condition. The periodic boundary condition is applied at the two ends in the wave propagation direction. Properties of the fluid are calculated based on the linear or nonlinear wave theories. The instability of the travelling nonlinear waves will lead to a plunging breaker. This initial condition has certain computational advantages: it is easy to setup; the initial wave profile can be calculated exactly; and the numerical dissipation due to

pre-breaking evolution of the wave is minimized. However, the condition is too ideal hence the breaking process may not reflect the correct phenomena and physics.

Colagrossi (2004), Khayyer (2008) used a piston paddle to generate a solitary wave. The wave was made unstable by let it run up on a slope beach or propagate over an obstacle. The breaking wave over a flat bed also can be created. Colagrossi (2004) generated a large solitary wave by imposing a large and rapid movement of the paddle. This method also has similar computational advantages: it is easily setup; the pre-breaking condition is easily controlled using wave paddle theory; and the numerical dissipation due to pre-breaking evolution of the wave is minimized. However, this condition is not suitable for our study since solitary wave is a shallow water wave and the breaking process is strongly affected by the bottom.

Our study aims to numerically reproduce an experimental wave breaking in Kway (2000) where a strong plunger in deep water was created by the modulation and focusing of a wave packet. A sketch of the numerical wave flume is given in Figure 2.2. The numerical experiment takes the same dimensions as the laboratory experiment done in Kway (2000).
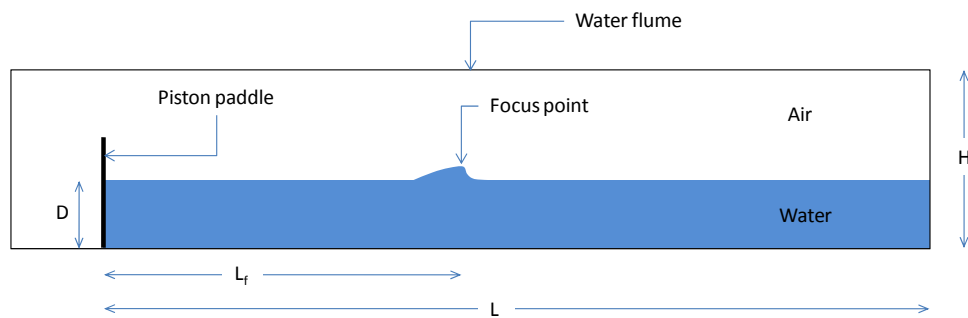
Figure 2.2. Dimension of the water flume and setup of the numerical experiment.

The wave flume has a length of 36 m and a height of 2.4 m of the actual laboratory experiment. The water depth is 0.8 m. A wave paddle at one side of a water flume is programmed to generate a packet of short waves with small wave heights and wave frequencies in a narrow

band which has high to low frequency order. The amplitude and frequency of the centre component are 0.0111 m and 0.83 Hz, respectively. The ratio of water depth over wave length of the centre component is 0.8/2.219 = 0.36, thus it is an intermediate water wave (close to 0.5 which is the criterion for deep water wave). The wave celerity and wave group speed calculated by linear theory are 1.84 m/s and 1.01 m/s, respectively. Other parameters of the experiments are given in Table 3.1 in Kway (2000). The details of the generation of a breaking wave will be discussed later in this Chapter.

2.1.2   Mathematical description of a water wave problem

The problem of 2D wave propagation and breaking is governed by the Navier-Stokes equations which are derived from the Newton's conservation law of mass and momentum. The equations read the form of

$$\frac{d\rho}{dt} = -\rho \nabla \cdot \mathbf{u} \tag{2.1}$$

$$\frac{d\mathbf{u}}{dt} = -\frac{1}{\rho} \nabla p + \nu \nabla^2 \mathbf{u} + \mathbf{g} + \nabla \cdot \boldsymbol{\tau} \tag{2.2}$$

where ρ is the density of the fluids, $\mathbf{u} = (u_x, u_z)$ is the velocity and p is the pressure of the fluids. The gravitational acceleration is $\mathbf{g} = (g_x, g_z)$, ν is kinetic viscosity, $\boldsymbol{\tau}$ is turbulence shear stress. The effect of surface tension could be neglected (Peregrine, 1983). In this study of plunging wave breaking, the fluids are water and air.

2.2   Numerical approximation to governing equations: the Smoothed Particle Hydrodynamics method

The Smoothed Particle Hydrodynamics (SPH) method was first introduced by Gingold and Monaghan (1977) and Lucy (1977) independently. In their works, a kernel estimation technique was used to derive the equations of motion for simulating astrophysical phenomena in

three-dimensional and open space. The kernel estimation technique had been used earlier by statisticians to estimate probability densities from sample values (Rosenblatt, 1956; Parzen, 1962; Boneva et al., 1971). This method allows one to estimate a function at any point using the values of the function itself at the other points weighted by the values of kernel function at these points. It is essentially an interpolation technique. The estimate of the function could be differentiated exactly provided the kernel was differentiable. Because of its close relation to the statistical concept, Gingold and Monaghan (1977) and Lucy (1977) firstly described the method as a Monte Carlo method.

The SPH method was applied extensively a decade later in the area of astronomy, including the simulation of the binary neutron stars and stellar collision (Benz, 1990; Monaghan, 1992; Rosswog and Davies, 2002) or the simulation of the formation of the Moon (Benz et al., 1986), and tar formation studies (Bate et al., 1995, 2003). Monaghan and Lattanzio (1991) used SPH to simulate the collapse and formation of galaxies. Michel et al. (2004) applied SPH to the breakup of planetestimals and the formation of asteroid families.

The SPH method has also been applied to a wide range of areas of computational solid mechanics or fluid dynamics because of its advantages of simplicity, flexibility in programming and ability of incorporating complex physical phenomena. These works include the simulations of elasticity (Libersky and Petschek, 1991), large deformation and fracture problems (Benz and Asphaug, 1994, 1995). Elastic SPH also provides a simple and robust technique for simulating complex fracture in geological rock formations and in brittle materials (Gray et al. 2001, Gray and Monaghan 2004). Benz and Asphaug (1994, 1995) showed that SPH could yield much better results than the finite element or the finite difference methods. Other remarkable applications of SPH include simulations of impulsive loading, hyper velocity impact (HVI) and explosion problems involving shock wave propagation within solid bodies (Randles and Libersky, 1996; Johnson et al., 1996). SPH was also used in blood simulation

for virtual reality surgery (Muller et al., 2004), and has been incorporated in commercial software package such as Autodyn for solving problems of high velocities, large deformation and fragmentation.

Applications of SPH in fluid dynamics have been increasing in recent years. The first applications of SPH in fluid dynamics were in gas dynamics, but later extended to problems involving incompressible flows by treating the flows as slightly compressible and with an appropriate equation of state (Monaghan, 1994; Morris et al., 1997). Applications of SPH in computational fluid dynamics include the simulation of underwater explosion, shock wave (Liu et al., 2003), elastic flow (Fang et al., 2006), flow through porous media (Zhu and Fox, 2002), liquid metal moulding (Cleary and Ha, 2002), heat transfer and mass flow (Cleary, 1998), ice and cohesive grains (Gutfraind and Savage, 1998; Oger and Savage, 1999) and multi-phase flows (Monaghan and Kocharyan, 1995; Gotoh et al., 2001; Gotoh et al., 2002). SPH has also been used for simulations of water wave breaking problems (Koshizuka et al., 1998; Gotoh et al., 2005a; Monaghan and Kos, 1999; Colagrossi and Landrini, 2003; Ikari et al., 2005).

2.2.1   Kernel approximation

The heart of the SPH method is an interpolation which allows a function to be expressed in term of the contribution of its values at any point $\mathbf{x}=(x,z)$ in the 2D space. This expression has the form of

$$A(\mathbf{x}) = \int_{\Omega} A(\mathbf{x}')W(\mathbf{x}-\mathbf{x}',h)d\mathbf{x}' \tag{2.3}$$

where $W(\mathbf{x}-\mathbf{x}',h)$ is an interpolating kernel (or kernel function) and the integration is taken over the entire domain Ω, and h is the smoothing length of the kernel function. The kernel function must satisfy the following two important properties

$$\int_{\Omega} W(\mathbf{x} - \mathbf{x}', h) d\mathbf{x}' = 1 \tag{2.4}$$

$$\lim_{h \to 0} W(\mathbf{x} - \mathbf{x}', h) = \delta(\mathbf{x} - \mathbf{x}') \tag{2.5}$$

For discrete problems, the interpolation is approximated by a summation over all discrete points $\mathbf{x}_b$ (represented as particle b which has mass m_b, density ρ_b and velocity $\mathbf{u}_b$).

$$A(\mathbf{x}) = \sum_b \frac{m_b}{\rho_b} A(\mathbf{x}_b) W(\mathbf{x} - \mathbf{x}_b, h) = \sum_b \frac{m_b}{\rho_b} A_b W_{ab} \tag{2.6}$$

where A_b is the value of function $A(\mathbf{x})$ at location $\mathbf{x}_b$ and $W_{ab} = W(\mathbf{x}_b - \mathbf{x}_a, h)$.

Using a differentiable kernel function and the approximation (2.6), one can compute the derivatives of a function $A(\mathbf{x})$ by translating the differentiation to the kernel function. By doing so, the gradient and divergence of a function $A(\mathbf{x})$ can be approximated as

$$\nabla A(\mathbf{x}) = \sum_b \frac{m_b}{\rho_b} A(\mathbf{x}_b) \nabla W(\mathbf{x} - \mathbf{x}_b, h) = \sum_b \frac{m_b}{\rho_b} A_b \nabla_a W_{ab} \tag{2.7}$$

$$\nabla \cdot A(\mathbf{x}) = \sum_b \frac{m_b}{\rho_b} A(\mathbf{x}_b) \cdot \nabla W(\mathbf{x} - \mathbf{x}_b, h) = \sum_b \frac{m_b}{\rho_b} A_b \cdot \nabla_a W_{ab} \tag{2.8}$$

Although the above summations are taken over all particles, only a few of them have significant contribution since the kernel function W is often chosen so that its value drops rapidly to zero for $|\mathbf{x} - \mathbf{x}_b| > h$ (see the next section).

2.2.1.1   Kernel function

The choice of kernel function (also called smoothing function) is crucial to the performance of SPH. The kernel function not only represents the pattern for the function approximation, dimension of the domain, but also determines the consistency and the accuracy of the particle approximations.

Different kernel functions have been used in the SPH method as shown in the published literatures (Monaghan, 1992; Liu and Liu, 2003). In general, any function that satisfies the requirements in Equation (2.4) and (2.5) can be used as kernel function. Equation (2.4) is normalization, which is to ensure that constants are approximated exactly. Equation (2.5) indicates that if h tends to zeros, the kernel function will tend to a delta function. If the kernel function is a delta function, Equation (2.3) will reproduce A exactly. Other requirements or properties for the kernel functions may be needed to keep the kernel function insensitive to particle disorder, and the errors in approximating the integral interpolants are small provided the particle disorder is not too extreme (Monaghan, 1992). This will lead to better accuracy and efficiency of the kernel approximation. Some of the typical requirements or properties are as follows

- The smoothing function have a compact support (or compact support domain), i.e. $W(\mathbf{x} - \mathbf{x}_b, h) = 0$ for $\mathbf{x} - \mathbf{x}_b > kh$, where k is a parameter which determines the spread of the kernel function. This property transforms a kernel approximation from involving entire set of particles in the computation domain to a local domain which involve a few neighbour particles. As a result, computational effort is significantly reduced

- The kernel function is non-negative in the support domain. It is not strictly required, but it is important to ensure a meaningful representation of some physical phenomena.

- The kernel function is monotonically decreasing with increase in distance away from the particle. This property means that nearer particles should have bigger physical influences on (or interactions with) the concerned particle. With the increase in distance between two interacting particles, the interaction force decreases.

- The smoothing function is symmetric. This property means that particles from the same distance should have equal effect on a concerned particle. This is not a very strict condition, and it is sometimes violated so that better results can be achieved.

- The smoothing function is sufficiently smooth.
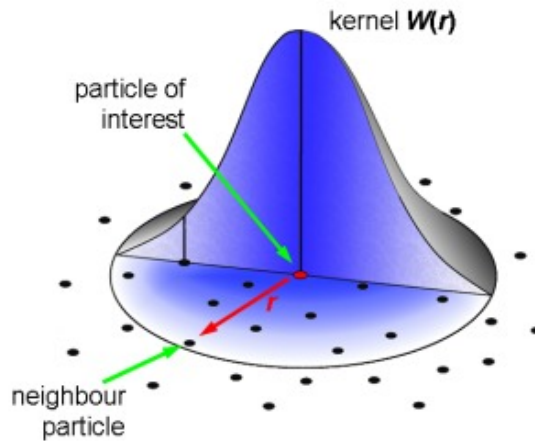
Figure 2.3. Kernel function and its compact support domain

There are several ways to define a kernel function. One of them is the method based on piece-wise continuous spline functions (M_n) that have $(n-2)$ continuous derivatives Schoenberg (1946). These functions are defined by the Fourier transform (see Monaghan, 2005).

$$M_n(x,h) = \frac{1}{2\pi} \int_{-\infty}^{\infty} \left[\frac{\sin(kh/2)}{kh/2} \right]^n \cos(kx)\,dk \qquad (2.9)$$

Another way to define the kernel function is to make use of the Taylor expansion to the original integral representation of the kernel approximation in Equation (2.3) (Liu and Liu,

2003). Assuming that the function $A(\mathbf{x})$ is sufficiently smooth, applying the Taylor series expansion to the function $A(\mathbf{x}')$ in the vicinity of $\mathbf{x}$ yields

$$
\begin{aligned}
A(\mathbf{x}') &= A(\mathbf{x}) + A'(\mathbf{x})(\mathbf{x} - \mathbf{x}') + \tfrac{1}{2} A''(\mathbf{x})(\mathbf{x} - \mathbf{x}')^2 + ... \\
&= \sum_{k=0}^{n} \frac{(-1)^k h^k A^{(k)}(\mathbf{x})}{k!} \left(\frac{\mathbf{x} - \mathbf{x}'}{h}\right)^k + O_{n+1}\left(\frac{\mathbf{x} - \mathbf{x}'}{h}\right)
\end{aligned}
\tag{2.10}
$$

where $O_{n+1}\left(\dfrac{\mathbf{x} - \mathbf{x}'}{h}\right)$ is the remainder which has an order higher than n

Substituting (2.10) in to (2.3) yields

$$
\begin{aligned}
A(\mathbf{x}) &= \int_{\Omega} \sum_{k=0}^{n} \frac{(-1)^k h^k A^{(k)}(\mathbf{x})}{k!} \left(\frac{\mathbf{x} - \mathbf{x}'}{h}\right)^k W(\mathbf{x} - \mathbf{x}', h) d\mathbf{x}' + O_{n+1}\left(\frac{\mathbf{x} - \mathbf{x}'}{h}\right) \\
&= \sum_{k=0}^{n} \frac{(-1)^k h^k A^{(k)}(\mathbf{x})}{k!} \int_{\Omega} \left(\frac{\mathbf{x} - \mathbf{x}'}{h}\right)^k W(\mathbf{x} - \mathbf{x}', h) d\mathbf{x}' + O_{n+1}\left(\frac{\mathbf{x} - \mathbf{x}'}{h}\right) \\
&= \sum_{k=0}^{n} I_k A^{(k)}(\mathbf{x}) + O_{n+1}\left(\frac{\mathbf{x} - \mathbf{x}'}{h}\right)
\end{aligned}
\tag{2.11}
$$

where

$$
I_k = \frac{(-1)^k h^k}{k!} \int_{\Omega} \left(\frac{\mathbf{x} - \mathbf{x}'}{h}\right)^k W(\mathbf{x} - \mathbf{x}', h) d\mathbf{x}'
$$

In order for Equation (2.11) to be valid for every $\mathbf{x}$, every coefficients I_k on the LHS must equal to their counterpart on the RHS, meaning that

$$\begin{cases} I_0 = \int_{\Omega} W(\mathbf{x}-\mathbf{x}',h)d\mathbf{x}' = 1 \\[2mm] I_1 = -h\int_{\Omega} \left(\dfrac{\mathbf{x}-\mathbf{x}'}{h} \right) W(\mathbf{x}-\mathbf{x}',h)d\mathbf{x}' = 0 \\[2mm] I_2 = \dfrac{h^2}{2}\int_{\Omega} \left(\dfrac{\mathbf{x}-\mathbf{x}'}{h} \right)^2 W(\mathbf{x}-\mathbf{x}',h)d\mathbf{x}' \\[2mm] \dots \\[2mm] I_n = \dfrac{(-1)^n h^n}{n!}\int_{\Omega} \left(\dfrac{\mathbf{x}-\mathbf{x}'}{h} \right)^n W(\mathbf{x}-\mathbf{x}',h)d\mathbf{x}' = 0 \end{cases} \qquad (2.12)$$

Because $h>0$, the above condition can be further simplified as

$$\begin{cases} M_0 = \int_{\Omega} W(\mathbf{x}-\mathbf{x}',h)d\mathbf{x}' = 1 \\[2mm] M_1 = \int_{\Omega} \left(\dfrac{\mathbf{x}-\mathbf{x}'}{h} \right) W(\mathbf{x}-\mathbf{x}',h)d\mathbf{x}' = 0 \\[2mm] M_2 = \int_{\Omega} \left(\dfrac{\mathbf{x}-\mathbf{x}'}{h} \right)^2 W(\mathbf{x}-\mathbf{x}',h)d\mathbf{x}' \\[2mm] \dots \\[2mm] M_n = \int_{\Omega} \left(\dfrac{\mathbf{x}-\mathbf{x}'}{h} \right)^n W(\mathbf{x}-\mathbf{x}',h)d\mathbf{x}' = 0 \end{cases} \qquad (2.13)$$

The form of the kernel function $W(\mathbf{x}-\mathbf{x}',h)$ is chosen in advance. The most commonly used

forms of kernel functions are single polynomials and piecewise polynomials.

For a single polynomial of order n, the following general form could be used

$$W(\mathbf{x}-\mathbf{x}',h) = W(q) = a_0 + a_1 q + a_2 q^2 + \dots + a_n q^n \qquad (2.14)$$

Here, a non-dimensional parameter q is used where $q = |\mathbf{x}-\mathbf{x}'|/h$. In order for the kth de-

rivative at $q=0$ to exists, the following condition must be satisfied

$$W^{(k)}(q=0) = \begin{cases} k!a_k & \mathbf{x}-\mathbf{x}' \to 0+ \\ (-1)^k k!a_k & \mathbf{x}-\mathbf{x}' \to 0- \end{cases} \tag{2.15}$$

$$k!a_k = (-1)^k k!a_k \tag{2.16}$$

$$\Leftrightarrow \quad a_k = 0 \quad k = 2i-1, \qquad i = 1,2,... \tag{2.17}$$

$$\Rightarrow \quad W(\mathbf{x}-\mathbf{x}',h) = W(q) = a_0 + a_2 q^2 + ... + a_{2i} q^{2i} \tag{2.18}$$

Substituting the Equation (2.18) of the kernel function in (2.13), one yields a system of linear equations with the unknown being the coefficients a_{2i}. The kernel function is fully determined after solving the linear system (2.13).

For piecewise polynomial, for example a 3 piece polynomial, the following form can be used for the kernel function

$$W(q) = \begin{cases} W_1(r) & 0 \le r < r_1 \\ W_2(r) & r_1 \le r < r_2 \\ 0 & r_2 \le r \end{cases} \tag{2.19}$$

Consider an nth order piecewise polynomial. The continuity conditions are required for the function itself and the first $n-1$ derivatives, thus leads to the following form for the kernel function

$$W(q) = \begin{cases} a_1(r_1-r)^n + a_2(r_2-r)^n & 0 \le r < r_1 \\ a_3(r_2-r)^n & r_1 \le r < r_2 \\ 0 & r_2 \le r \end{cases} \tag{2.20}$$

Following the similar approach as used for single polynomial and using the linear system (2.13), the unknown coefficients a_i in (2.20) are determined and so is the kernel function. In

the present research, the following kernel functions are used depending on the problems. These include the cubic spline kernel used for the sloshing problem and a fifth order kernel needed for high accuracy modeling of the transient wave breaking process. Sensitivity studies show that, in general, a higher order kernel can lead to spurious oscillations. The choice is therefore dependent partly on the validation of the simulation through comparisons with experimental results.

Gaussian

$$W(q) = \alpha_D e^{-q^2} \tag{2.21}$$

$\alpha_D = 1/(\pi h^2)$ in 2D and $\alpha_D = 1/(\pi^{3/2} h^3)$ in 3D
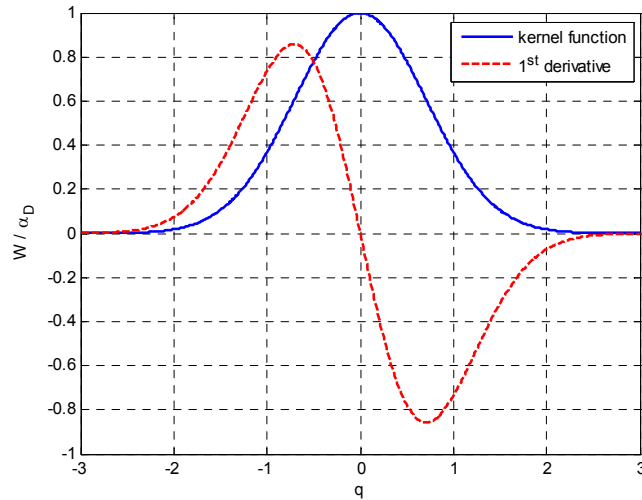
Figure 2.4. The Gaussian kernel function and its 1st derivative

Quadratic

$$W(q) = \alpha_D \left(\frac{1}{4} q^2 - q + 1 \right) \qquad 0 \le q \le 2 \tag{2.22}$$

$\alpha_D = 3/(4\pi h^2)$ in 2D and $\alpha_D = 3/(4\pi h^3)$ in 3D
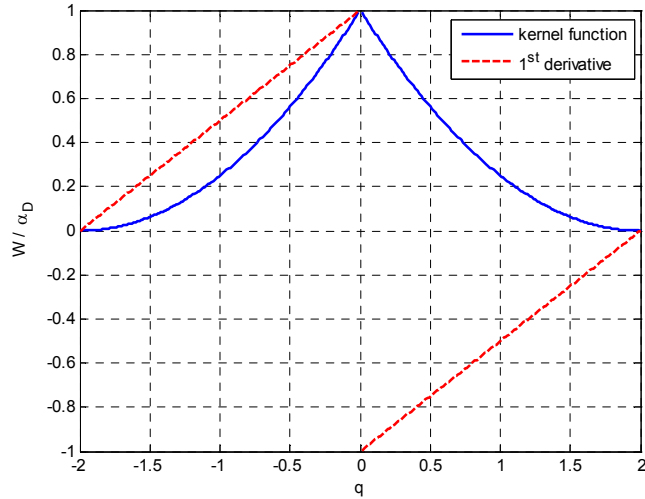
Figure 2.5. The quadratic kernel function and its 1st derivative

Cubic spline

$$W(q) = \alpha_D \begin{cases} \dfrac{3}{4}q^3 - \dfrac{3}{2}q^2 + 1 & 0 \le q < 1 \\[2mm] \dfrac{1}{4}(2-q)^3 & 1 \le q < 2 \\[2mm] 0 & q \ge 2 \end{cases} \tag{2.23}$$

$\alpha_D = 10/(7\pi h^2)$ in 2D and $\alpha_D = 1/(\pi h^3)$ in 3D
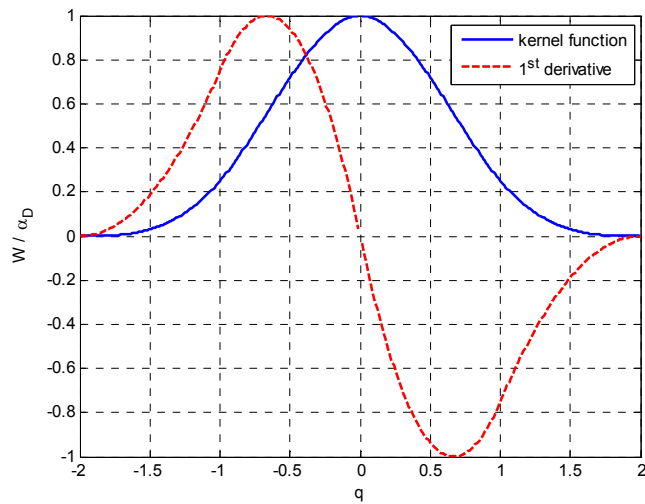
Figure 2.6. The cubic spline kernel function and its 1st derivative

Quintic

$$W(q) = \alpha_D \left(1 - \frac{q}{2}\right)^4 (2q+1) \quad 0 \leq q \leq 2 \tag{2.24}$$

$\alpha_D = 7/\left(4\pi h^2\right)$ in 2D and $\alpha_D = 7/\left(8\pi h^3\right)$ in 3D
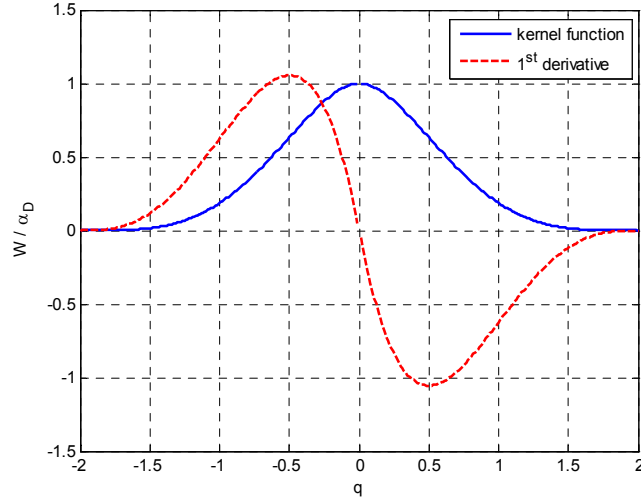
Figure 2.7. The quintic kernel function and its 1st derivative.

2.2.1.2 Kernel approximation of the governing equations

Neglecting the viscosity, turbulence and surface tension terms (they will be treated separately in the later sections) the Navier-Stokes equations are rewritten as

$$\frac{d\rho}{dt} = -\rho \nabla \cdot \mathbf{u} \tag{2.25}$$

$$\frac{d\mathbf{u}}{dt} = -\frac{1}{\rho}\nabla p + \mathbf{g} \tag{2.26}$$

Using the kernel approximation similar to Equation (2.7) and (2.8), the gradient of pressure and divergence of velocity can be approximated as

$$(\nabla p)_a = \sum_b \frac{m_b}{\rho_b} p_b \nabla_a W_{ab} \tag{2.27}$$

$$(\nabla \cdot \mathbf{u})_a = \sum_b \frac{m_b}{\rho_b} \mathbf{u}_b \cdot \nabla_a W_{ab} \tag{2.28}$$

Note that $(\nabla p)_a$ does not vanish if p is a constant which is inconsistent. However, if the pressure gradient and velocity divergence are approximated as

$$\nabla p = [\nabla p] - p[\nabla 1] \tag{2.29}$$

$$\nabla \cdot \mathbf{u} = [\nabla \cdot \mathbf{u}] - \mathbf{u} \cdot [\nabla 1] \tag{2.30}$$

and $\nabla 1$ can be further approximated as

$$\nabla 1 = \sum_b \frac{m_b}{\rho_b} \nabla_a W_{ab} \tag{2.31}$$

Following Equation (2.7) and (2.8), the pressure gradient and velocity divergence can be expressed as

$$(\nabla p)_a = \sum_b \frac{m_b}{\rho_b} (p_b - p_a) \nabla_a W_{ab} \tag{2.32}$$

$$(\nabla \cdot \mathbf{u})_a = \sum_b \frac{m_b}{\rho_b} (\mathbf{u}_b - \mathbf{u}_a) \cdot \nabla_a W_{ab} \tag{2.33}$$

Equation (2.32) will ensure that the gradient vanishes if p is a constant. A drawback of Equation (2.32) and (2.33) is that when approximating the pressure forces, linear and angular momentum are not conserved exactly (Morris, 1996).

For higher accuracy, the following expressions of the gradient of pressure and divergence of velocity may be used

$$\frac{\nabla p}{\rho} = \left[\nabla\left(\frac{p}{\rho}\right)\right] + \frac{p}{\rho^2}[\nabla\rho] \tag{2.34}$$

$$\rho\nabla\cdot\mathbf{u} = [\nabla\cdot(\rho\mathbf{u})] - \mathbf{u}\cdot[\nabla\rho] \tag{2.35}$$

Using the kernel approximation (2.7) and (2.8) for the terms in square brackets, we have

$$\left(\frac{\nabla p}{\rho}\right)_a = \left[\sum_b \frac{m_b}{\rho_b}\left(\frac{p_b}{\rho_b}\right)\nabla_a W_{ab}\right] + \left(\frac{p}{\rho^2}\right)_a\left[\sum_b \frac{m_b}{\rho_b}(\rho_b)\nabla_a W_{ab}\right]$$

$$= \sum_b m_b\left(\frac{p_a}{\rho_a^2} + \frac{p_b}{\rho_b^2}\right)\nabla_a W_{ab}$$

$$\Rightarrow \quad (\nabla p)_a = \rho_a\sum_b m_b\left(\frac{p_a}{\rho_a^2} + \frac{p_b}{\rho_b^2}\right)\nabla_a W_{ab} \tag{2.36}$$

$$(\rho\nabla\cdot\mathbf{u})_a = \left[\sum_b \frac{m_b}{\rho_b}(\rho_b\mathbf{u}_b)\cdot\nabla_a W_{ab}\right] - \mathbf{u}_a\cdot\left[\sum_b \frac{m_b}{\rho_b}\rho_b\nabla_a W_{ab}\right]$$

$$= \sum_b m_b(\mathbf{u}_b - \mathbf{u}_a)\cdot\nabla_a W_{ab}$$

$$\Rightarrow \quad (\nabla\cdot\mathbf{u})_a = \frac{1}{\rho_a}\sum_b m_b(\mathbf{u}_b - \mathbf{u}_a)\cdot\nabla_a W_{ab} \tag{2.37}$$

Equation (2.36) and (2.37) only work for problems with one phase flow or two-phase with small difference of density. In one phase flow problems, the density gradient across the free surface is large. However, the pressure will dismiss to zeros, $p\rightarrow 0$, when moving across the free surface, then the last term of (2.34) vanishes and the large gradient of density at free surface is cancelled out. In two phase flow problem, we do not have situation of $p\rightarrow 0$ at the interface. The pressure changes (unless surface tension is considered) across the interface to a nonzero. However, with small density gradient across the interface, the last term of (2.34) is

kept in a stable range. A study by Colagrossi and Landrini (2003) has concluded that the SPH formulation using (2.36), (2.37) will not work for the cases of density ratio less than 0.1.

The main source of numerical instabilities that limit the application of SPH to two-phase flow with large density difference is the sharp gradient of density at the interface. To prevent this, the following expressions are used in this thesis

$$\frac{\nabla p}{\rho} = \frac{1}{\rho}[\nabla p] + \frac{p}{\rho}[\nabla 1] \tag{2.38}$$

$$\nabla \cdot \mathbf{u} = [\nabla \cdot \mathbf{u}] - \mathbf{u} \cdot [\nabla 1] \tag{2.39}$$

Using the kernel approximation (2.7) and (2.8) for the terms in square brackets, we can yield

$$\left(\frac{\nabla p}{\rho}\right)_a = \frac{1}{\rho_a}\left[\sum_b \frac{m_b}{\rho_b} p_b \nabla_a W_{ab}\right] + \left(\frac{p}{\rho}\right)_a \left[\sum_b \frac{m_b}{\rho_b} \nabla_a W_{ab}\right]$$

$$= \sum_b m_b \left(\frac{p_a}{\rho_a \rho_b} + \frac{p_b}{\rho_a \rho_b}\right)\nabla_a W_{ab}$$

$$\Rightarrow \quad (\nabla p)_a = \rho_a \sum_b m_b \left(\frac{p_a}{\rho_a \rho_b} + \frac{p_b}{\rho_a \rho_b}\right)\nabla_a W_{ab} \tag{2.40}$$

$$(\nabla \cdot \mathbf{u})_a = \left[\sum_b \frac{m_b}{\rho_b} \mathbf{u}_b \cdot \nabla_a W_{ab}\right] - \mathbf{u}_a \cdot \left[\sum_b \frac{m_b}{\rho_b} \nabla_a W_{ab}\right]$$

$$= \sum_b \frac{m_b}{\rho_b}(\mathbf{u}_b - \mathbf{u}_a)\cdot \nabla_a W_{ab}$$

$$\Rightarrow \quad (\nabla \cdot \mathbf{u})_a = \sum_b \frac{m_b}{\rho_b}(\mathbf{u}_b - \mathbf{u}_a)\cdot \nabla_a W_{ab} \tag{2.41}$$

The density in the continuity equation can be approximated either by

$$\rho_a = \sum_b m_b W_{ab} \tag{2.42}$$

or $\dfrac{d\rho_a}{dt} = -\rho_a \sum_b \dfrac{m_b}{\rho_b}\left(\mathbf{u}_b - \mathbf{u}_a\right)\cdot\nabla_a W_{ab}$ (2.43)

Most SPH calculations use (2.42). However, when (2.42) is used in simulating interfacial flow, the density would have dropped near the interface causing pressure oscillations. Equation (2.43) gives a better representation of density and pressure at the interface.

The above derivation assumes that there is no source or sink. When a problem involves sources and sinks, an additional term is added into the continuity equation. If the source function is $f(\mathbf{x})$, then its kernel approximation is

$$f_a = \sum_b \dfrac{m_b}{\rho_b} f_b W_{ab}$$ (2.44)

2.2.1.3 Kernel approximation for air-water flow

From the discussion above, the governing equations for air-water flow in the kernel approximation will take the form of

$$\dfrac{d\rho_a}{dt} = -\rho_a \sum_b \dfrac{m_b}{\rho_b}\left(\mathbf{u}_b - \mathbf{u}_a\right)\cdot\nabla_a W_{ab}$$ (2.45)

$$\dfrac{d\mathbf{u}_a}{dt} = -\sum_b m_b\left(\dfrac{p_a}{\rho_a\rho_b} + \dfrac{p_b}{\rho_a\rho_b}\right)\nabla_a W_{ab} + \mathbf{g}_a$$ (2.46)

Position of the particles is updated by

$$\dfrac{d\mathbf{x}_a}{dt} = \mathbf{u}_a$$ (2.47)

Equations (2.45)- (2.47) approximate the governing equations for 2D air-water flow problems. However, it is also applicable for 3D air-water flow problems.

2.2.2   Equation of state

In real fluids such as water, the speed of sound is very large compared to fluid velocity (~1500 m/s compared to ~10 m/s). For this reason, numerical methods treat the water as incompressible to simplify the governing equations. Pressure can be computed explicitly or implicitly from the fluid density. In implicit calculation, a Poisson equation of pressure need to be solved and the condition of incompressibility can be strictly satisfied. Implicit calculation of pressure will involve solving a system of linear equations which is computationally expensive. It also requires an explicit definition of the free surface where the boundary condition of pressure is applied. The definition of the free surface in particle methods is very sensitive to the pressure calculation and still remains a challenge. In explicit calculation, the pressure is directly updated as a function of density and thus no free surface definition is required and computational cost is much cheaper. However, only quasi-incompressible condition is achieved by adapting an artificial equation of state. This approach is usually referred to as weakly-compressible. It is more convenient to use explicit equation of state to simulate gas-liquid problems such as air-water since the compressible condition is easily applied for gas phase while the compressibility of water could be controlled. The following equation of state suggested by Batchelor (1967) is used

$$p(\rho) = B\left[\left(\frac{\rho}{\rho_o}\right)^{\gamma} - 1\right] + p_o \tag{2.48}$$

where, p_o is background pressure (sometimes called atmospheric pressure) and usually set zero. The reference density of fluid is ρ_o ($\rho_o = 997\,kg/m^3$ for water and $\rho_o = 1.2\,kg/m^3$ for air). The coefficient γ determines the response of pressure changes to the density variation. In water, $\gamma = 7$ is used hence a very large pressure can only make small change to density. This condition brings the water to nearly incompressible. In air, the condition is compressible

so a large variation of pressure can lead to a significant change in the density. Hence, a small value of γ is chosen. Here, $\gamma=1.4$ is used for air.

The subtraction of 1 in the equation of state is to ensure that the relative pressure is zero if the density equals to the reference density; and the fluid stays at rest. This helps to remove spurious boundary effect at the free surface.

The coefficient B in the equation of state is used to control the compressibility of the fluid. It is a function of the compressibility and density of the fluid. The derivation of B is as follows. Since the density variation is proportional to square of the Mach number

$$\frac{|\delta\rho|}{\rho} \propto \left(\frac{V_{max}}{c_s}\right)^2 \qquad (2.49)$$

where V_{max} is the maximum speed of fluid and c_s is the sound speed in the fluid which is computed as

$$c_s = \sqrt{\left.\frac{\partial p}{\partial \rho}\right|_{\rho_o}} = \sqrt{\frac{B\gamma}{\rho_o}} \qquad (2.50)$$

Assuming that

$$\frac{|\delta\rho|}{\rho} = \left(\frac{V_{max}}{c_s}\right)^2 \leq \delta_{max} \qquad (2.51)$$

$$\Leftrightarrow \quad \frac{\rho_o V_{max}^2}{B\gamma} \leq \delta_{max}$$

$$\Rightarrow \quad B \geq \frac{\rho_o V_{max}^2}{\delta_{max}\gamma} \qquad (2.52)$$

Given the actual sound speed in water, the density variation, δ_{max}, is very small and thus a very large value of B is required. However, the computational time step will be extremely small since it is inversely proportional to the sound speed (as discussed later in Section 2.3.7). Small time step will deteriorate the efficiency of the computation. Hence, in actual simulations, the value of B is chosen so that the density variation and sound speed are within desired ranges. This sound speed used in the computation is called artificial sound speed and is not necessary equal to the actual sound speed. Similarly, an artificial sound speed is also used for the simulation of air.

For cases with large density difference such as between air and water, the density variation in air, δ_{max}, is larger due to larger compressibility. However the air density is much smaller than water density. Therefore, from Equation (2.52), the reference pressure for water is larger than that for air.

In two-phase flow, the pressure at the interface has to satisfy the dynamic boundary condition ($p = p_A$). Since the lighter fluid has smaller value of γ, the pressure-density steepness ($\partial p / \partial \rho$) has to be larger than that of heavier fluid in order to maintain a small gradient across the interface. Moreover, the pressure-density steepness equals to square of the sound speed, i.e. $\partial p / \partial \rho = c_s^2(\rho)$. Therefore, the numerical sound speed in lighter fluid is larger than that in heavier fluid (although in reality, sound speed in water is larger than that in air). A simple mathematical and graphical proof for air-water case is as follows. Rewriting the equation of state, we has

$$p(\rho) = B\left[\left(1 + \frac{d\rho}{\rho_o}\right)^{\gamma} - 1\right] + p_o \qquad (2.53)$$

At the interface, the dynamic condition requires $p_W = p_A$ yielding

$$B_W \left[\left(1 + \left(\frac{d\rho}{\rho_o} \right)_W \right)^{\gamma_W} - 1 \right] = B_A \left[\left(1 + \left(\frac{d\rho}{\rho_o} \right)_A \right)^{\gamma_A} - 1 \right] \tag{2.54}$$

$$\Rightarrow \quad \frac{B_A}{B_W} = \frac{\left(1 + \left(\frac{d\rho}{\rho_o} \right)_W \right)^{\gamma_W} - 1}{\left(1 + \left(\frac{d\rho}{\rho_o} \right)_A \right)^{\gamma_A} - 1} \tag{2.55}$$

$$\Rightarrow \quad \frac{c_{sA}}{c_{sw}} = \sqrt{\frac{\gamma_A \rho_{oW}}{\gamma_W \rho_{oA}}} \sqrt{\frac{B_A}{B_W}} \tag{2.56}$$

Here, subscripts $_A$ and $_W$ are meant for air and water particles. With $(d\rho/\rho_o)_W = [-1\%, 1\%]$ and $(d\rho/\rho_o)_A = \alpha(d\rho/\rho_o)_W$, $\alpha = 1, 5, 10, 15, 20$, Figure 2.8 show the values of B_A/B_W and c_{sA}/c_{sW} as functions of $(d\rho/\rho_o)_W$ at different α
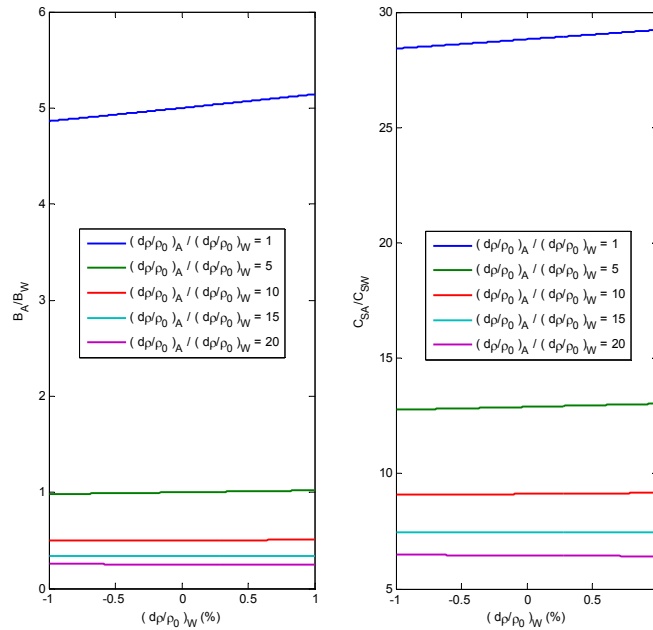
Figure 2.8. Variations of B_A/B_W and c_{sA}/c_{sW} as functions of $(d\rho/\rho_0)_W$ at different α.

By using the equation of state in SPH, the computed pressures are propagated in the fluid through the changes in the particle densities. The pressure propagation speed is equal to the artificial sound speed. The computed pressures are the actual pressures of the fluids. However, the computed particle densities do not necessarily represent the actual densities of the fluids. In SPH, the particle densities are intermediate values to compute the pressures. It is worth to point out that the equation of state is generally not applicable for liquids. However, in SPH the use of equation of state for a fluid is adequate since it is applied on an intermediate value of fluid density which is not fluid actual density, and the compressibility of the fluid is controlled by the choice of *B* or the artificial sound speed.

2.2.3 Viscosity

In SPH, viscosity is usually referred to artificial or laminar viscosity. While, the laminar viscosity is a characteristic of real fluid (i.e. real viscosity), the artificial viscosity has no relation to the real viscosity of the fluid and is introduced in the momentum equation to allow shock phenomena to be simulated. Lucy (1977) firstly introduced an artificial bulk viscosity to prevent a slow build-up of acoustic energy from integration errors in an SPH simulation. Monaghan and Gingold (1983) introduced a more effective viscosity which conserves linear and angular momentum. This viscosity model is then widely used in many applications of shock problems involving gases, liquids and solids. In some simulations without a shock wave, artificial viscosity is also introduced to stabilize the solution. In SPH, artificial viscosity is incorporated in the momentum equation as

$$\frac{d\mathbf{u}_a}{dt} = -\sum_b m_b \left(\frac{p_a}{\rho_a \rho_b} + \frac{p_b}{\rho_a \rho_b} + \Pi_{ab} \right) \nabla_a W_{ab} + \mathbf{g}_a \qquad (2.57)$$

$$\text{where } \Pi_{ab} = \begin{cases} \dfrac{-\alpha \bar{c}_{ab}\mu_{ab} + \beta\mu_{ab}^2}{\bar{\rho}_{ab}} & \text{if } \mathbf{u}_{ab} \cdot \mathbf{r}_{ab} < 0 \\ \\ 0 & \text{otherwise} \end{cases} \tag{2.58}$$

$$\mathbf{r}_{ab} = \mathbf{x}_b - \mathbf{x}_a$$

$$\mu_{ab} = \frac{h\mathbf{u}_{ab} \cdot \mathbf{r}_{ab}}{\mathbf{r}_{ab}^2 + 0.01h^2} \tag{2.59}$$

and $\bar{\rho}_{ab} = (\rho_a + \rho_b)/2$ and $\bar{c}_{ab} = (c_a + c_b)/2$ are the mean density and sound speed, respectively. The term $0.01h^2$ is to maintain a nonzero denominator while the term $\beta\mu_{ab}^2$ is to handle high Mach shocks. Values of α and β are suggested to be 1 and 2 by Monaghan (1992), respectively. The artificial viscosity was used in many SPH simulations in the past as well as some test cases in this study. However, in the simulation of wave breaking, we use laminar and turbulence viscosity which are popular in Eulerian gridded methods. The viscosity coefficients used in gridded methods are used in SPH.

The laminar viscosity appears in the right hand side of the momentum equation as

$$\frac{d\mathbf{u}}{dt} = -\frac{1}{\rho}\nabla p + \left(\frac{1}{\rho}\nabla.\mu\nabla\right)\mathbf{u} + \mathbf{g} \tag{2.60}$$

where $\mu = \rho\nu$ is the dynamic viscosity, ν is the kinematic viscosity. The SPH approximation of laminar viscosity has the form of (Morris et al., 1997)

$$\left[\left(\frac{1}{\rho}\nabla.\mu\nabla\right)\mathbf{u}\right]_a = \sum_b \frac{m_b}{\rho_a\rho_b}\frac{(\mu_a + \mu_b)\mathbf{r}_{ab} \cdot \mathbf{u}_{ab}}{\mathbf{r}_{ab}^2 + 0.01h^2} \cdot \nabla_a W_{ab} \tag{2.61}$$

Assuming $\nu = \nu_o$ is a constant the above expression can be further simplified

$$\left[\left(\frac{1}{\rho}\nabla.\mu\nabla\right)\mathbf{u}\right]_a = \sum_b \frac{m_b}{\rho_a\rho_b} \frac{v_o(\rho_a+\rho_b)\mathbf{r}_{ab}\cdot\mathbf{u}_{ab}}{\mathbf{r}_{ab}^2+0.01h^2}\cdot\nabla_a W_{ab}$$

$$= v_o\sum_b m_b\left(\frac{1}{\rho_a}+\frac{1}{\rho_b}\right)\frac{\mathbf{r}_{ab}\cdot\mathbf{u}_{ab}}{\mathbf{r}_{ab}^2+0.01h^2}\cdot\nabla_a W_{ab}$$

(2.62)

For two-phase flows, the summation in Equation (2.62) is performed over particles belongs to the same fluid, regardless the other fluid even they are at the interface.

Comparing the SPH formations for artificial viscosity in (2.57), (2.58) and (2.59) and laminar viscosity (2.62), there is a term $\alpha\bar{c}_{ab}h$ in $\prod_{ab}$ being equivalent to the kinematic viscosity v_o. This remark can be used to estimate the value of α such that the artificial viscosity can be used in lieu of the real one.

2.2.4 Turbulence

For wave breaking problems, the main source of turbulence is due to the breaking of the wave where most of wave energy is dissipated quickly. For problems with non-breaking wave, turbulence is also generated in the fluid where shear stress is large enough. The shear stress in a fluid is characterized by a Reynolds number which is a function of length scale of the wave, fluid velocity and viscosity. According to Gotoh et al., (2001), problems involving fluid velocity of 50 – 100 times of wave period usually need accurate simulation of turbulence.

This SPH turbulence model uses the concept of Large Eddy Simulation (LES) where the large scale turbulence (particle scale – PS) is computed directly in the numerical simulation and the small scale (sub-particle scale – SPS) stresses are modelled using subgrid-scale model (SGS). By using a filtering, the velocity is presented by a summation of a PS component $\bar{u}$ and a SPS component u' as

$$u_i = \bar{u}_i + u'_i \tag{2.63}$$

The particle scale momentum equation can be written as

$$\frac{d\bar{\mathbf{u}}}{dt} = -\frac{1}{\rho}\nabla\bar{p} + \left(\frac{1}{\rho}\nabla.\mu\nabla\right)\bar{\mathbf{u}} + \mathbf{g} + \frac{1}{\rho}\nabla.\bar{\boldsymbol{\tau}} \tag{2.64}$$

where $\bar{\tau}$ is SPS Reynolds turbulence stress which is represented by a eddy viscosity model in tensor notation as

$$\bar{\tau}_{ij} = \rho\overline{u'_i u'_j} = \rho\nu_t\left(\frac{\partial\bar{u}_i}{\partial x_j} + \frac{\partial\bar{u}_j}{\partial x_i}\right) - \frac{2}{3}\rho k\delta_{ij} \tag{2.65}$$

in which ν_t is kinematic eddy viscosity; k is turbulence energy; and δ_{ij} is Kronecker's delta.

With Δ being the filter width (equal to initial particle spacing), the kinematic eddy viscosity and the energy dissipation are

$$\nu_t = C_\nu k^{1/2}\Delta \tag{2.66}$$

$$\varepsilon = \frac{C_\varepsilon k^{3/2}}{\Delta} \tag{2.67}$$

Where the constants C_ν, C_ε are chosen as 1.0 and 0.08 respectively (Gotoh et al., 2001).

Assuming the local equilibrium condition of the SPS turbulence (Gotoh et al., 2001)

$$\overline{u'_i u'_j}\frac{\partial\bar{u}_i}{\partial x_j} = \nu_t\left(\frac{\partial\bar{u}_i}{\partial x_j} + \frac{\partial\bar{u}_j}{\partial x_i}\right)\frac{\partial\bar{u}_i}{\partial x_j} = \varepsilon \tag{2.68}$$

Defining of P_r as $P_r = \left(\frac{\partial\bar{u}_i}{\partial x_j} + \frac{\partial\bar{u}_j}{\partial x_i}\right)\frac{\partial\bar{u}_i}{\partial x_j}$ \tag{2.69}

the kinematic eddy viscosity and turbulence energy can be expressed as

$$v_t = (C_s \Delta)^2 P_r^{1/2} \tag{2.70}$$

$$k = \frac{C_v}{C_\varepsilon} \Delta^2 P_r \tag{2.71}$$

here C_s is Smagorinsky constant, $C_s = \sqrt{C_v^{3/2} C_\varepsilon^{-1/2}}$.

In SPH simulation of 2D flow, the above tensor notations are rewritten in normal form as

$$\bar{\tau}_{xx} = 2\rho v_t \frac{\partial \bar{u}}{\partial x} - \frac{2}{3}\rho k \tag{2.72}$$

$$\bar{\tau}_{yy} = 2\rho v_t \frac{\partial \bar{v}}{\partial y} - \frac{2}{3}\rho k \tag{2.73}$$

$$\bar{\tau}_{xy} = \rho v_t \left(\frac{\partial \bar{u}}{\partial y} + \frac{\partial \bar{v}}{\partial x} \right) \tag{2.74}$$

$$(\nabla.\bar{\tau})_x = \frac{\partial}{\partial x}\bar{\tau}_{xx} + \frac{\partial}{\partial y}\bar{\tau}_{xy} \tag{2.75}$$

$$(\nabla.\bar{\tau})_y = \frac{\partial}{\partial x}\bar{\tau}_{xy} + \frac{\partial}{\partial y}\bar{\tau}_{yy} \tag{2.76}$$

$$P_r = 2\left(\frac{\partial \bar{u}}{\partial x} \right)^2 + 2\left(\frac{\partial \bar{v}}{\partial y} \right)^2 + \left(\frac{\partial \bar{u}}{\partial y} + \frac{\partial \bar{v}}{\partial x} \right)^2 \tag{2.77}$$

The SPH expression of the SPS term in two-phase flow simulation is

$$\left(\frac{1}{\rho}\nabla.\bar{\tau} \right)_a = \sum_b m_b \left(\frac{\bar{\tau}_a + \bar{\tau}_b}{\rho_a \rho_b} \right) \cdot \nabla_a W_{ab} \tag{2.78}$$

2.3   Implementation of SPH

2.3.1   Boundary conditions

In normal fluid dynamic applications, free surfaces and solid walls (fixed and moving walls) are commonly used. In problems involving multiple scales, due to the complexity and size of problem, nesting and periodic boundary conditions are applied.

An accurate treatment of the boundary condition is crucial for a successful SPH simulation. A typical calculation pertaining to a specific particle always requires a complete support domain, i.e. the support domain filled with particles. However, due to the termination or discontinuity of the computation domain at the boundaries, there will be an absence of particles on one side of the boundaries (see Figure 2.9). For completion of the support domain, in particular, to facilitate the computation of the kernel approximation for particles located near or on the boundary, one of the possible approaches is to add in fictitious particles. The use of fictitious particles is different for different types of boundaries. In this thesis, four types of boundary conditions are implemented and described as below.
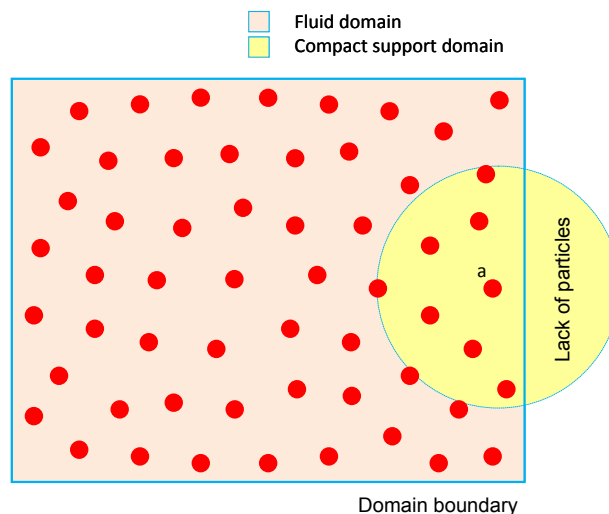
Figure 2.9. Insufficient particles inside the compact support domain of particle 'a' (indicated by the yellow circle)

2.3.1.1   Free surface condition

Fictitious particles at the free surface are difficult to implement as the free surface has arbitrary and changing shapes. In many practical applications such as the simulation of water waves, the error due to the neglect of air particles above the free surface is expected to be very small. This is largely because of the significant difference in the density of air and water. However, if the air is compressed at high pressure, such as in the case of entrapped air inside a plunging jet, the neglect of air particles will significantly affect the SPH approximation at the water surface. For such a scenario, a two-phase flow simulation comprising both water and air particles should be used and fictitious particles are not required at the interface of two fluids since the compact support domain of a particle at the interface is completely filled by particles from the both fluids.

2.3.1.2   Solid boundary condition

In some SPH simulations, solid boundaries are approximated by a set of particles analogous to fluid particles. The boundary particles representing the solid boundaries also carry the properties of mass, density, pressure and velocity. These properties of the boundary particles are either calculated using SPH approximations or extrapolated from fluid particles. The dummy particle method (Crespo et al., 2007) widely used in the past is of this type. In this method, solid walls are represented by several layers of particles distributed uniformly within a distance of $2h$ outward of the fluid domain. A schematic drawing of the dummy particles at a solid boundary is shown in Figure 2.10. In this method, the boundary particles are treated equivalently to other fluid particles in the continuity and momentum equations. However, these boundary particles are forced to remain in fixed position (for the case of fixed solid walls) or to move according to an externally imposed function (for the case of moving solid walls such as a gate or wave paddle). The equation of state of the heavier fluid is usually used

for the pressure-density calculation for boundary particles at the layers nearer to the fluid. Properties of outer layer particles are extrapolated from the inner layer particles. The condition of zero normal velocity is applied by setting normal velocity of boundary particles to zero. The free-slip and non-slip conditions are imposed by forcing the tangential velocity component of the boundary particles to be non-zero or zero.

The dummy particle method is simple to implement. The major disadvantages of the method, however, are the low accuracy of the SPH approximation near a solid boundary. In many cases, fluid particles are detached from the solid boundary. An alternative method to approximate solid boundaries is ghost particle method which is implemented in this study.
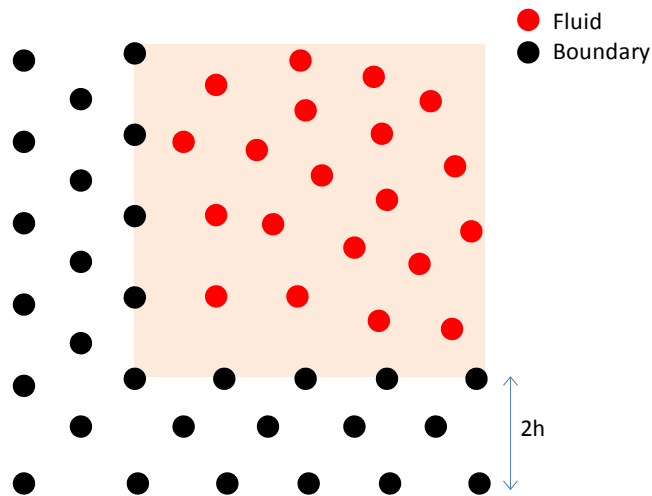
Figure 2.10. Distribution of dummy solid particles and nearby fluid particles

The ghost particle method provides a better representation of the solid boundary. In this method, a solid boundary is represented by a straight line or a curve. The outer region of the solid boundary is filled by a set of the so-called "ghost" particles (see Figure 2.11 and Figure 2.12). Essentially, the ghost particles are the "image" or the "mirror" of the fluid particles on the other side of the solid boundary through the boundary itself. Only fluid particles with in a distance of $2h$ from the solid boundary are mirrored. At the corner where the two solid

boundaries intersect, the fluid particles in the corner area are mirrored about the two bounda-ries and the intersection point as well. Properties of the ghost particle, a_G, are extrapolated from their physical counterpart, a, as follows:

The position of the ghost particle is updated according to the positions of the boundary and fluid particle a

$$\mathbf{x}_{a_G} = 2\mathbf{x}_B - \mathbf{x}_a \qquad (2.79)$$

where $\mathbf{x}_B$ is the mirror point which is either the perpendicular projection of $\mathbf{x}_a$ on the boundary or the intersection point of the two boundaries.

The distances between the fluid particles and the nearest solid boundaries are around a half of the initial particle size. Hence, after mirroring, the distance between a particle and its ghost is around one grid size.

In many SPH applications in the past, the pressure and density of ghost particles are set equal to that of the fluid counterparts. In this application, a more consistent approach is used. The pressure of the ghost particle a_G is extrapolated from fluid particle a by using the hydrostatic hypothesis. Then the density of particle a_G is calculated from its pressure using the inverse of the equation of state. The equations are as follows:

$$p_{a_G} = p_a + \rho_a \mathbf{g}\left(\mathbf{x}_{a_G} - \mathbf{x}_a\right) \qquad (2.80)$$

$$\rho_{a_G} = \left(\rho_o\right)_a \left(\frac{p_{a_G} - p_o}{B_a} + 1\right)^{\frac{1}{\gamma_a}} \qquad (2.81)$$

Here the subscriptions a and a_G mean the parameters are defined at particles a and a_G. The velocity of the ghost particle a_G is calculated from its physical counterpart a, depending on the slip condition applied at the boundary. The equations are

$$u_{na_G} = 2u_{nB} - u_{na} \tag{2.82}$$

$$u_{ta_G} = (1 - \alpha_s)u_{tB} + \alpha_s u_{ta} \tag{2.83}$$

Here, the subscripts n and t are the normal and tangential velocity components with respect to the instantaneous position of the boundary; u_{nB} and u_{tB} are the normal and tangential velocity components at the mirror point $\mathbf{x}_B$ on the boundary; α_s is the slip coefficient, $\alpha_s = 1$ for free-slip condition and $\alpha_s = -1$ for non-slip condition. An intermediate slip condition is modelled by a value of α_s between -1 and 1. In the corner region, the non-slip condition is always used.

Figure 2.11 and Figure 2.12 show the free-slip and non-slip conditions, respectively. Figure 2.11 to Figure 2.13 show the distribution of ghost particles used for different types of domain corners that the present SPH model can handle. Those include right convex, obtuse convex and right concave angles. The acute angle requires more complex treatment and is not presented here.
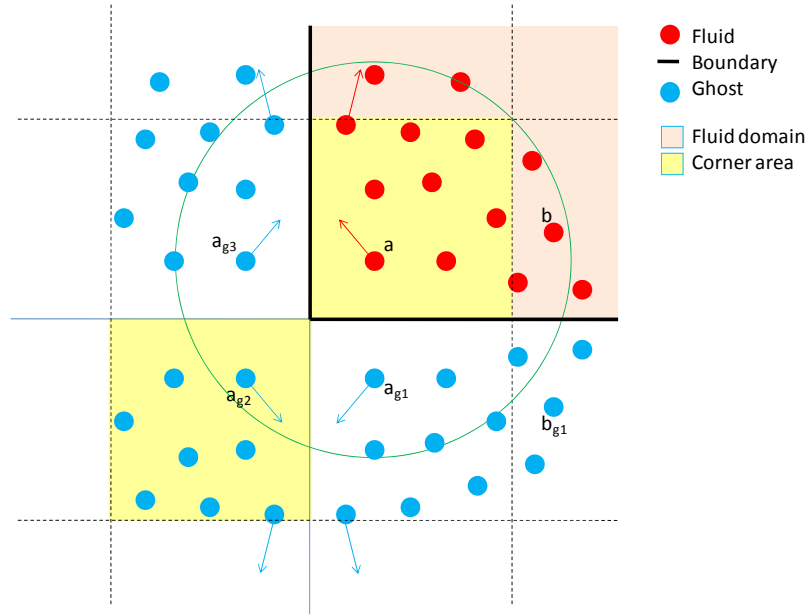
Figure 2.11. Distribution of ghost particles for a right, convex angle. A free-slip type of boundary condition is imposed.
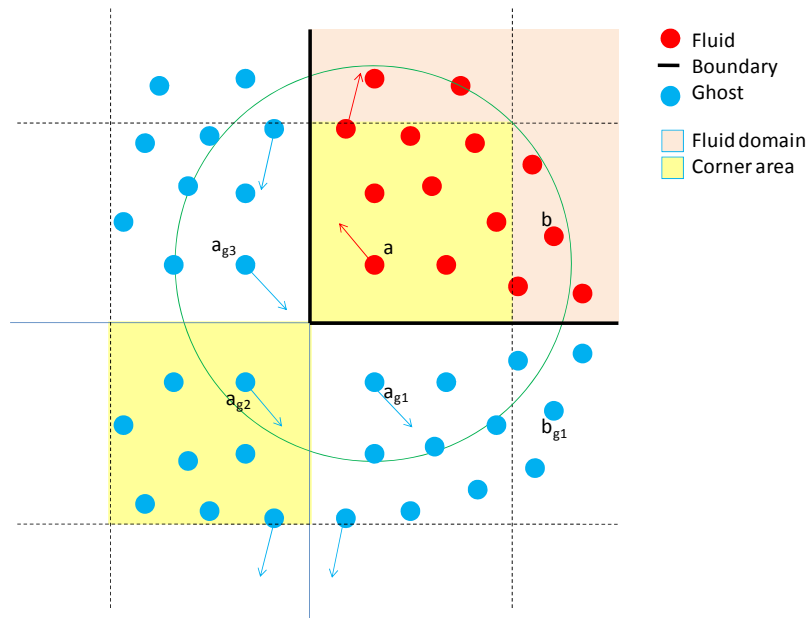
Figure 2.12. Distribution of ghost particles for a right, convex angle. A non-slip type of boundary condition is imposed.
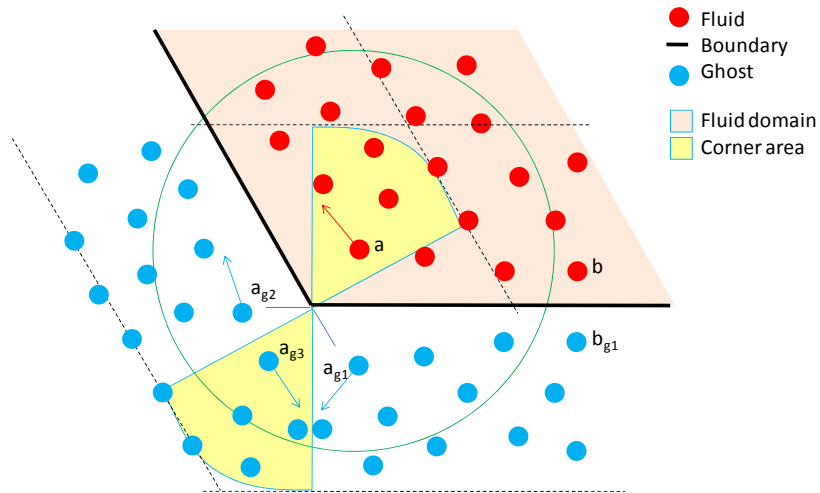
Figure 2.13. Distribution of ghost particles for an obtuse, convex angle. A free-slip type of boundary condition is imposed.
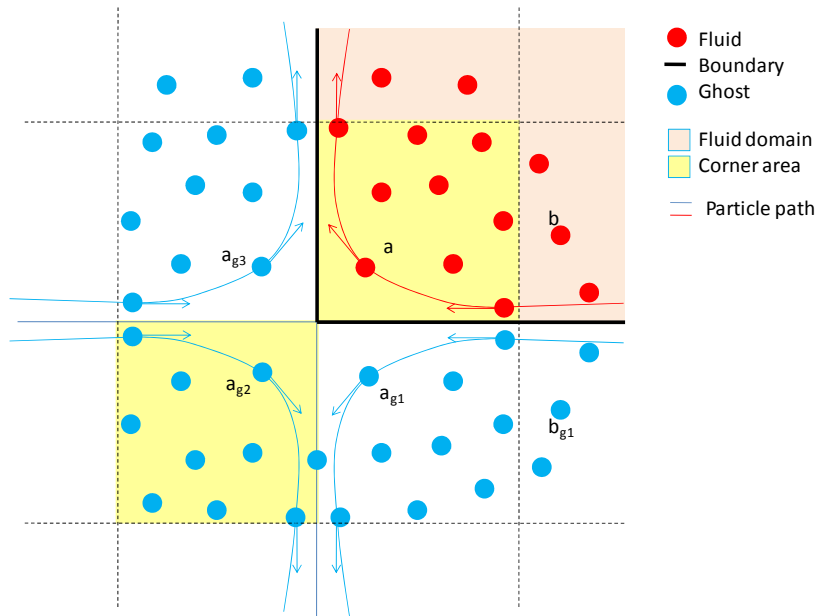
Figure 2.14. Continuity of a ghost particle's trajectory (red and blue solid lines).

The above mirror patterns to create ghost particles ensure that the trajectory of a ghost particle is continuous (Figure 2.14). Since the ghost particles contribute to fluid particles through the SPH approximation, any discontinuity in their paths may cause discontinuity in the prop-

erties of fluid particles. To create ghost particles near a right concave corner, the following procedure is proposed. The fluid area around the concave corner is divided into 3 sub-areas, namely area 1, 2 and 3 as shown in Figure 2.15. Particles in area 1 and area 2 are mirrored about the nearest boundary lines while particles in area 3 (corner area) are mirrored about the corner point. By doing so, the outer region at the corner is over-mirrored. In the SPH computation, a fluid particle in each area will have interactions with fluid particles in neighbouring areas as usual. In addition, fluid particles in each area will receive contributions from ghosts of particles in the same area but not from ghosts of particles in other areas. For example, a fluid particle in area 3 will have interactions with fluid particles in neighbouring areas 1 and 2. It will also have contributions from ghosts of particles in area 3. Using this mirroring procedure, the continuity of the ghost particles' paths is assured, as demonstrated by the green and red dashed lines in Figure 2.15. In this study, no concave corner is involved; thus this mirroring procedure has not implemented.
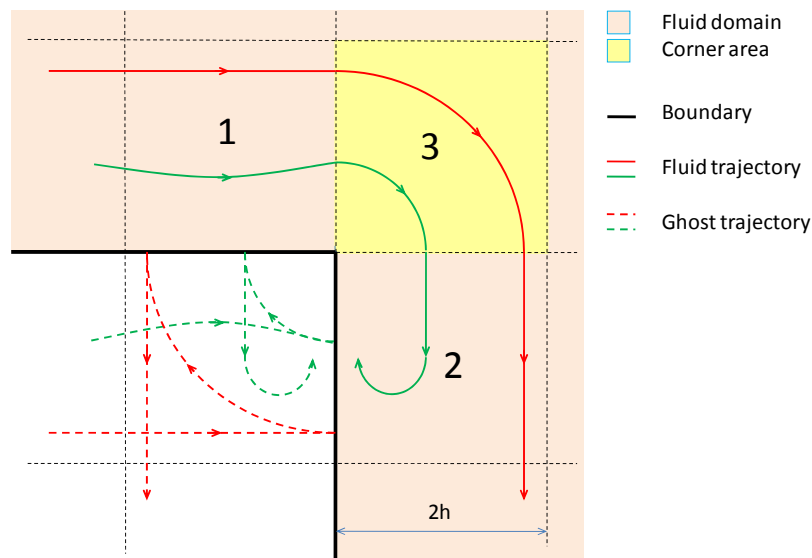
Figure 2.15. Mirror of particle trajectories near a right, concave angle. A free-slip type of boundary condition is imposed.

In certain situations, for example water particles at both sides of a wave paddle, a fluid particle locates within the compact support domain of another particle but the connection line between the two particles is crossed by a solid boundary. In these cases, one particle and its ghosts will have no influence on the other.

2.3.1.3 Lateral periodic boundary condition

The lateral periodic open boundary condition is applied when the flow condition at one lateral boundary is required to be identical to that at the other lateral boundary. In the SPH context, this essentially means: (1) a particle near a lateral boundary has interaction with particles in a complementary area near the lateral boundary on the other side of the domain; (2) a particle leaving the computation domain at one side will enter the same domain from the other side. This is demonstrated in Figure 2.16 where water particle a lies near the right boundary and therefore its compact support domain extends beyond the boundary and extrudes into the domain through the left boundary (yellow patches).
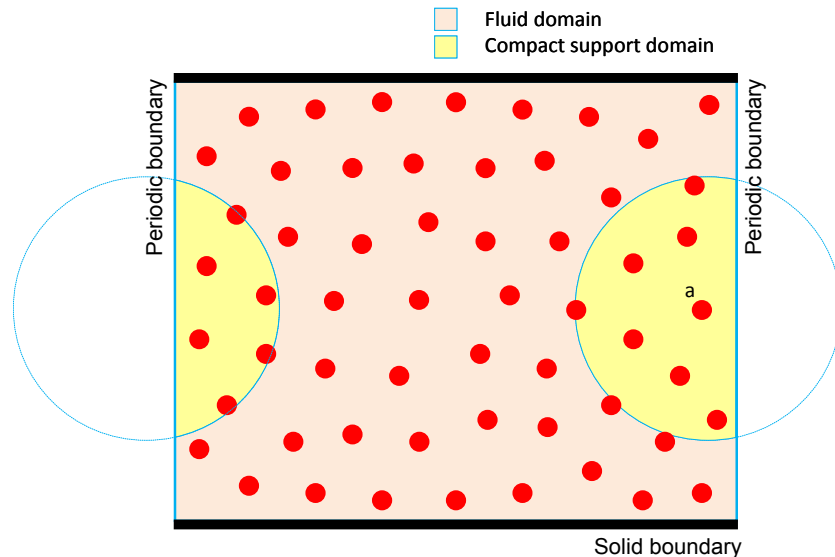
Figure 2.16. Schematic representation of the lateral periodic open boundary condition.

2.3.2 Particle initialization

In the present SPH program, a simulation can be executed from a cold start or hot start. In the cold start mode, the initial particles are uniformly distributed over the whole computational domain with particle-particle distance equal to the particle size. Solid boundaries are located at a distance of a half particle size from the nearest fluid particles. The velocity field is calculated from linear theory. Pressure and density follow the hydrostatic hypothesis and fluid is assumed to be incompressible. This initialization may produce small error due to the inconsistency with the slightly compressible assumption in the SPH simulation and the nonlinearity of the governing equations. However, the error will decay quickly.

In the hot start mode, a simulation using SPH or any numerical model, such as those based on BEM, VOF, etc, is carried in advance. The results of velocity, pressure and density that are closest to the desired initial condition are interpolated to a set of uniformly distributed particles. The hot start is more complex but it can provide more accurate initial conditions.

2.3.3   The neighbour list problem

The kernel approximation at a particle requires a search through all particles in the computational domain for a list of a small number of particles within its compact support domain. This task is repeated for every single particle; hence it costs an order of N^2 operations, where N is the number of particles inside the computational domain. If N is large, the particle searching becomes a very heavy and time consuming task, thus making the program inefficient.

Several techniques have been designed to reduce the search effort. One of the techniques is to use a search grid system in the background (see Figure 2.17). The computational domain is divided into square boxes of size $2h$, forming the search grid. As shown in Figure 2.17, only the black particles fall into the compact support domain of particle a. These particles belong

to the box containing particle a and another 8 boxes in the vicinity. Therefore, the particle search is reduced to within these 9 boxes only.

The search effort can be further reduced by minimizing the repeated search. If particle a falls into the compact support domain of particle b, then particle b will fall into the compact support domain of particle a. Hence, only one search is needed to compute the interaction between the two particles a and b. A sweep technique is used to search for the interaction of the pairs of particles. Starting from the lower left corner cell, all cells are swept once by changing their index (i, j). The interactions of particles in a cell (i, j) with particles in the East $(i, j+1)$, Northeast $(i+1, j+1)$, North $(i+1, j)$, Northwest $(i+1, j-1)$ cells and the cell itself are computed (these cells are marked yellow in Figure 2.17, cell (i, j) contains particle a). Interactions with particles in the rest of the neighbouring cells are computed in previous sweeps. This sweep technique is used in SPHysics v1.0 and is modified to take into account the interactions with ghost particles. If two particles have mutual interaction, then ghosts of one particle can also influence the other particle if they are lying inside the compact support domain. If the two particles have no interaction, then their ghosts do not influence each other.

Using the search grid and sweep techniques, the computation effort is reduced significantly from N^2 to $N\log N$.
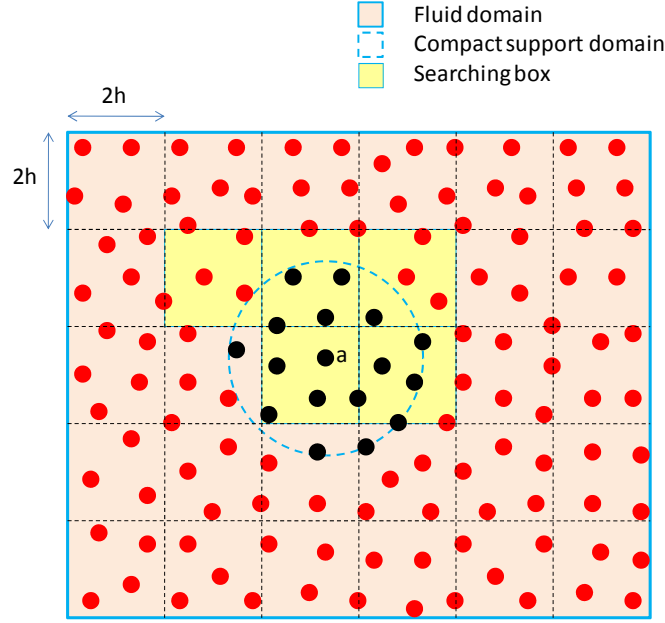
Figure 2.17. Searching boxes (yellow) for particles influencing particle a.

2.3.4 XSPH correction

In the weakly compressible SPH method, particles are free to move with their own velocity. Due to the presence of oscillation in the solutions, the neighbouring particles can have significantly different velocities which can result in particle inter-penetration. To prevent particle penetration and to regularize the velocity field, the velocity of a particle is corrected closer to the average velocity of its neighbours. This procedure is called XSPH and was introduced by Monaghan (1989). The original XSPH formulation has the form:

$$\hat{\mathbf{u}}_a = \mathbf{u}_a + \Delta \mathbf{u}_a \tag{2.84}$$

$$\Delta \mathbf{u}_a = \varepsilon \sum_b \frac{m_b}{\overline{\rho}_{ab}} \left(\mathbf{u}_b - \mathbf{u}_a \right) W_{ab} \tag{2.85}$$

where $\overline{\rho}_{ab} = (\rho_a + \rho_b)/2$ is the mean density and ε is a constant ($0 \leq \varepsilon \leq 1$).

For strict consistency, the corrected velocity is used only in the position evolution and continuity equations. The velocity before XSPH correction should be used in the momentum equation so that no dissipation is introduced by XSPH.

XSPH will introduce numerical dispersion since the movement of a particle is affected by movement of its neighbours. This numerical dispersion can be controlled by the value of ε or the kernel function. XSPH is useful for simulation of nearly incompressible fluids without using viscosity.

For two-phase flows, the original XSPH has a limitation. When a particle is very near the interface, the mean density is wrongly evaluated because of the presence of other fluid particles in its support domain. The situation becomes more severe if the two fluids have extremely large density difference, such as air and water. This wrong XSPH will distort the movement of particles near the interface and lead to wrong results.

The XSPH correction is thus modified for two-phase flows (see Colagrossi and Landrini, 2003). When correcting the velocity of a particle, only particles belonging to the same medium are used. Furthermore, the correction is also used in the divergence of velocity as

$$
\begin{aligned}
(\nabla \cdot \mathbf{u})_a &= \sum_b \frac{m_b}{\rho_b} (\hat{\mathbf{u}}_b - \hat{\mathbf{u}}_a) \cdot \nabla_a W_{ab} \\
&= \sum_b \frac{m_b}{\rho_b} (\mathbf{u}_b - \mathbf{u}_a) \cdot \nabla_a W_{ab} + \sum_b \frac{m_b}{\rho_b} (\Delta \mathbf{u}_b - \Delta \mathbf{u}_a) \cdot \nabla_a W_{ab}
\end{aligned}
\tag{2.86}
$$

The first summation in Equation (2.86) is identical to the original divergence expression of (2.45). The second summation is the correction to the divergence. The correction is often neglected in many computations; however, the use of this correction in two-phase flow improves significantly the accuracy of the solution. Furthermore, the use of XSPH is found graphically unaffected to energy conservation (Colagrossi and Landrini, 2003).

2.3.5   Density re-initialization

By using this formulation of SPH, small variations of density could be magnified by the equation of state, leading to large oscillations of pressure. The situation becomes more severe at the interface where the density oscillation is large. A filtering is applied to regularize the density field before it is used to calculate pressure. Making use of Equation (2.6), the density is reinitialized by a zero-order filter scheme as

$$\rho_a = \frac{\sum_b \rho_b W_{ab} V_b}{\sum_b W_{ab} V_b} \tag{2.87}$$

where $V_b = m_b / \rho_b$.

Note that the numerator in (2.87) is identical to that shown in (2.42). However at the boundary or the interface, where $\sum_b W_{ab} V_b < 1$, the filtering would introduce additional error. Therefore, the presence of the denominator in (2.87) is important as it normalizes the kernel approximation.

Using a similar filtering, highly nonlinear physics such as overturning of wave fronts, wave impact and vertical jet were still adequately captured by SPH (Dalrymple and Rogers, 2006)

A first-order filter scheme has been used by Belytschko et al. (1998). In this method, the density is re-initialized as:

$$\rho_a = \sum_b \rho_b W_{ab}^{MLS} V_b \tag{2.88}$$

where the moving-least-square kernel W_{ab}^{MLS} is computed using:

$$W_{ab}^{MLS} = \left[\beta_0 + \beta_1 (x_a - x_b) + \beta_2 (z_a - z_b) \right] W_{ab} \tag{2.89}$$

$$B = \begin{bmatrix} \beta_0 \\ \beta_1 \\ \beta_2 \end{bmatrix} = A_a^{-1} \begin{bmatrix} 1 \\ 0 \\ 0 \end{bmatrix} \tag{2.90}$$

$$A_a = \sum_b W_{ab} A_{ab} \tag{2.91}$$

$$A_{ab} = \begin{bmatrix} 1 & x_a - x_b & z_a - z_b \\ x_a - x_b & (x_a - x_b)^2 & (x_a - x_b)(z_a - z_b) \\ z_a - z_b & (x_a - x_b)(z_a - z_b) & (z_a - z_b)^2 \end{bmatrix} \tag{2.92}$$

The re-initialization of density is performed at every $20 - 50$ steps. This procedure restores the consistency between mass, density and volume of the particles. Moreover, a more regular pressure distribution can be obtained and the total energy is better conserved when artificial viscosity is used in the computations. These benefits have been observed in Colagrossi and Landrini (2003) both for free-surface and for interface flows. In this study, the first-order density re-initialization is used.

2.3.6 Control of interface sharpness

As discussed in Colagrossi and Landrini (2003), if Equation (2.40) is used and no surface tension introduced in the simulations of large density difference flows, lighter fluid at the interface can disperse into heavier fluid. In such cases, the state equation is modified to improve the sharpness of the interface as

$$p(\rho) = B\left[\left(\frac{\rho}{\rho_o} \right)^\gamma - 1 \right] + p_o - \bar{a}\rho^2 \tag{2.93}$$

This modified equation of state is applied to lighter fluid only, with the last term expressed in SPH approximation as

$$-\bar{a}\sum_{b}\left(\rho_a^2 + \rho_b^2\right)V_b\nabla_a W_{ab}$$

(2.94)

and is further simplified as

$$-2\bar{a}\rho_a^2\sum_{b}V_b\nabla_a W_{ab}$$

(2.95)

The value of $\bar{a}$ controls the strength of cohesion force. At the fluid interface, this equation reduces the pressure of the lighter fluid acting on the heavier fluid particles by reducing the pressure of the lighter fluid particles. This somehow represents the effect of surface tension at the fluid interface. It is used in certain cases such as very high pressure air bubbles in water. In the wave breaking problem, it is not necessary.

Note that the force should vanish (or be as small as possible) when the particle is embedded totally in its own fluid. The expression (2.95) satisfies this condition since $\sum_{b}V_b\nabla_a W_{ab} \approx 0$. In this study, the expression (2.95) is added to the SPH approximation of pressure gradient (2.40) as

$$\left(\nabla p\right)_a = \rho_a\sum_{b}m_b\left(\frac{p_a}{\rho_a\rho_b} + \frac{p_b}{\rho_a\rho_b} - 2\bar{a}\frac{\rho_a}{\rho_b}\right)\nabla_a W_{ab}$$

(2.96)

2.3.7 Time-stepping

Consider the compact form of the governing equations, which are in the form

$$\frac{d\rho_a}{dt} = D_a$$

(2.97)

$$\frac{d\mathbf{u}_a}{dt} = \mathbf{F}_a$$

(2.98)

$$\frac{d\mathbf{x}_a}{dt} = \hat{\mathbf{u}}_a \tag{2.99}$$

Two numerical time-stepping schemes of SPHysics v1.0 are used in the present SPH program: the Predictor-Corrector scheme (Monaghan, 1989) and the Verlet scheme (Verlet, 1967).

In the Predictor-Corrector scheme, the density, velocity and position of fluid particles are first predicted as

$$\rho_a^{n+1/2} = \rho_a^n + \frac{\Delta t}{2} D_a^n \tag{2.100}$$

$$\mathbf{u}_a^{n+1/2} = \mathbf{u}_a^n + \frac{\Delta t}{2} \mathbf{F}_a^n \tag{2.101}$$

$$\mathbf{x}_a^{n+1/2} = \mathbf{x}_a^n + \frac{\Delta t}{2} \hat{\mathbf{u}}_a^n \tag{2.102}$$

The pressure $p_a^{n+1/2}$ is calculated from $\rho_a^{n+1/2}$ via the equation of state. In the corrector stage, these values are corrected as

$$\rho_a^{n+1/2} = \rho_a^n + \frac{\Delta t}{2} D_a^{n+1/2} \tag{2.103}$$

$$\mathbf{u}_a^{n+1/2} = \mathbf{u}_a^n + \frac{\Delta t}{2} \mathbf{F}_a^{n+1/2} \tag{2.104}$$

$$\mathbf{x}_a^{n+1/2} = \mathbf{x}_a^n + \frac{\Delta t}{2} \hat{\mathbf{u}}_a^{n+1/2} \tag{2.105}$$

Finally, the density, velocity and position of fluid particles at time step $n+1$ are updated

$$\rho_a^{n+1} = 2\rho_a^{n+1/2} - \rho_a^n \tag{2.106}$$

$$\mathbf{u}_a^{n+1} = 2\mathbf{u}_a^{n+1/2} - \mathbf{u}_a^n \tag{2.107}$$

$$\mathbf{x}_a^{n+1} = 2\mathbf{x}_a^{n+1/2} - \mathbf{x}_a^n \tag{2.108}$$

The pressure p_a^{n+1} is calculated from ρ_a^{n+1} via the equation of state

In the Verlet scheme, the properties of fluid particles are updated as

$$\rho_a^{n+1} = \rho_a^{n-1} + 2\Delta t D_a^n \tag{2.109}$$

$$\mathbf{u}_a^{n+1} = \mathbf{u}_a^{n-1} + 2\Delta t \mathbf{F}_a^n \tag{2.110}$$

These calculations of density and velocity use second order approximation which involves the information of particles at time step $n-1$. After every M steps (M is in order of 40), a first order scheme is used:

$$\rho_a^{n+1} = \rho_a^n + \Delta t D_a^n \tag{2.111}$$

$$\mathbf{u}_a^{n+1} = \mathbf{u}_a^n + \Delta t \mathbf{F}_a^n \tag{2.112}$$

The use of 1st order forward scheme is to remove the spurious oscillation due to the effect of the 2nd order central difference scheme.

The position of fluid particles is updated at every step as:

$$\mathbf{x}_a^{n+1} = \mathbf{x}_a^n + \Delta t \hat{\mathbf{u}}_a^n + 0.5\Delta t^2 \mathbf{F}_a^n \tag{2.113}$$

The pressure p_a^{n+1} is calculated from ρ_a^{n+1} via the equation of state.

In both the above schemes, the time-step size is controlled by the Courant–Friedrichs–Lewy (CFL) condition. The CFL condition requires the distance that a fluid particle moves in one time step to be less than a smoothing length. This condition reads

$$\Delta t_{CFL} = \frac{h}{u_{max}} \; ; \; u_{max} = \max_a \left(c_s + \max_b \left| \frac{h\mathbf{u}_{ab}\mathbf{x}_{ab}}{\mathbf{x}_{ab}^2} \right| \right) \tag{2.114}$$

The forcing condition requires that the movement of a fluid particle due to the acceleration (second order term) to be less than a smoothing length. This implies that

$$\Delta t_F = \min_a \sqrt{\frac{h}{\mathbf{F}_a}} \tag{2.115}$$

The time-step may be updated at every step using

$$\Delta t = 0.2 \min\left(\Delta t_{CFL}, \Delta t_F \right) \tag{2.116}$$

In the present SPH program, the initial time-step is calculated by a simpler formulation

$$\Delta t = \frac{0.2h}{\max_a (c_s)} \tag{2.117}$$

2.3.8   Computation flow chart
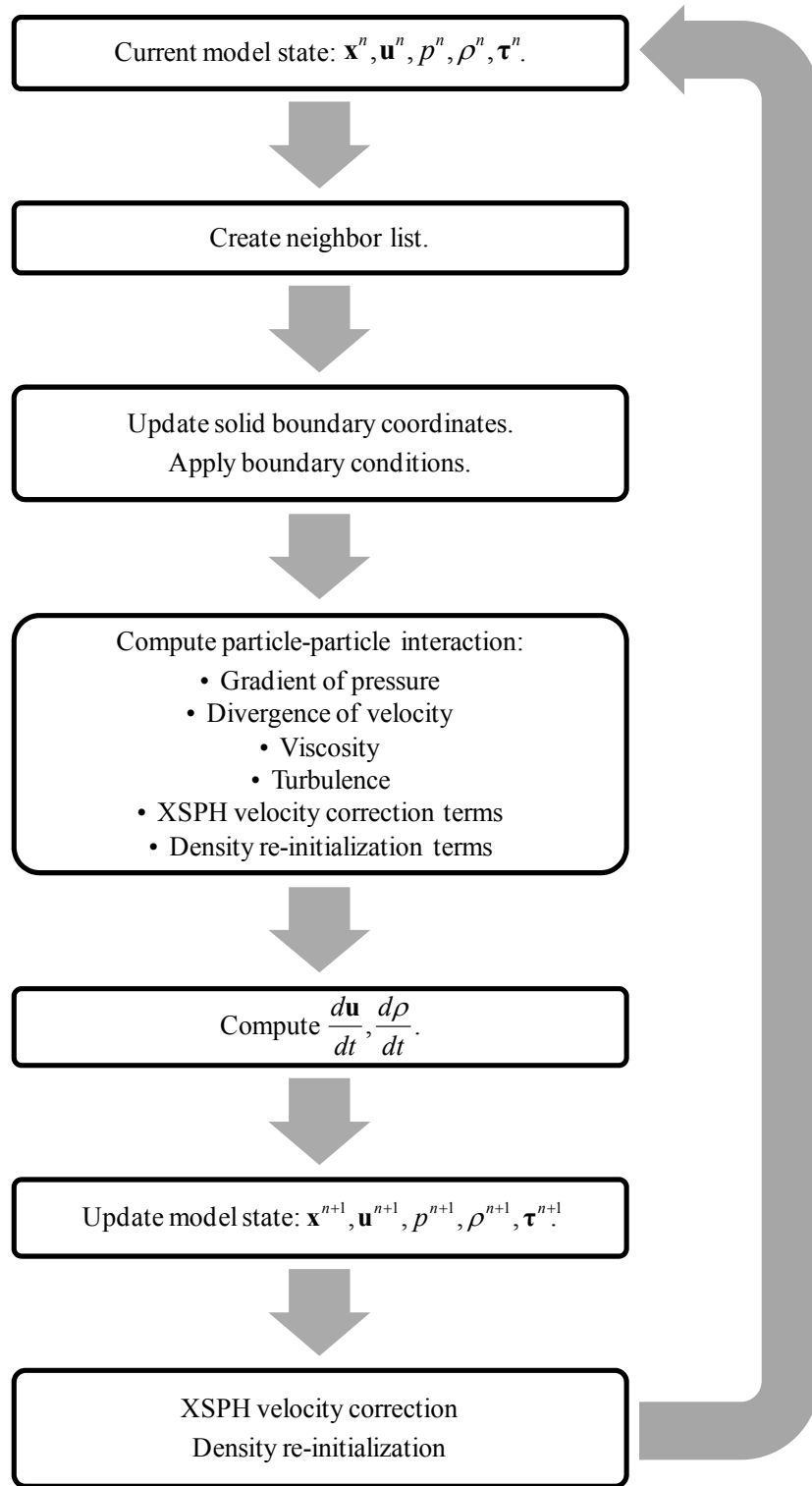
Figure 2.18. Computation flow chart of the SPH program

2.4 Generation of a plunging wave in deep water

2.4.1 Wave simulation

Using a moving vertical paddle in the numerical wave tank, a desired wave can be generated by imposing required movement patterns to the paddle. The desired movement of the paddle can be computed by using linear or nonlinear theories for wave generation by piston paddles which can be found in the book of Dean and Dalrymple (1984). However these calculations are analytical and are derived from some simplified equations with assumptions such as linearity. Therefore, when the derived paddle movement is applied in numerical models, the generated wave usually exhibits higher nonlinearity (due to nonlinearity in the numerical model) and in many cases they are significantly different from the analytical solutions.

In this study, the paddle movement is derived directly from the paddle movement signals used in the laboratory experiment. Using the paddle signals derived directly from experiments and direct simulations of the wave paddle, wave generations in experiments can be mimicked and the wave conditions in laboratory experiments are reproduced very well in the numerical simulations.

2.4.2 Generation of breaking wave

The initiation of wave breaking by focusing of wave energy in space and time has been tried out in the past. Wave energy of unidirectional waves can be focused by laterally converging the channel walls or focusing in the wave propagation direction by frequency dispersion. Experiments by Kway (2000) used the longitudinal frequency dispersion and superposition of the wave components in time and space. This method has been used in several studies in the past including Chan and Melville (1988). In this method, a modulated wave packet is generated by summing up sinusoidal wave components of discrete frequencies. Using linear wave theory and dispersion relationship, wave number and phase can be calculated such that all the

wave crests appear simultaneously at a desired point in space and time. Constructive interference of the wave component leads to a build up of water level and increase of speed of water at the crest. The intensity of the breaking wave can be controlled by changing the amplitude of each wave component. This breaking wave can be generated in water of constant depth.

Such an approach has been used in the experimental studies by Kway (2000) and Lim (2001). An amplitude and frequency modulated voltage signal is sent to the wave paddle control system in the laboratory. The signal comprises of 28 components whose frequencies are in the range of 0.56 Hz to 1.1 Hz. The phases and amplitudes of the components are calculated such that the generated wave packet will break at a distance of 15.2 m from the paddle mean position and after 26 seconds. The input voltage signal used in the experiment is given in Figure 2.19.
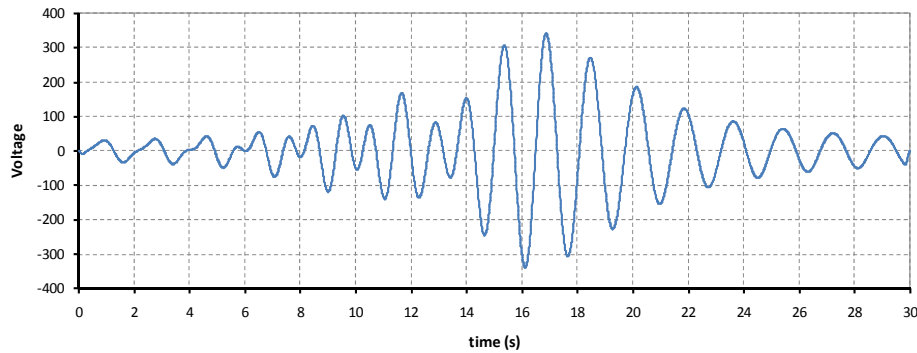
Figure 2.19. Voltage signal input to the wave paddle control system in the experiment.

The velocity of the paddle is needed as the input for the SPH program. In order to obtain the velocity of the paddle, it is assumed that the voltage varies linearly with stroke of the paddle (Lim, 2001). Equating the maximum voltage to half of the maximum stroke the following equation is assumed and used to obtain the velocity.

$$V(t) = Stroke_{max} \times \frac{Voltage(t) - Voltage(t-1)}{2 \times Voltage_{max} \times dt} \tag{2.118}$$

69

Using this relationship, the velocity of the wave paddle is derived from the voltage signal and is shown in Figure 2.20. This velocity signal was used in a numerical simulation of breaking wave in Lim (2001) and will be used in this thesis.
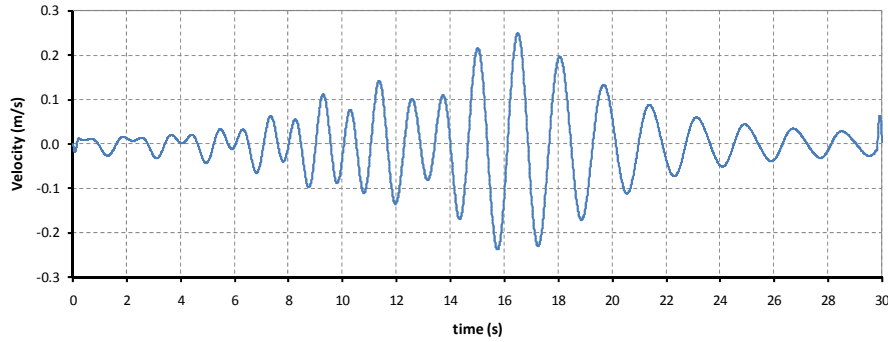
Figure 2.20. Velocity of the paddle input into the numerical simulation.

2.5   Code parallelization

When high resolution simulation is required and the air-water phases need to be simultaneously simulated, the number of particles involved in the simulation, *N,* becomes extremely large.

In theory, a computation at a single particle requires a loop over all particles in a computation domain to compute the interaction between the particle itself and its neighbours. Thus the computation in one step is O(N^2). However, using an advance searching technique (see section 2.3.3), the computation complexity is reduced to almost O(N).

Since the computation is explicitly and totally Lagrangian, the computational time step nearly varies linearly with the resolution (proportional to particle size). If *M* is the times of resolution increase, then the number of particles will increase by M^2 times in 2D and M^3 in 3D. Time stepping is assumed being reduced by *M* times when resolution increase by *M* times. That means number of time steps will increase by *M* times. Thus, in total, computational time

increases M^3 times in 2D and M^4 times in 3D. The actual test of parallel computation has shown that the computational time increment is closed to the theoretical $O(M^3)$.

In such situation, parallel computation is obviously essential. The computational domain is partitioned into sub-domains and the Message Passing Interface (MPI) is used to exchange data among the sub-domains. The domain decomposition and data exchange are described as followings.

Firstly, the original computational domain is decomposed into several sub-domains; each is handled by a separate processor. Assuming the original domain is divided into 6 sub-domains (shown as colour coded boxes in Figure 2.21a). A sub-domain is required to exchange data with its adjacent sub-domains, e.g. domain #4 exchanges data with domains #0, 1, 2, 3, 5.

To serve for the data exchange, small zones at the interface between sub-domains are created. These zones are called buffer zones and will have widths of $2h$ (which is equal to the smoothing length or the radius of the compact support circle). A copy of particles which lie inside a buffer zone just next to a sub-domain (sharing the same edge or corner) is sent to that sub-domain. Copies of particles sent to a sub-domain will be added into its particle list, creating an extended sub-domain (as shown in Figure 2.21b). Small colour coded boxes surrounding the sub-domain #4 are received from adjacent sub-domains with the same colour codes.

Once all the sub-domains sent and received necessary data, normal SPH calculation is performed for all particles in each extended sub-domain in a separate processor (Figure 2.21c). However, only particles in the original sub-domain need to be updated with new properties.

The efficiency of the parallel computing could be maximized by balancing the computational load and communication (data exchange) load. Preliminary calculations and benchmark simulations are performed to estimate the resource needed for the simulation.
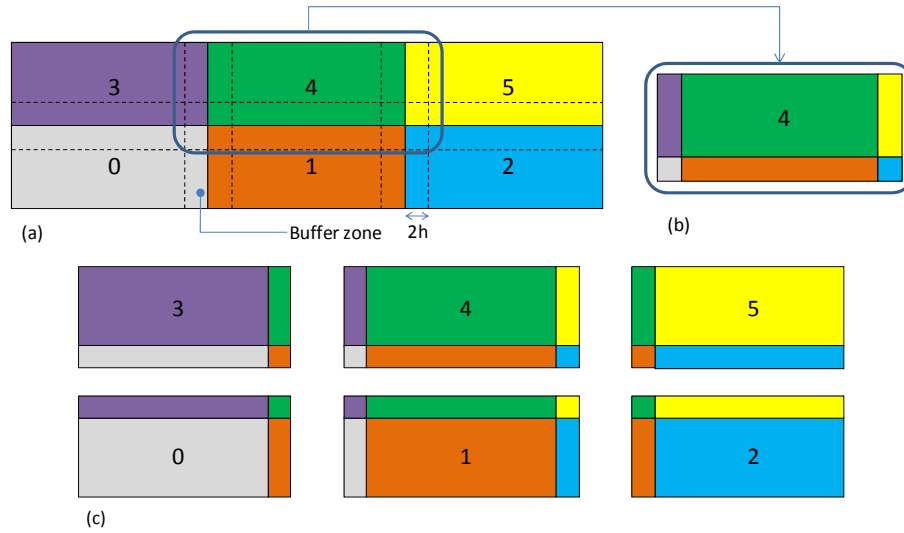
Figure 2.21. Domain decomposition and buffer zones for data exchange.

At the final nested stage, the SPH program is used to simulate a breaking wave starting from the instance of wave steepening to that of the wave collapse. The time scale for this process is around 1 second. The length scale of the simulation is equal to that of a laboratory experiment done. Computation domain in two-dimensional is 8 m long and 3 m high. The desired resolution of the simulation is 0.001 m or less. Thus, the simulation will involve 24 million particles. Computational time step required for the simulation at this resolution is 10^{-6} s. Thus, the number of steps is 1 million.

Preliminary computations in single PC and parallel cluster have shown that the number of particles should be less than 200,000 – 300,000 in order to finish the computation in a practical time (about 2 weeks). Thus, the number of processors needed is 70 – 100.

In parallel computation, additional time for data exchange is required. The communication time among processors is large if the data required for exchange is large. This communication time sometimes dominates the pure computation time. Thus we expect the speedup of a small

problem and a large problem could be significantly different even the same program is used. Therefore, in this test, a reasonably large problem is used. The size of the problem is as below

- Number of particles: 3,673,200

- Number of step: 1,000

The test is done on 25, 50, 75, 90 processors in a CE Linux cluster with the following specification:

- Nodes: 23, with 4 processors/node.

- Processor: Intel(R) Core(TM) i7 CPU   940 @ 2.93GHz

- Memory (RAM): 12GB

- Network card: Myri-10G PCIe NIC with MX

The number of processors used and average number of particles per processor, time to finish 1000 steps and speedup ratio are shown in the Table 2.1. Since the program is too large to run in a single processor, the 25-processor run will serve as benchmarking point with speedup ratio equal 1.

The speedup curve of the program is plotted (blue dots) against the ideal one (red dots) in Figure 2.22. The green solid line is the fitting curve to the actual speedup. The 100-processor run is not shown because hyper-thread mode is used. The speedup in running the SPH program is close to expectations.

Table 2.1. Computation time and speedup ratio versus number of processors

No. of proc	Particles/1 proc	Comp. time/ 1000 steps (min)	Speedup
25	147,000	13.065	1
50	73,000	6.495	2.01
75	49,000	4.71	2.77
90	41,000	4.178	3.13
100♣	37000	6.278	NA

♣Hyper-thread mode used as the number of physical processors is 92. This hyper-thread mode reduces the computation speed probably because some physical processors have to carry 2 jobs, and this slows down the whole computation.
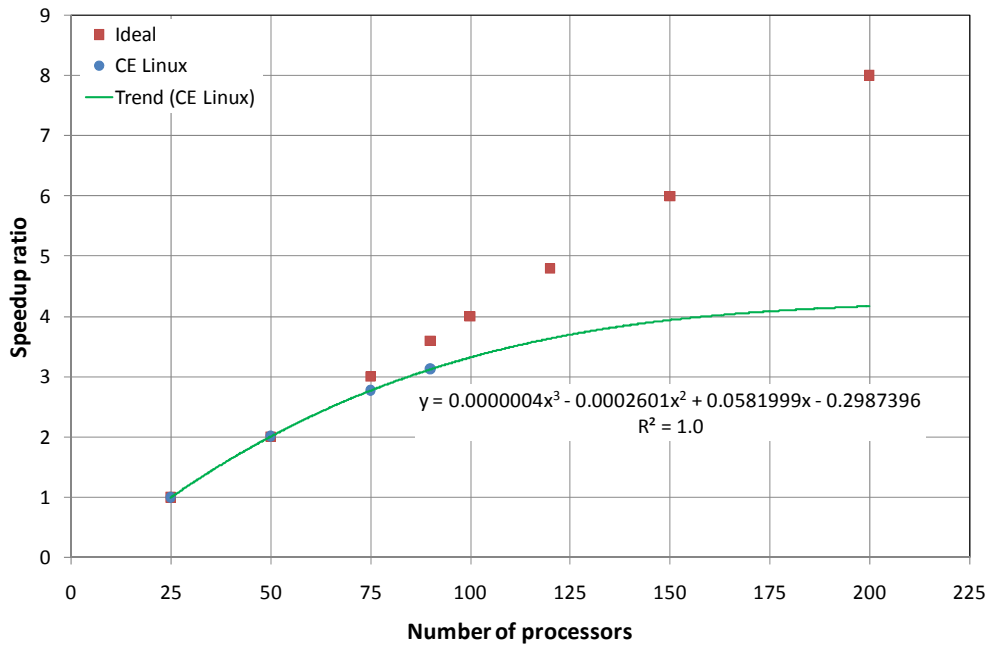
Figure 2.22. Speedup curve of the SPH program running in the "CE Linux" cluster.

Using this test and assuming that the computation time increases at $O(M^3)$ with M is the increase ratio of resolution; apply to the target problem (24 millions particles), computation time will increase $(24/3.7)^{3/2} = 16.5$ times.

Number of particles in one processor is assumped to be in between 40,000 – 300,000 to retain the speedup of the tested problem (or linearly scale up of the tested problem). The number of processors required is 160 – 580. Using this assumption, number of processors, number of particles and the computation time (minutes per 1000 model steps and hours per 1 model second) for the target problem are estimated as in Table 2.2.

Table 2.2. Estimated computation time versus number of processors for the target problem

No. of proc	Particles/ 1 proc	Comp. time/ 1000 step (min)	Comp. time/ 1 model sec (hr)
90	267,000	23.517	391.95
162	148,000	13.065	217.75
325	68,000	6.495	108.25
487	49,000	4.71	78.5
585	41,000	4.1775	69.625

To verify this estimation, a simulation of 22,950,000 particles, time step of 10^{-6} s (close to the target problem) is performed on 90 processors. The computation time for 1000 model steps is 22.8 mins, and time to complete 1 model second is 380 hr. These values are very close to the estimation above for 24 millions particles on 90 processors shown in the table above. Thus within the range of 40,000 – 300,000 particles per processor, the computational time of the program can be linearly scaled with the size of the problem.

2.6 Multi-scale nesting approach

As shown in the previous section, even with parallel computation with large number of processors, the numerical simulation is unable to perform the whole process of two-dimensional two-phase wave focusing and breaking at our target resolution. There are several techniques to address this issue. Non-uniform particle size and nesting are the two techniques that have been used intensively for multi-scale problems. In this study, the nesting approach is used. The computation domain is nested down to the area of interest from a much coarser simulation (see Figure 2.23). The nesting procedure is implemented through the following two steps.

In the first step, the wave packet generation and propagation in a long water flume (shown in Figure 2.2 and Figure 2.23) is simulated at a coarse resolution. This simulation is performed until the wave packet focuses and starts to break. It is well understood that during this stage the evolution of the waves are not much affected by the air, thus single-phase flow model is sufficient. Various numerical models could perform well during this stage. However, due to the fact that the waves are short waves and travel a long distance before focusing, numerical dissipation is a crucial issue. Among available numerical methods, the boundary integral method (BIM) and the current SPH are good candidates. In this study we use SPH for simulation of wave propagation and focusing. Results show that SPH output agrees very well with that of BIM and observation in the experiment. The numerical dissipation is under control and reduced significantly.
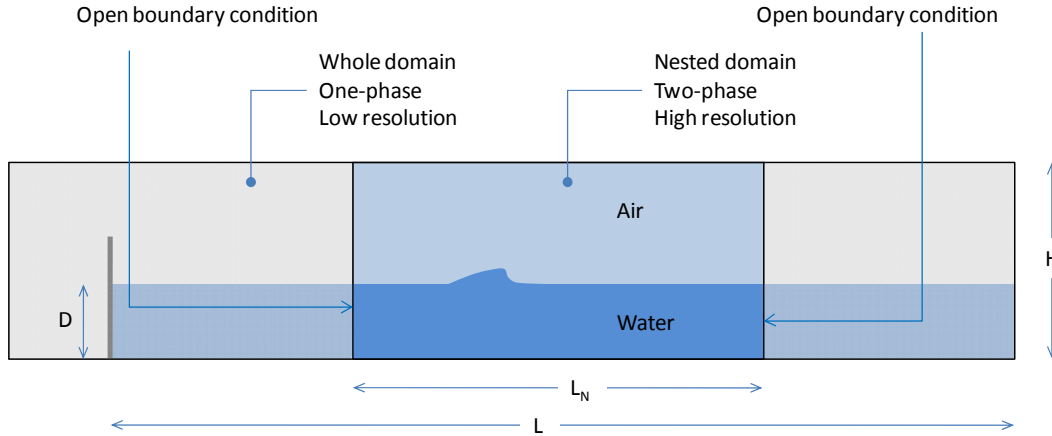
Figure 2.23. Schematic plot of the nesting procedure.

In the second step, a smaller domain that covers the breaking area is extracted from the coarser simulation in the first step. The domain is chosen such that it is large enough to minimize inconsistency errors at the nesting boundary to propagate in and influence on the breaking process. Much finer resolution is used for the simulation of this domain. Initial condition of the water is interpolated from the coarser simulation. The area above the water surface is also filled up by a layer of air. Initial gauge pressure and velocity of the air layer are set to zero. Air velocity near the interface with water is extrapolated from the velocity of the water to reduce the inconsistency.

In this thesis, the following two nesting techniques are implemented.

2.6.1 Interpolated nesting boundary condition

A key step in nesting is the exchange of boundary and field information between two computational domains of two different resolutions. The finer resolution domain is located within the coarser resolution domain. The information exchange could be one-way (one-way nesting) or two-way (two-way nesting). In the one-way nesting, the finer resolution domain utilizes data from coarser resolution domain to carry out simulation and there is no data to be fed

back to the coarser domain. In the two-way nesting, the finer resolution domain receives data from coarser resolution domain to carry out simulation, and the information from finer resolution simulation, which is supposed to be more accurate, is fed back to the coarser domain to correct its current state. In general, several nest levels could be used to go from larger scale simulation to the finest scale. In this thesis, the one level and one-way nesting are used.

The scheme for the one level and one-way nesting is shown in Figure 2.24. In this scheme, the coarser resolution (represented by light blue area and blue circles as particles) simulation is carried out in advance. The simulation of the finer resolution domain (represented by light pink area and red circle as particles) is carried out by using information from the coarser domain. Lateral boundaries of the finer domain are defined by lines connecting all the outer most particles on the left and right sides of its domain. The initial condition of the finer domain is interpolated from the coarser domain. Lateral boundary condition is transferred from coarser to finer domain through buffer zones, which are defined as strips of $2h$ wide along the lateral boundaries of the finer domain. During every step of the simulation of the finer domain, properties of the red particles within the buffer zones are interpolated from the results of coarser domain. Properties of particles at the inner zone are computed as usual using SPH approximation. In the next step, velocity and position of particles in the finer domain are calculated from equations and lateral boundaries are defined again.
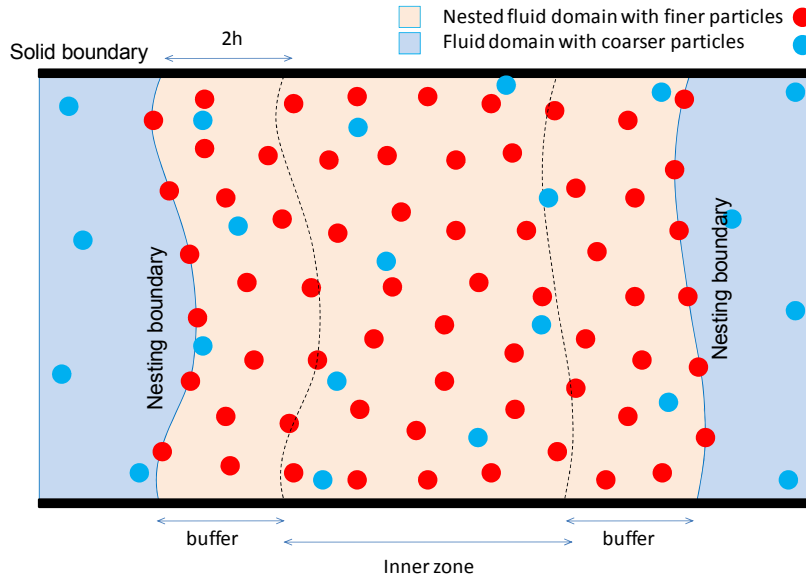
Figure 2.24. Schematic representation of the interpolated boundary condition.

2.6.2 Periodic boundary condition

The nesting procedure could be further simplified by making use of known characteristics of the problems. The wave focusing problem involves slow dynamics at large scale. The length and time scales are much larger than those of the breaking problem. In this study, the wave flume is 36 m long. The focus point and time of the wave packet to focus are 15 m and 26 s, respectively. The wave length at the focus point is around 7 m and the maximum velocity of particles is 0.4 m/s. The dynamics of the breaking process is much faster and more localized. The length scale of the breaking area is around 2 m and the time scale of breaking process is 1 – 2 s. The breaking wave crest is located at the centre of the domain or 3 m from the left boundary. The velocity of water particle during the breaking could reach 2 -3 m/s. Therefore, within one second, disturbances at the lateral boundary which is sufficiently far away are not expected to reach the breaking area. Making use of these characteristics of the wave focusing and breaking problem, the lateral periodic boundary condition (see Section 2.3.1.3) could be used. The procedure is as followings:

- The length of the nested domain is chosen to be at least one wave length around the focus point so that the breaking area is in the middle of the domain. The left and right boundaries are preferred to be at the places where particle velocity is lowest.

- Water particles at a desired resolution are regularly distributed in the nested domain from the bottom to the free surface. Air particles are regularly filled up on top of the water surface. A solid boundary located at the top of the air layer to prevent the air leaking at the top. The thickness of the air layer is 3 – 4 times of the water layer to minimize the effects of the imposed solid wall at the top.

- The initial condition of the water particles in the nested domain is interpolated from the coarser simulation at the starting time of the nested simulation. Initial condition comprises of pressure, density, velocity and other viscosity, turbulence and correction terms of the particles. Parameters of the state equation for water are copied from coarser simulation. Initial pressure and velocity of the air layer are set to zero. Air velocity near the water interface is extrapolated from the velocity of the water to reduce the inconsistency.

- Lateral periodic boundary conditions are applied at the two end of the nested domain, for both water and air phases.

2.6.3 Comparison of the two nesting techniques

A study of the sensitivity and comparison of the two nesting techniques described above for nested simulations at different particle sizes (0.005, 0.0025 and 0.001 m) were conducted (see Figure 2.25 to Figure 2.30). In these simulations, only one-phase flow is considered. Results in Figure 2.25 and Figure 2.26 show that at coarser resolution, dx = 0.005 m, the shapes of the breaking wave are significantly different. At finer resolution, dx = 0.0025 m, the both types of boundary condition produce much similar results at the breaking area, except for slightly difference at the vertical jet (see Figure 2.27 and Figure 2.28). It suggests that at

80

coarser resolution, numerical noise due to the non-natural truncation of the lateral boundary and the imperfect boundary condition at lateral boundaries propagate faster and reach the centre of the domain in a shorter time. The numerical noise is larger and propagates faster when the resolution is lower, similar to other gridded methods. The SPH method uses information from neighbour particles to approximate properties of a particle, thus the more particles used in its neighbour, the more disturbances it has to receive. In other words, the disturbance is propagating at a speed proportionally to the number of neighbour particles and the radius of the support domain in that direction. At the finest resolution of 0.001 m, the two types of boundary condition produce very similar result at the breaking region (see Figure 2.29 and Figure 2.30).
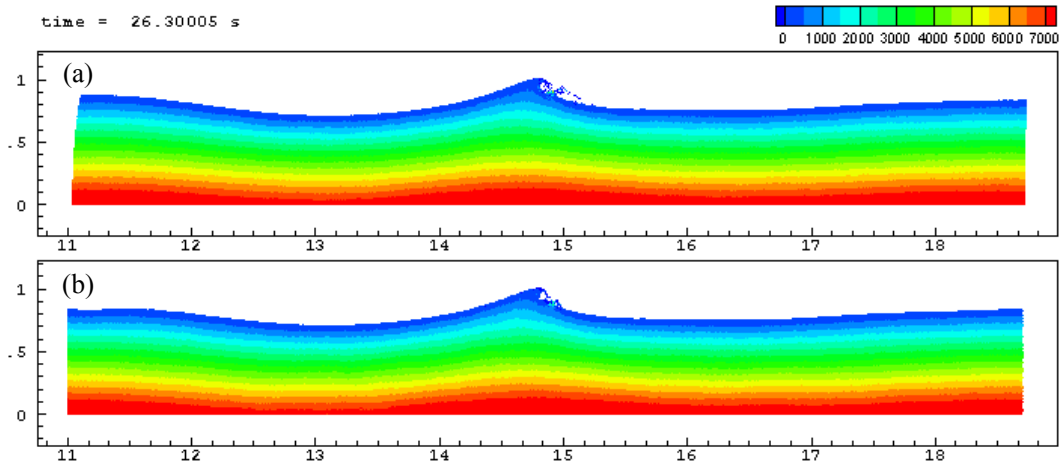
Figure 2.25. Results at 26.3 s (0.5 s since focal time) from interpolation at the boundaries (a) and periodic boundary condition (b). Particle size 0.005 m. Color is fluid pressure.
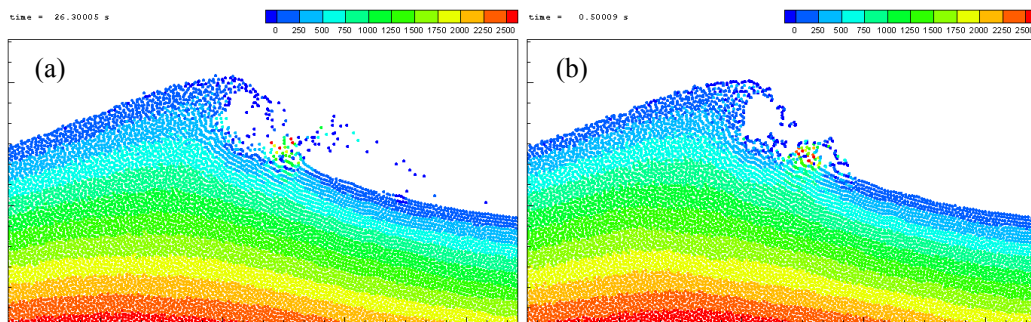
Figure 2.26. Results at 26.3 s (0.5 s since focal time) from interpolation at the boundaries (a) and periodic boundary condition (b), zoomed in at the breaking area. Particle size 0.005 m. Color is fluid pressure.
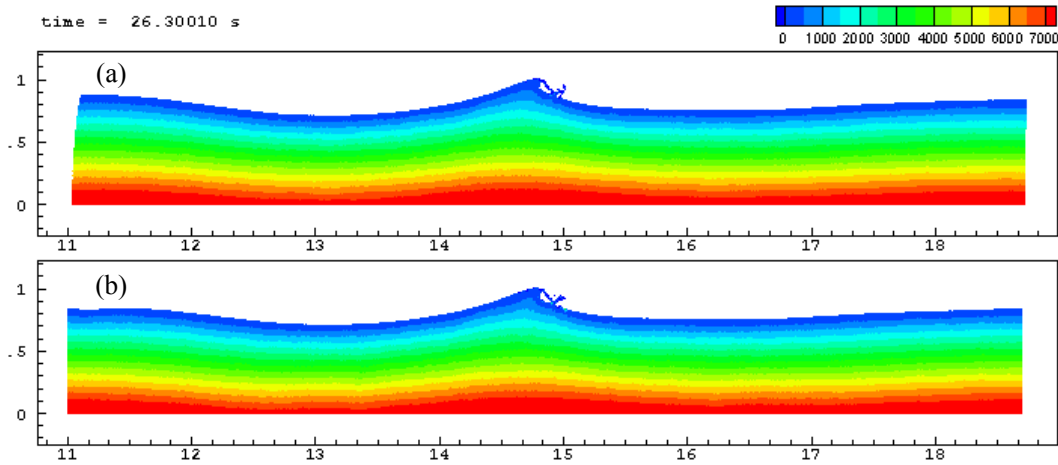
Figure 2.27. Results at 26.3 s (0.5 s since focal time) from interpolation at the boundaries (a) and periodic boundary condition (b), zoomed in at the breaking area. Particle size 0.0025 m. Color is fluid pressure.
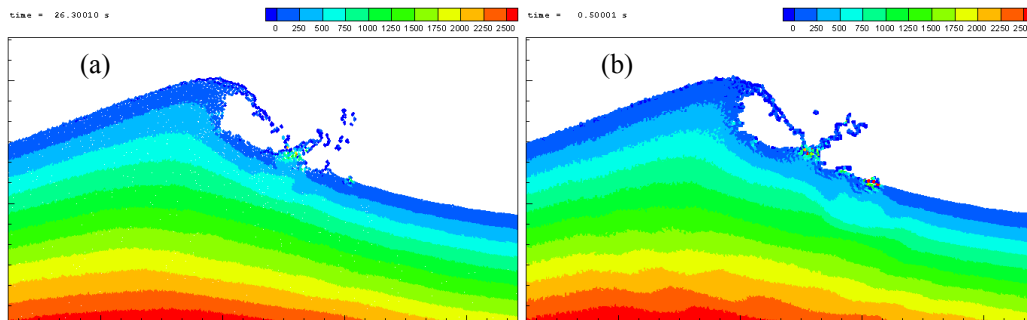
Figure 2.28. Results at 26.3 s (0.5 s since focal time) from interpolation at the boundaries (a) and periodic boundary condition (b), zoomed in at the breaking area. Particle size 0.0025 m. Color is fluid pressure.
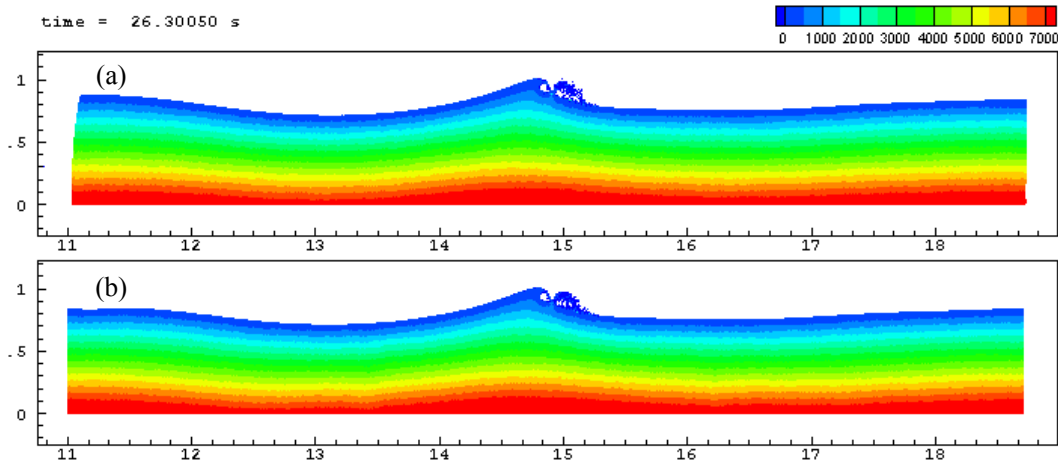
Figure 2.29. Results at 26.3 s (0.5 s since focal time) from interpolation at the boundaries (a) and periodic boundary condition (b), zoomed in at the breaking area. Particle size 0.001 m. Color is fluid pressure.
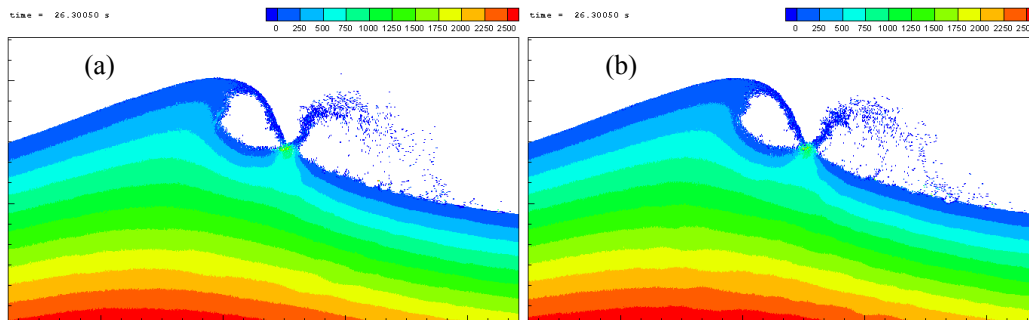
Figure 2.30. Results at 26.3 s (0.5 s since focal time) from interpolation at the boundaries (a) and periodic boundary condition (b), zoomed in at the breaking area. Particle size 0.001 m. Color is fluid pressure.

From the theoretical point of view, the interpolated nesting boundary condition is more consistent and accurate than the periodic boundary condition technique in term of the transferring the dynamics of the particles in the coarser domain is into the finer domain. However, the interpolated nesting boundary condition technique in more complicated when applied to the air-water two-phase flow problems. In such problems, the movement of the air particles is faster and more turbulent compared to that of water. This makes the definition of lateral boundaries and buffer zones more difficult, especially near the air-water interfaces. Moreover, in order to supply boundary condition for the nested domain with two-phase flow, the coarser simulation must be two-phase as well. The two-phase flow simulation even at the coarser resolution will involve much more particles (number of air particles is usually twice or triple number of water particles) and thus reduces the efficiency of the nesting approach.

The periodic boundary condition technique is relatively simpler. Using this technique, the lateral boundaries are fixed and no buffer zone is required. The air particles could be initiated from rest at the start of the finer simulation. Therefore two-phase simulation at coarser resolution is not required. However, inconsistencies at the lateral boundaries could propagate far inside the computational domain if the resolution is relatively coarse and simulation is long. In the problem of wave breaking studies in this thesis, the time scale of the breaking process under consideration is very short and the resolution is very fine. Under these conditions, as concluded in the above sensitivity study, the two nesting methods will produce very similar results at the breaking region. Therefore, in the study of wave breaking in this thesis, the periodic boundary condition is used.

Chapter 3.   Validation of SPH Program in Simulating Extreme Wave Breaking

The SPH program is validated against common benchmark problems ranging from slow to fast dynamics. The chosen benchmark problems include sloshing in an enclosed tank, dynamics of a high pressure air bubble rising in water, dam break with impact on a vertical wall, and wave propagation in a flume. The SPH results are compared with analytical, numerical solutions, and experiments. Sensitivity studies on key numerical settings of SPH are also presented.

3.1   Sloshing Tank

The configuration of the sloshing problem and initial surface displacement are given in Figure 3.1. The tank is 1.0 m long and 0.25 m high. The still water depth in the tank is $H = 0.2$ m. The water is initially inclined a slope of $S = 0.02$ ($Z_0 = 0.01$ m). The water sloshes under gravity with one slosh cycle period estimated from linear theory, $T = 1.5196$ s. Results are verified against the linear analytical solution given in Lin and Li (2002).

The SPH simulation uses a set of 50,000 water particles with the size of $0.01H$ in diameter. The simulation is carried out for 10s, which covers 6 sloshing cycles. Only the single-phase flow simulation is presented.

The initial free surface and pressure field of the sloshing problem are shown in Figure 3.2. The initial analytical solution of free surface is also plotted in this figure as the black line.

Comparisons of the simulate sloshing free surfaces to the analytical solutions at different time instances are given in Figure 3.3.
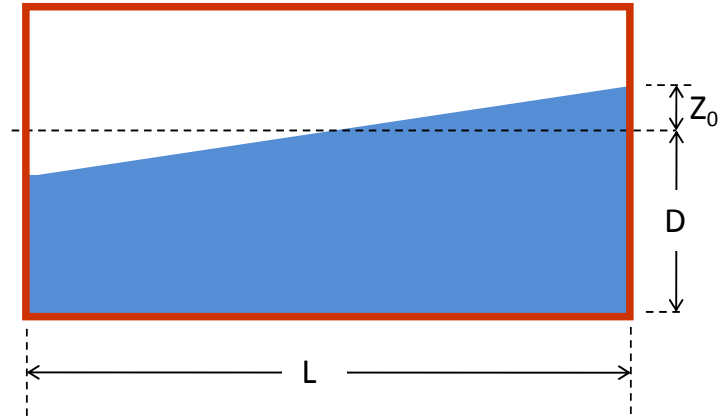
Figure 3.1. Schematic configuration of the sloshing water tank problem.
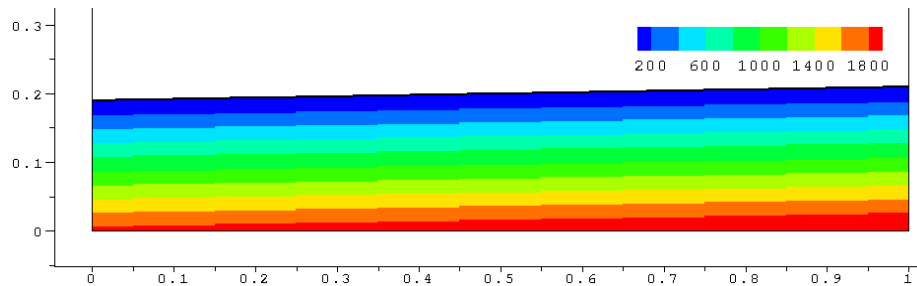
Figure 3.2. Initial surface elevation and pressure field.
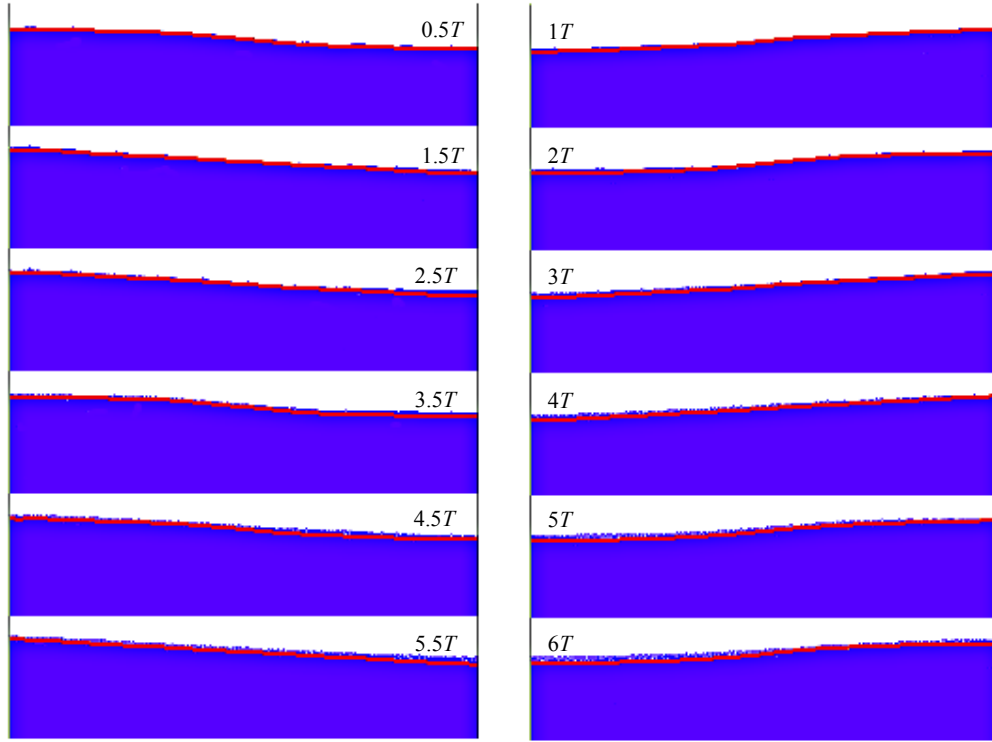
Figure 3.3. Comparison of simulated (blue) to analytical solution (red line) of free surfaces.

Figure 3.4 plots graphs of the normalized potential, kinetic and total energy which are defined as

$$E_P = \frac{E_P - E_{T0}}{\Delta E} + 1; \ E_K = \frac{E_K}{\Delta E}; \ E_T = \frac{E_T - E_{T0}}{\Delta E}$$

where E_T is total energy, E_{T0} is initial total energy; E_P and E_K are potential and kinetic energies, respectively; ΔE is the value used for normalizing; here $\Delta E = E_{Kmax} - E_{Kmin}$.

It can be seen from the figure that the kinetic and potential energies are transforming to each other. The magnitudes of kinetic and potential energy oscillations reduce by 10% after 6 cycles. The total energy increases by 20% of the maximum range of the kinetic energy ΔE.
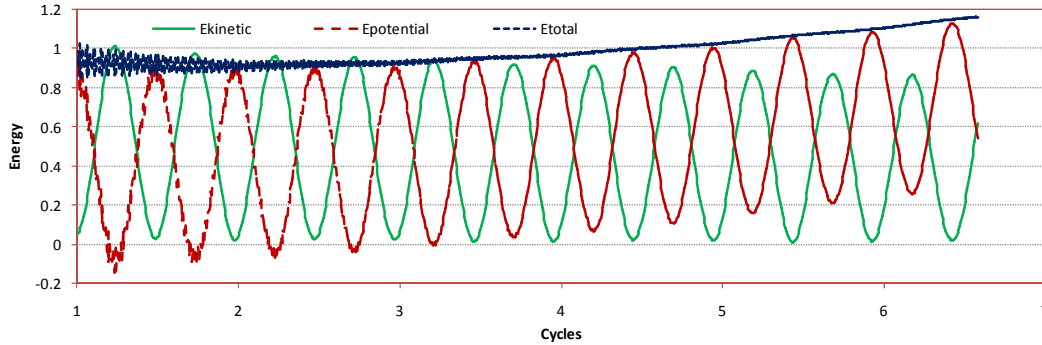
Figure 3.4. Energy plot of single-phase simulation of sloshing problem.

The energy lost could be explained, similarly to that of other numerical methods, by the numerical (and artificial) and physical viscosity presented in the SPH simulation. The artificial and physical viscosity term is introduced to approximate the real fluid viscosity and to stabilize the SPH solution if required. The numerical viscosity is the result of the approximation error of the pressure gradient and other terms. For example, without the presence of other forces, the pressure gradient inside a fluid in a water tank must balance with the gravitational acceleration. However, the ratio of SPH approximation of pressure gradient over gravitational acceleration may not exactly equal to unity. The difference is dependent on many numerical parameters such as the kernel characteristics, the particle arrangement or the initialization of particle properties. If this ratio is less than one, the error has analogous effect to viscosity to dissipate energy. But if the ratio is greater than one, more energy is added to the system. In Figure 3.4, the tendency of total energy increase is observed while oscillations of individual energy components reduce. The reduction of energy oscillations is normally due to viscosity. The energy lost is 10% after 6 sloshing cycles. The increase of total energy is probably due the increase of the mean potential energy. This is the result of the slight increase of the free surface level due to the error in the approximation of the pressure gradient, especially at the free surface. After investigation, we found that the imperfect initialization of particle pressure and density, the lacking of particles in supporting domains near the free surface are the major

90

causes of this error. Nevertheless, this error may have significant effect to the problems with very small disturbance and inviscid flow. In the problems involving strong flow motion of real fluids, viscous effect could overwhelm this error. A balance could be found by carefully tuning numerical parameters. This will be demonstrated in the sensitivity studies later in this chapter.

3.2   Rising of an air bubble in water

The configuration of the air bubble rising problem is given in Figure 3.5. The water tank has dimensions of $L = 6R$ and $D = 10R$. The bubble is initially at high pressure and released near the bottom of the tank. The bubble has circular shape of diameter $d = 2R$. The center of the bubble locates at the center line of the tank and $2R$ from the tank's bottom. The ratio of the reference density of air and water is 1.2/997. Due to the difference of pressure inside and outside of the bubble and buoyancy, the bubble quickly deforms and rises up.
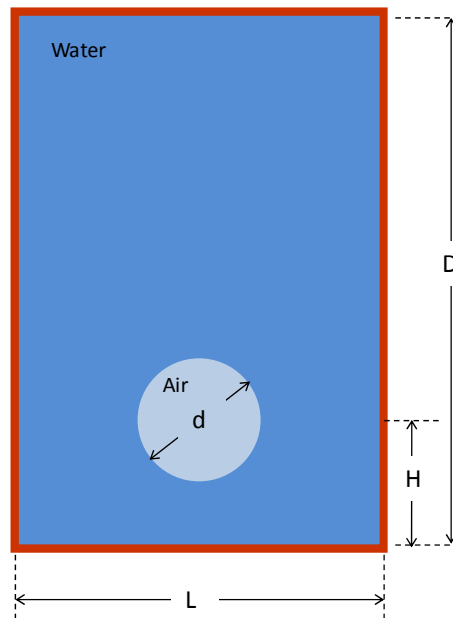
Figure 3.5. Setup and dimension of a high pressure air bubble rise in water.

The SPH simulation involves 37,500 particles, in which 35,524 is the number of water particles. The particle diameter is $0.04R$. Parameters for SPH simulation are: smoothing length $h = 0.08R$; numerical sound speeds in water $cs_W = 28.28(gR)^{0.5}$, and in air $cs_A = 400(gR)^{0.5}$; time step $dt = 10^{-5}$.

Due to its very high pressure, the air particles near the bubble surface can easily break through the interface and go inside the water. Therefore, the sharpness control parameter is turned on to prevent the air particles at the interface diffusing quickly into the water. The sharpness control parameter used in the simulation is $a = 15,000$.

Snapshots of vertical velocity of the surrounding water at some time instances are plotted in Figure 3.6. The bubble's shapes are shown in Figure 3.7 together with the solution of the bubble surface solved by LS method in Sussman et al. (1994). Note that the LS solution is for reference only, not for evaluating the accuracy of SPH or LS model.

At early stage, an upwelling water jet is created beneath the bubble. The jet deforms the bubble to a horse-shoe shape. The jet becomes broaden and the horse-shoe shape bubble stretched horizontally. The necks at the bubble tips become thinner and the bubble tips have rolling motion due to the circulation of the surrounding water. Eventually, bubble tips detached forming smaller bubbles. The main bubble is flattened and rises up.

As shown in Figure 3.7, the shapes of the bubble derived from the two methods agree fairly well with each other. Significant differences are along the centre line and at the bubble necks. The thickness of the bubble along the centreline is larger in the SPH result. The upper surface of the bubble from SPH matches well with LS solution, but the lower part is lower in the SPH solution. However, the necks are thinner in the SPH solution. This suggests that the vertical jet is stronger in LS simulation. After breaking down, LS simulation shows more and larger detached bubbles created. The additional smallest bubbles appear and then disappear in LS

simulation but not on SPH simulation. That is probably due to poor resolution and mass conservation in LS.

Figure 3.8 shows SPH simulations using different surface sharpness control parameter. In the figure, we can see the importance of surface sharpness in this case. On the left, without surface sharpness, the bubble appears to be bursting while on the right the bubble surface retains its sharpness.
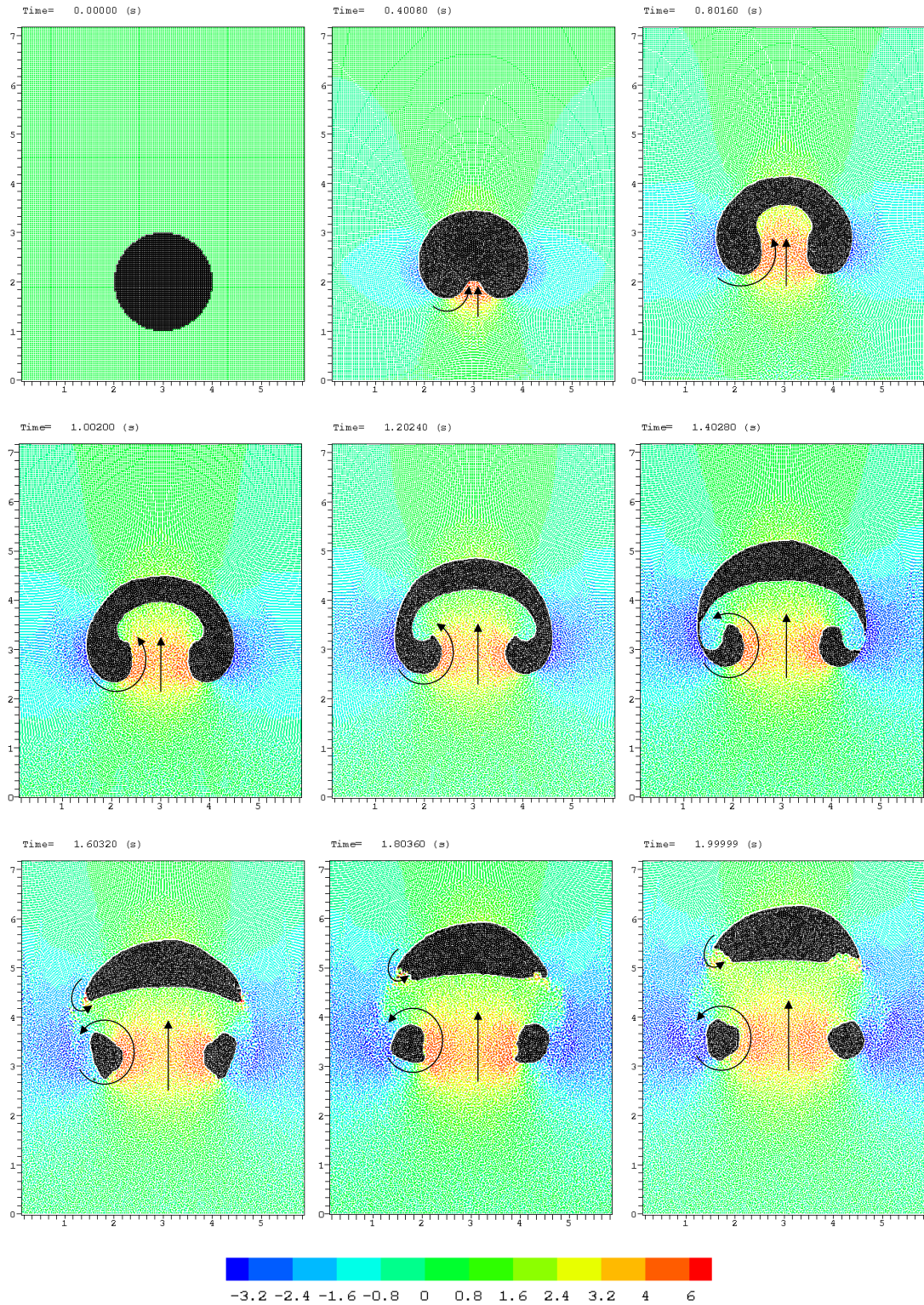
Figure 3.6. Snapshots of vertical velocity fields of water around a rising air bubble. Vectors show the direction of water flow.
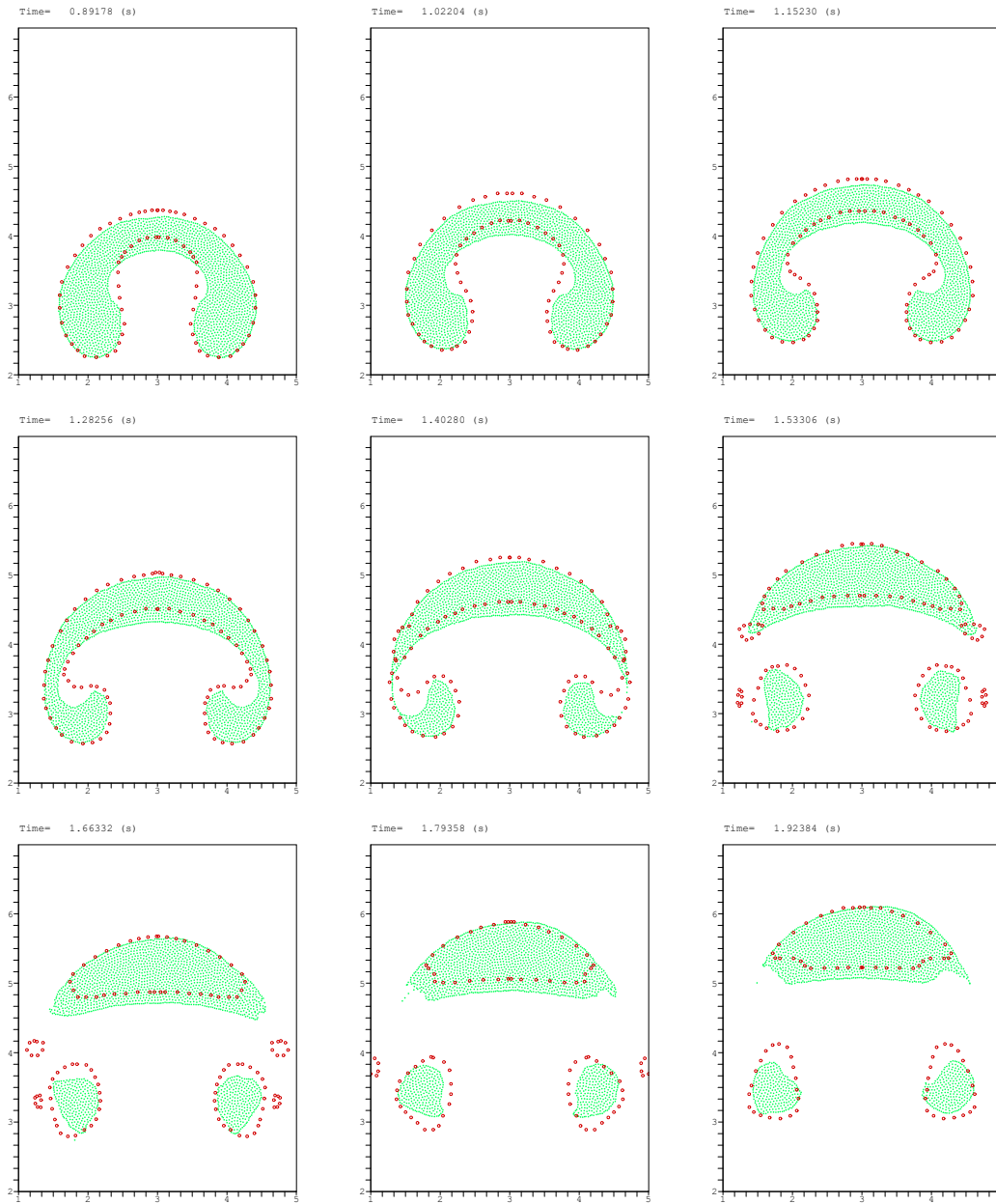
Figure 3.7. Evolution of simulated air bubble rising in water (green dots) compared with LS simulation (red circles). Only air particles are plotted.
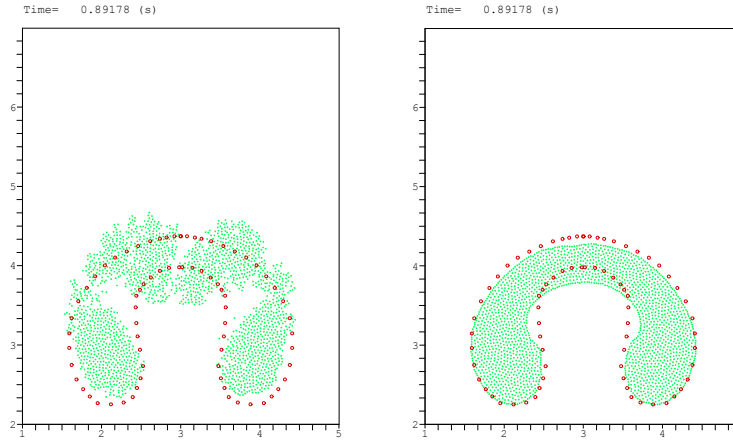
Figure 3.8. Simulated air particles (green dots) with different surface sharpness options used. Left: no sharpness control; Right: surface sharpness parameter a = 15000 (right). LS simulation (red circles) is plotted for reference.

The normalized energy of the air-water system is plotted in Figure 3.9. It can be seen that during the evolution, potential energy is almost perfectly transformed into kinetic energy, the total energy of the system remains close to the initial energy.
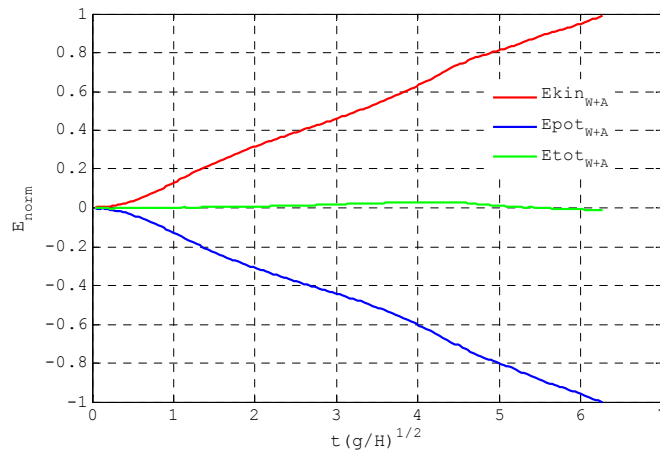
Figure 3.9. Energy of the system.

3.3   Dam break and impact of water on vertical wall

The configuration of the dam break problem is shown in Figure 3.10. The water body after a sudden break of a dam is numerically represented as an initial rectangular column of water supported by the horizontal bottom of a water tank. The left side of the water column is a vertical wall of the tank. The other vertical side of the water column is the water-air interface which is free to evolve under gravitational force. After the dam breaks, water spreads quickly over the dry bottom of the tank. The water front then impacts on the right wall of the tank developing an upward jet. The developed jet reverts and overturns, forming a strong plunger and entrapping large amount of air.

The dam break problem has been studied experimentally in the past (Zhou et al., 1999). Results of water surface height, impact pressure on the right wall from the experiment can be used to verify the current SPH method.

For comparison, the dam break experiment in Zhou et al. (1999) is reproduced using SPH. The dimension of the tank is $D{\times}L = 3.33H \times 5.366H$. The height and width of the water column are $H = 1.0$ m, and $W = 2H$. The SPH simulation uses 28,800 water particles of size $0.00833H$ (and 228,800 air particles in two-phase simulation). The simulation is carried out for 3 sec with time step of $2{\times}10^{-6}$ sec.
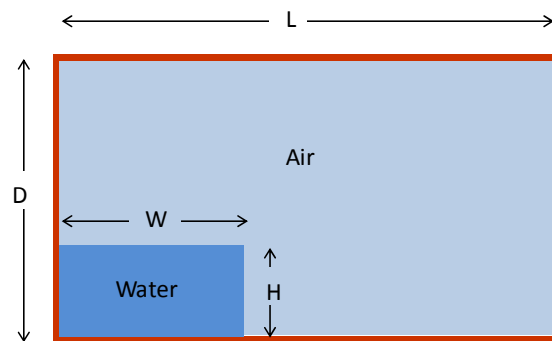
Figure 3.10. Schematic configuration and initial condition of the dam break problem.

The computed shapes of the air-water interfaces at different time instances are plotted to-gether with those obtained from BEM and LS simulations. In Figure 3.11, the SPH simulated overturning plunging tips at two time instances are compared with a BEM simulation of in-viscid flow. SPH simulation is two-phase but only water phase is plotted. Comparisons show a good agreement between SPH and BEM near the wall. A slight difference is observed at the plunging tip. The plunging tip from SPH simulation develops faster. The BEM simulation stops when the plunging tip impacts on the underlying water. At the same time, the tip from SPH simulation penetrated the water body, enclosing an air pocket.
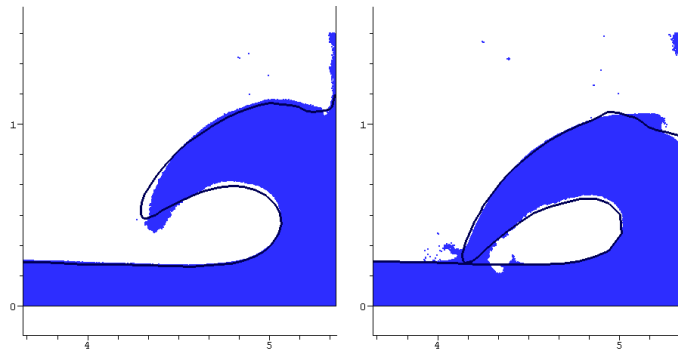
Figure 3.11. Comparisons of air-water interface solutions of SPH (blue) to BEM (black solid line) solution at dimensionless time $t(g/H)^{1/2} = 5.95$ and $t(g/H)^{1/2} = 6.2$.
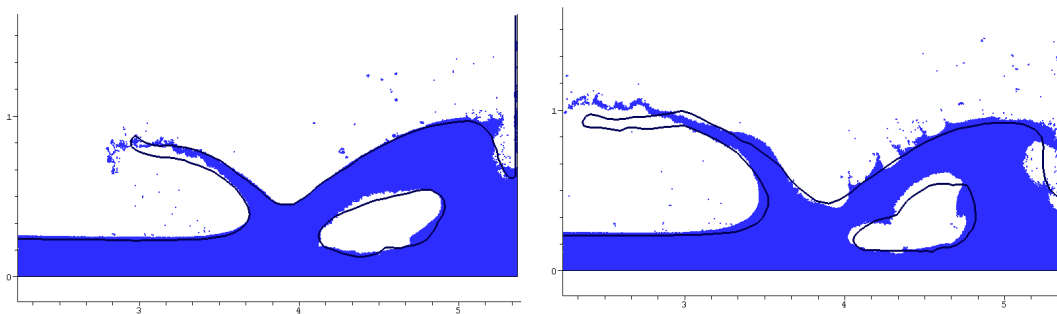
Figure 3.12. Comparisons of air-water interface solutions of SPH (blue) to LS solution (black solid line) at dimensionless time $t(g/H)^{1/2} = 6.76$ and $t(g/H)^{1/2} = 7.14$.

Figure 3.12 compares the air-water interface with the solutions from a LS simulation. Both methods produce similar results in term of capturing the interface shape. The splash-up of water following the impact of the plunging breaker on the wetted deck was captured by SPH and LS. Some water particles leaving the main bulk of fluid is observed in SPH simulation. Compared to a SPH simulation at the same resolution, the LS method is smoother but it failed to capture the fragmentation of water.

By labelling each fluid particle with a colour code, Figure 3.13 suggests a slight penetration of the plunging tip into the underlying water. The plunging tip is divided into two parts. The first part is pushed forward together with the water from the underlying surface to form a splash-up. The second part penetrates deeper into the water body and is carried along by the rolling water surrounding of the entrapped air pocket. The air pocket surface is initially smooth except for a small disturbed area near the impact location. The disturbed surface is then developed and spread over the air pocket surface due to the rolling motion. This phenomenon is typical for plunging waves and is discussed more in Chapter 4.

The total height of water column at two locations in the horizontal axis and the impact pressure on vertical wall are compared with experimental results by Zhou et al. (1999). In the experiment, standard capacitive wave gauges being used are sensitive to the wetted portion of the wire. Hence in the numerical simulations, the total height of water is computed by taking the water level deducting the height of entrapped cavity (if present). Figure 3.14 shows the time evolutions of total water height at two locations $x_1 = 4.517\,H$ and $x_2 = 3.713H$ and comparison with experiment results. At both locations the water height is characterized by a immediate hump when the deck is being flooded. This is not picked up in the numerical simulations, probably due to the deck condition such as roughness is not included in the simulations. In overall, comparisons at two locations show good agreements between numerical simulations and laboratory measurements up to the time $t(g/H)^{1/2} \approx 6.8$ (which corresponds to the

stage of splash-up formation shown in Figure 3.12, right pane). Subsequently, the total water height measured in experiment jumps sharply then reduces gradually. During this period, the two simulations deviate from experiment. At location x_1, both single-phase and two-phase simulations show similar results which under-predict the measurement. The comparison at location x_2 shows a better agreement where the two curves follow the trend of the experimental result. However, the single-phase curve over-predicts while the two-phase curve under-predicts the experiment result.
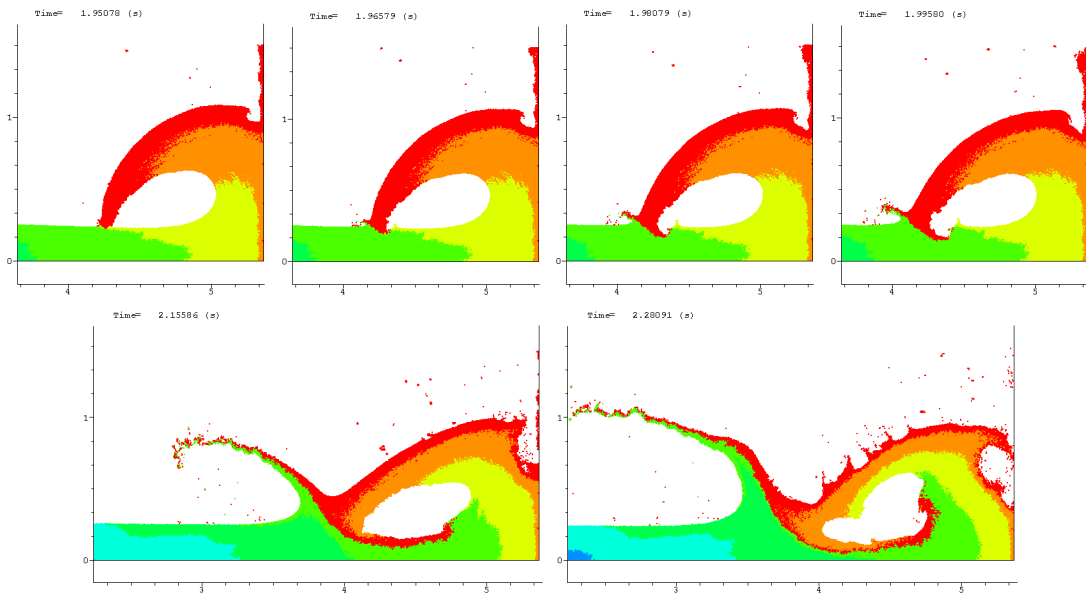
Figure 3.13. Penetration of plunging tip into underlying water and splash-up formation. Water from the plunging tip is bifurcated on impingement.

The impact pressures of the water front on the vertical wall computed from numerical simulations are plotted in Figure 3.15 together with the measurement from experiment of Zhou et al. (1999). In the experiment, impact pressure was measured by a circular pressure transducer of 0.09 m ($0.15H$) in diameter. The pressure transducer is located at the right wall of the tank and is centered at $0.267H$ above the deck. In numerical simulations, the total pressure is com-

puted based on the Bernoulli equation for compressible fluid which comprises of dynamic pressure from the moving fluid that brought to rest and the fluid pressure.

It can be seen from Figure 3.15 the SPH simulations show a good agreement to the experiment. The first pressure peak (A) at time $t(g/H)^{1/2} \approx 2.4$ corresponds to the impact of the water front against the wall. This sudden rise of pressure is well captured in SPH simulations both one- and two-phase flows since it associates mainly with the dynamics of the water front. The peak of impact pressure from the numerical simulation is about twice larger than that measured in the experiment.

(a)

(b)
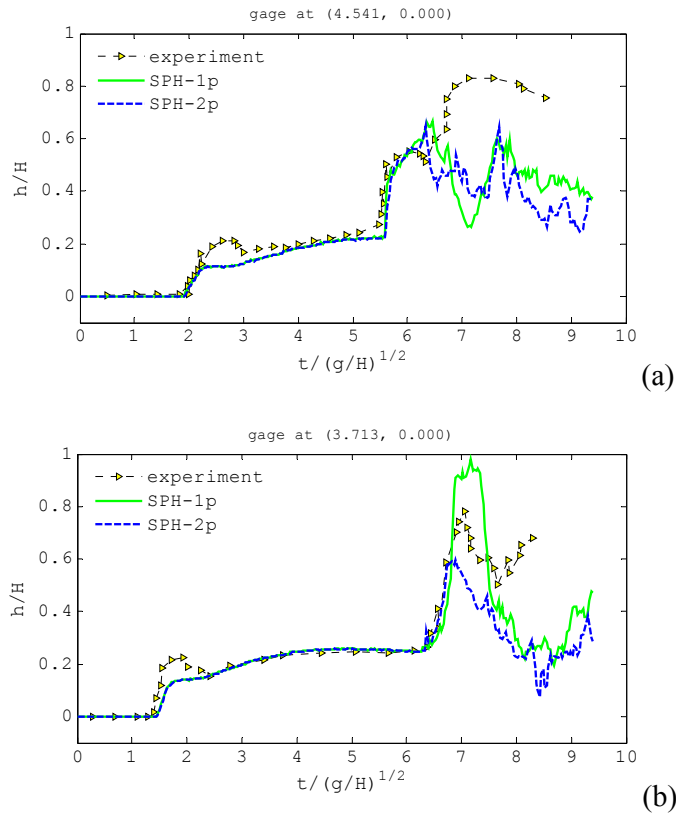
Figure 3.14. Time evolution of total water height at locations (a) $x_1/H = 4.517$ and (b) $x_2/H = 3.713$. (SPH-1p stands for single water phase, SPH-2p is air-water two phase simulation)

The backward plunging water jet impinging on the water surface induces the second pressure peak (C) at time $t(g/H)^{1/2} \approx 6$. The numerical simulations show a delay of the rising time of this pressure peak. There are several pressure peaks observed in the two-phase flow simulation while less peaks are seen in single-phase simulation. The higher number of peaks in the two-phase simulation may be attributed to the compression and expansion of the entrapped air pocket. These oscillations are also observed in the measurement although the magnitude is smaller. There are two high pressure peaks occurring in very short durations shown in single-phase curve at $t(g/H)^{1/2} \approx 8.4$ and 9.2 (E and F). These pressure peaks are unrealistic and they are associated with the collapse of the void pocket where the top part of the plunging wave falls on the water part beneath. This comparison clearly shows the important effect of air-cushion to the impact pressure on structures.
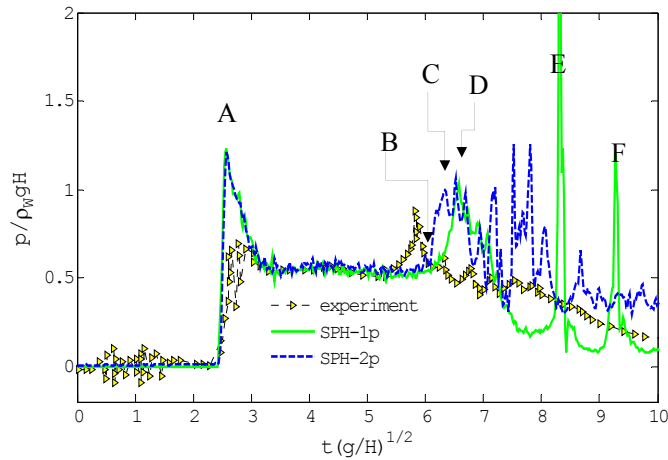
Figure 3.15. Evolution of total pressure single-phase and two-phase simulations on the vertical wall at location *(x, z)/H* = (5.366, 0.267).

Figure 3.16 shows the fractions of the hydrostatic and dynamic pressure components contributing to the total pressure at the wall computed from the two-phase flow simulation. At the time of the impact, pressure rises sharply due to the fast moving fluid brought to rest, the kinetic energy almost transforms to potential energy (represented in term of pressure). After

that, a part of potential energy converts back to kinetic energy, containing in the vertical water jet (see Figure 3.17a). At the time when the second peak occurs, the contribution from dynamic pressure is very small. It can be seen on Figure 3.17b that the flow speed near the wall is close to zero. The rise of pressure is mainly due to the impact of the falling jet on the underlying water and the pressure propagating through water and the compressing air pocket.
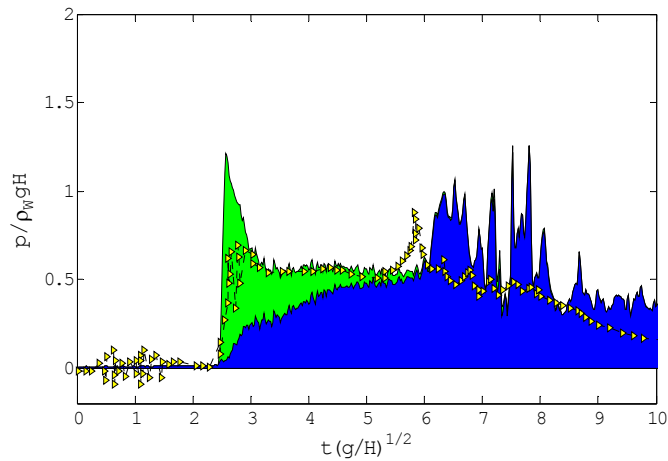
Figure 3.16. Fractions of static pressure (blue) and dynamic pressure (green) contributing to the total pressure.

(a)   (b)
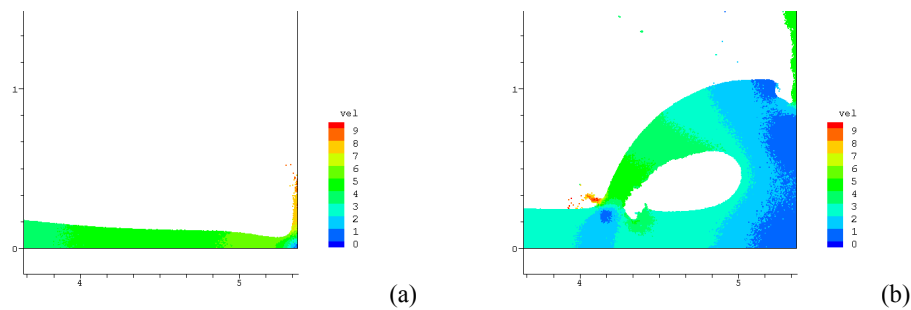
Figure 3.17. Velocity field near the wall of the two-phase simulation (only water phase is shown) at the times of the first (A) and second peaks (C) occurring

A

sensor

B

C

D

E

(a)　　　　　　　　　　(b)
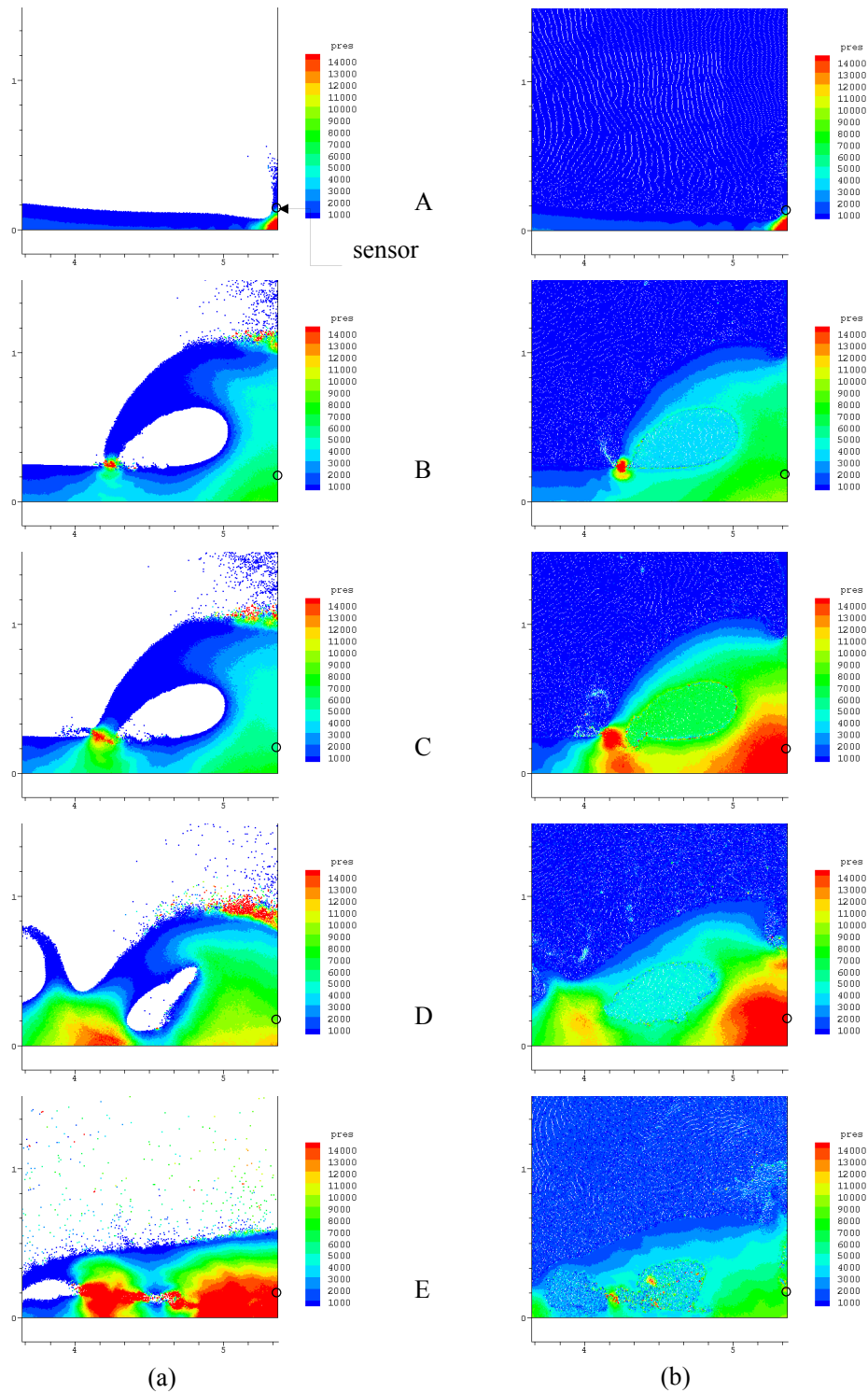
Figure 3.18. Static pressure field near the wall of single-phase (a) and two-phase (b) simulations at the times of the simulated peaks (A, B, C, D, E in Figure 3.15) occurring. The circle in each snapshot is the location of the pressure sensor.

Snapshots of the static pressure distribution near the right wall of the tank corresponding to the time instances labelled as A – E in Figure 3.15 are shown in Figure 3.18. The snapshots are taken from single-phase (left column) and two-phase simulations (right column). It can be seen at time C and D the air pocket is compressed and the fluid pressure is significantly higher in the two-phase simulation. At time E, collapse of the plunger in the single-phase simulation results in an extremely high pressure near the wall. Note, however, that the entrapped air pocket immediately disappears at collapse and this is inconsistent with the physics of air entrapment and breakdown into bubbles during breaking.

The kinetic, potential and total energy of the one- and two-phase flow simulations are given in Figure 3.19. The total energy error is defined as $(E_T - E_{T0})/E_{T0}$, where E_T is total energy and E_{T0} is the initial total energy. One can observe several oscillations in the kinetic and potential energy (such as those at $t(g/H)^{1/2} \approx 3$ and $t(g/H)^{1/2} \approx 6.5$). These oscillations may be associated with the peaks of impact pressure shown in Figure 3.15 which implies that the kinetic energy being transferred to potential energy during the impact. In both cases, the total energy dissipation is very small during pre-breaking stage of the backward plunger. During breaking, energy dissipates quickly. At time $t(g/H)^{1/2} = 10$, total energy is reduced by 30%. The two-phase simulation shows faster energy dissipation.
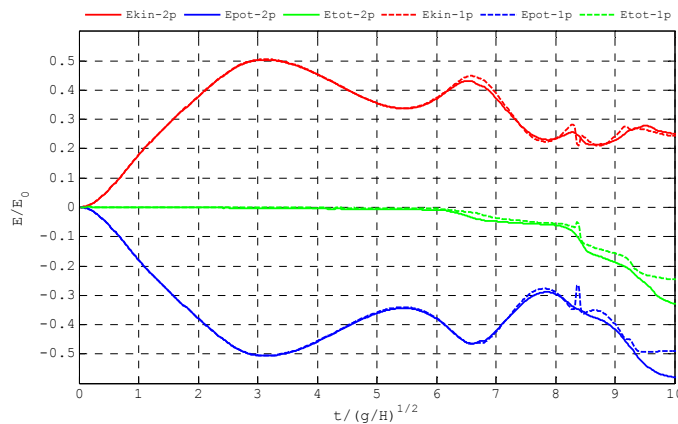
Figure 3.19. Energy plots for two-phase (solid lines) and single-phase (dash lines) simulations of the dam break problem.

A comparison of different two-phase SPH simulations using different key numerical parameters (numerical sound speed, smoothing length and viscosity model) is also carried out. Three scenarios are simulated. The parameter settings of the scenarios are given in Table 3.1. Results of air-water interfaces, impact pressures on vertical wall and wetted heights at the two locations are plotted in Figure 3.20 to Figure 3.22.

Table 3.1. Scenarios and parameters for different SPH simulations of dam-break problem.

Scenario ID	Sound speed in water	Sound speed in air	Smoothing length h/dx	Viscosity model
C1	27.124	108.4	1.33	Artificial viscosity
C2	27.124	108.4	1.33	Turbulence (LES)
C3	20	20	2	No viscosity
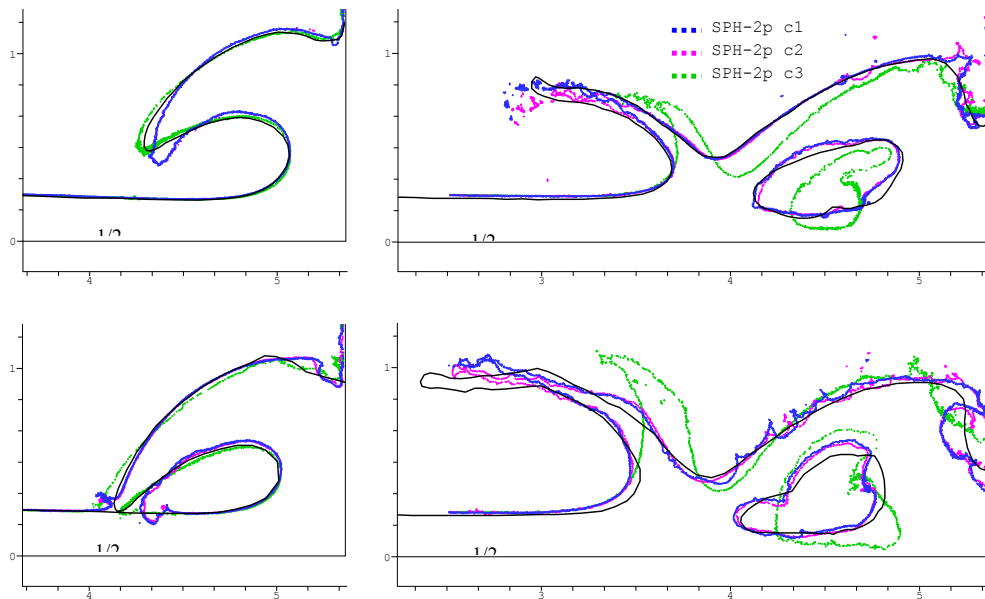
Figure 3.20. SPH simulated air-water interfaces solutions at different numerical parameters. BEM (left) and LS (right) solutions (black solid line) are plotted for reference.
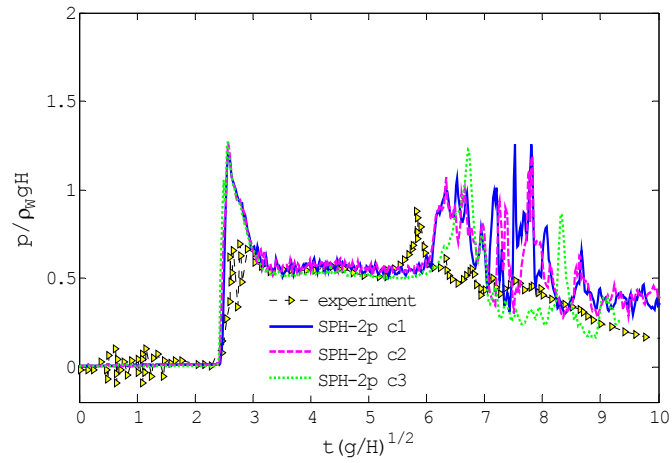
Figure 3.21. SPH simulated total pressures on the vertical wall at location (x, z)/H = (5.366, 0.267).
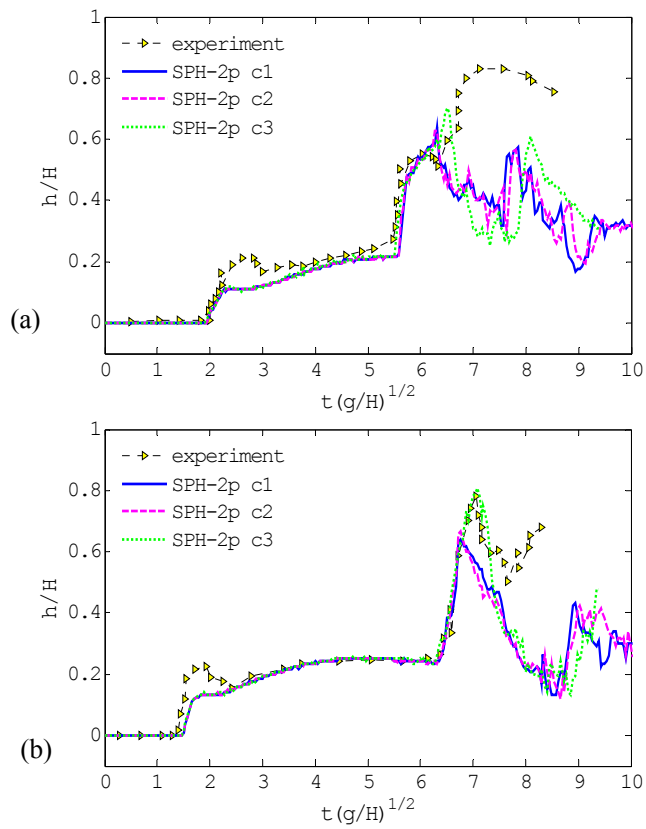
Figure 3.22. SPH simulated total water heights at locations (a) x_1/H = 4.517 and (b) x_2/H = 3.713.

We can see that the results from simulations of C1 and C2 are almost similar. It suggests that the viscosity model has minor influence to the numerical results. In Figure 3.20, the air-water interfaces from simulations of C1 and C2 develop faster than BEM solution but agree very well with LS solution. Results of air-water interfaces from simulation of C3 agree well with BEM solution but deviate significantly from LS simulation. It is noted that in BEM simulation the fluid is non-viscous and dissipation is small while in LS simulation fluid is viscous and dissipation is higher.

The impact pressure results from the three simulations agree well with each other until the second peak of pressure occurring as shown in Figure 3.21. After that, pressures from C1 and C2 are oscillatory with many large peaks and slow decay. The pressure from C3 shows two large peaks and small oscillation. The decay rate of pressure in C3 is faster and closer to the measurement.

The total water heights computed from the three simulations also agree very well with each other until the time the second pressure peak occurs as shown in Figure 3.22. After that, the total water heights from C3 are higher and match better with the measurement than that from C1 and C2. At location x_2, the C3 simulation successfully captures the peak of the total water height.

Overall, the C3 simulation agrees better with the measurement and BEM although it deviates significantly from LS simulation. A possible reason is the high dissipation rate in LS and C1, C2 simulations. The C3 setting will be used for the later simulations.

3.4   Water wave propagation in a long flume

The SPH simulations presented above are at small spatial and temporal scales. Within a short time, the numerical dissipation has not significantly affected the results. For problems of lar-

ger scales, dynamics evolve over a long time scale and numerical dissipation could accumulate and drastically changes the results. The difficulty in simulating slow dynamics and large dissipation are commonly found in many numerical methods. With SPH, choosing the right numerical parameters such as resolution, time step, and smoothing length would help to mitigate the numerical dissipation.

The problem of wave propagation in a wave flume is simulated to test the SPH method as well as to obtain the best set of numerical parameters for the later simulations of the wave breaking problem. The configuration is shown in Figure 3.23. The flume has dimensions of 36 m long and 2.4 m height. The water depth is 0.8 m. The bottom surface is assumed flat and smooth. The horizontal moving piston is initially located at 0.5 m from the left wall (or 35.5 m from the right wall). In cases of sinusoidal wave generation, this initial position coincides with the mean paddle position. This configuration of the water flume follows that of the laboratory experiment conducted by Kway (1998, 2000).
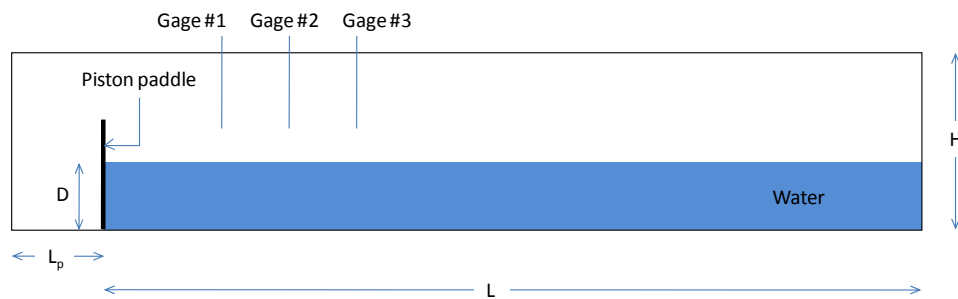
Figure 3.23. Dimension of the water flume and setup of the numerical experiment.

A parametric sensitivity study of wave propagation in a water flume, validations of sinusoidal wave propagation and wave breaking with laboratory experiments are carried out. All SPH simulations used in these numerical experiments are single phase.

3.4.1 Sensitivity study of wave propagation simulation

A signal is sent to the paddle to generate a series of sinusoidal waves (short wave) of predefined amplitude (0.05 m) and period (1 sec). SPH simulations are carried out using different combination of smoothing length coefficients *hc* (*hc* = *h*/*dx*), time steps *dt* and resolutions (particle sizes) *dx*. Time series of water elevations at the wave gauges are compared with each other to find the best combination of these parameters. Results are given in Figure 3.24 – Figure 3.26.
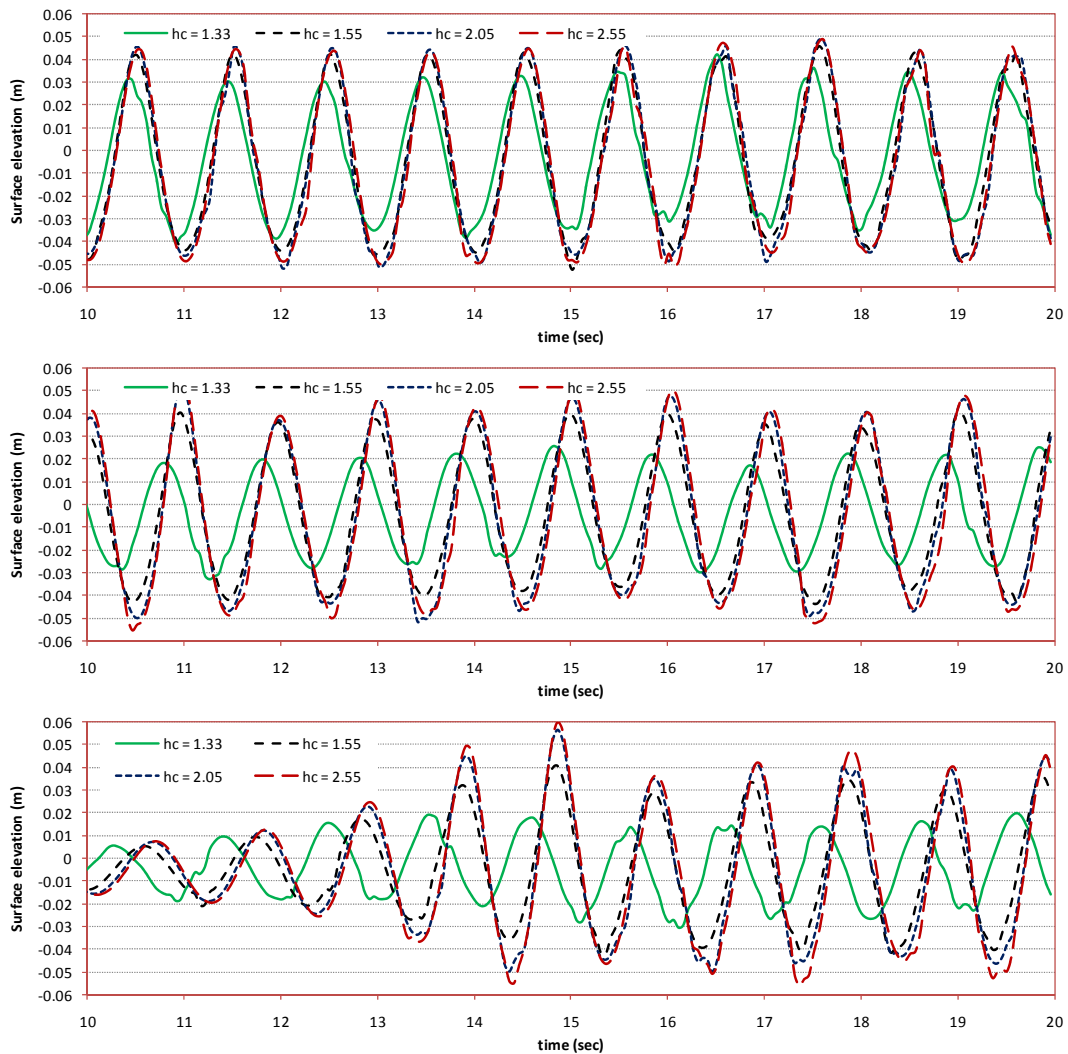
Figure 3.24. Simulated water levels of sinusoidal waves at gauge #1 (4.5 m from the mean paddle position), gauge #2 (9.0 m) and gauge #3 (12.0 m). Four different smoothing length coefficients are used. Time step and resolution are fixed at *dt* = 2×10⁻⁵ sec and *dx* = 0.01 m.
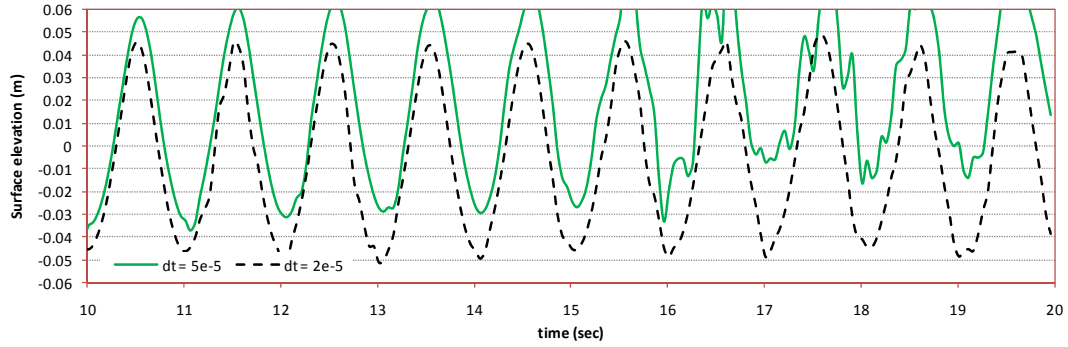
Figure 3.25. Simulated water levels of sinusoidal waves at gauge #1 (4.5 m from the mean paddle position). Two different time steps are used. Smoothing length and resolution are fixed at *hc* = 2.05 and *dx* = 0.01m.
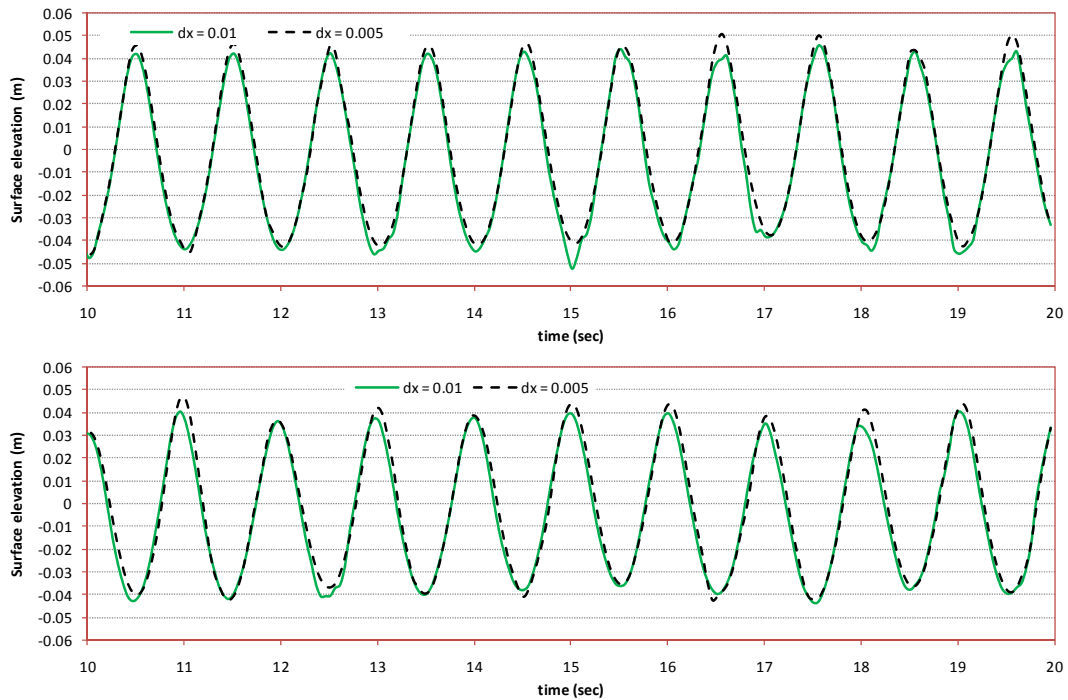
Figure 3.26. Simulated water levels of sinusoidal waves at gauge #1 (4.5 m from the mean paddle position) and gauge #2 (9.0 m). Two different resolutions are used. Smoothing length is fixed at *hc* = 1.55. Time step changed accordingly to resolution.

It can be seen from the results plotted in Figure 3.24 that the wave height reduces quickly when the smoothing length coefficient $hc = 1.33$ is used. The use of larger smoothing length coefficients reduces the dissipation rate. As a result, wave amplitude remains closer to the initial value. Small dissipation is observed with $hc = 1.55$. Some overshooting peaks are obtained when $hc = 2.05$ and this increases when $hc = 2.55$. Using lager smoothing length is theoretically more accurate. It is true inside the fluid. However, large smoothing length could cause particles at one or two layers at the free surface to detach from the fluid, resulting in the overshooting of surface elevation as observed in the $hc = 2.55$ curve in Figure 3.24. The results suggest that suitable smoothing length coefficients should be chosen in the range between 1.55 and 2.05.

Fixing the smoothing length coefficient at $hc = 2.05$ and resolution at $dx = 0.01$ m, the simulation are conducted with time steps $dt = 5 \times 10^{-5}$ sec and $dt = 2 \times 10^{-5}$ sec. The results are shown in Figure 3.25. The results with $dt = 5 \times 10^{-5}$ suggests that the free surface kept rising and eventually blows up. It is recommended that the Courant number, $Cr = c_s \times dt / dx$, should be less than 0.2 to prevent the simulations from blowing up.

The comparisons of SPH simulations using two different resolutions, dx, are shown in Figure 3.26. The smoothing length coefficient is fixed at $hc = 1.55$ while the time step is adjusted to satisfy Courant condition. The surface elevations at two wave gauges located at 4.5 m and 9 m from the paddle are presented in the figure. It can be seen from the figure that both resolutions yield good results. The use of smaller dx clearly converges closer to the initial wave amplitude of 0.05 m.

3.4.2 Sinusoidal wave propagation

In the second experiment, a set of suitable numerical parameters are used in the simulations of the sinusoidal wave propagation and compared with a laboratory experiment. Input signal

(the same as that used in experiment) is sent to the paddle to generate a series of sinusoidal waves. The period of the input signal is 1 sec and the stroke of the wave paddle is 0.042 m. Experimental result showed wave amplitudes of 0.03m at the trough and 0.037m at the crest. Water elevations at the two wave gauges (4.5 m, 9 m from the mean paddle position) are compared with the records from the laboratory experiment (see Figure 3.27).

As shown in Figure 3.27, the agreement with measurements at gauge #1 is good although the troughs appear to be under-predicted. Flatter troughs in the actual measurement suggest that the waves in the experiment exhibit more nonlinearity than those in the numerical simulation. At gauge #2, a small phase shift is observed. The simulated time history slightly over-predicts the amplitude obtained in the measurement.

Figure 3.27. Comparison of SPH-simulated and measured water level of sinusoidal waves at gauge #1 (4.5 m from the mean paddle position) and gauge #2 (9.0 m).

3.4.3   Simulation of wave breaking

Having derived suitable parameters for the simulation of waves in a 36 m long wave flume, a simulation of the modulation and focusing a wave packet is carried out. An amplitude and frequency modulated signal as presented in Section 2.4.1 is sent to the wave paddle to produce a propagating wave packet (see Figure 2.20). The properties of the wave packet are as follows: number of sinusoidal components: 28; frequency ranging: 0.56 Hz to 1.1 Hz; central frequency: 0.83 Hz (5.21 rad/s); designed focal distance: 14.0 m (Table 3.1 in Kway (2000)); breaking distance: 15.2 m (Table 1 in Kway (1998)); and focal time: 26.0 sec. The actual focal distance and time measured from the laboratory experiment are 14.0 m and 25.8 sec (as shown in Figure 4 and Figure 5 in Kway (1998) and Figure 3.11 and 3.12 in Kway (2000)), respectively. Note that these focal distance and time were intuitively estimated from the photographs taken during the experiment, and thus are very subjective.

Computed surface elevation time histories at three wave gauges, #1, #2 and #3 (4.5 m, 9 m and 12 m from the mean paddle position) are compared with those measured from the experiment in Figure 3.28.

Very good agreements between the curves can be observed in Figure 3.28. At gauge #1, the numerical result almost matches very well with the experiment, except for minor deviations at the wave troughs and crests. At gauge #2 and #3, similar agreements are obtained. A slight phase shift can be seen at gauge #2 and this increases slightly at gauge #3.

Snapshots of simulated wave profiles at its focal time zoomed in at the focal point are plotted in Figure 3.29 and Figure 3.30. The background color codes are the pressures and the horizontal and vertical velocity components of the water respectively. It can be seen in Figure 3.29 and Figure 3.30 that the focal point is at $x = 14.2$ m and focal time is 25.7 s. As the mean paddle position is at $x = 0.5$ m (see Figure 3.23), the focal point is 13.7 m from the mean

paddle position. These values are closely agreed with the values obtained from the laboratory experiment (14.0 m and 25.8 s, respectively). The breaking jet impinges on the front water surface at 14.7 m from the mean paddle position. This value reasonably agrees with the experimental value of 15.2 m of the breaking point in Kway (1998). The small differences in focal distance and focal time are probably due to many factors including the use of derived paddle signal that is not exactly the same as the signal used in the experiment, the nonlinearity being not captured, and some experiment conditions being not modelled in the numerical simulation.

Some characteristics of the generated wave packet can be seen from the snapshots in Figure 3.30 that the horizontal velocity of the water at the wave crest is around 1.4 m/s. The wave crest celerity estimated from consecutive snapshots from the simulation is around 2 m/s. When the wave starts to break, water velocity at the crest increases to above 2 m/s which is higher than the speed of the wave crest. Wave length (measured horizontally from trough to trough both sides of the wave crest) is 2.3 m and wave height (measured vertically from the wave crest to the wave trough right ahead) is 0.26 m. The wave height over water depth ratio is 0.325.

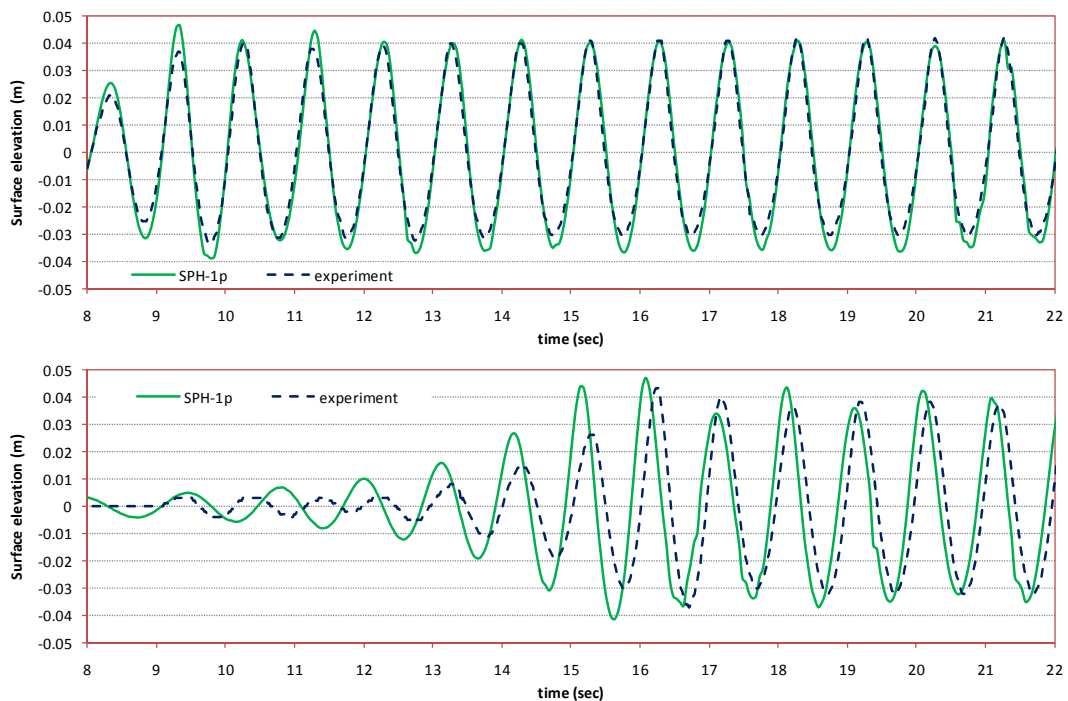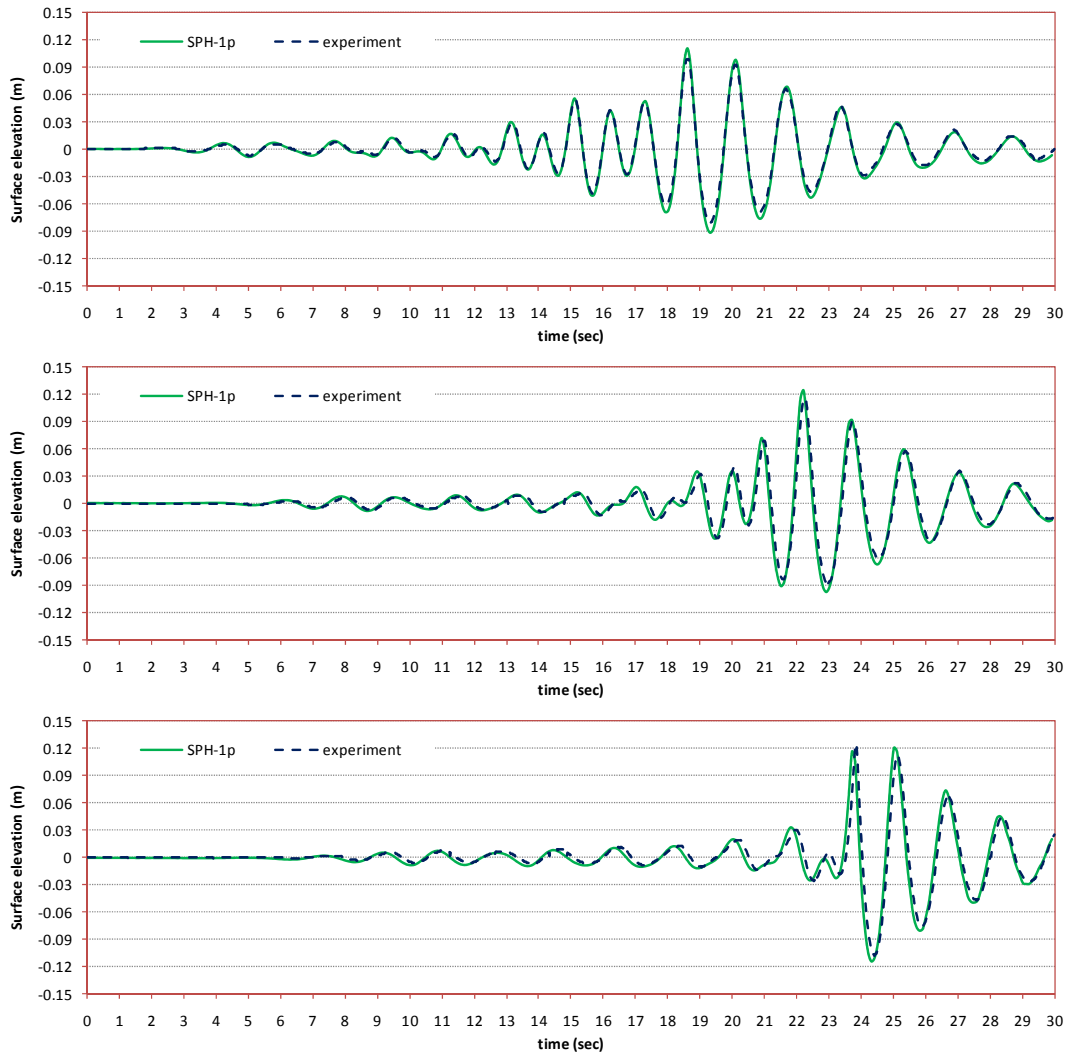**Figure 3.28. Comparison of SPH-simulated and measured water level at gauge #1 (4.5 m from the mean paddle position) gauge #2, (9.0 m) and gauge #3 (12.0 m).**
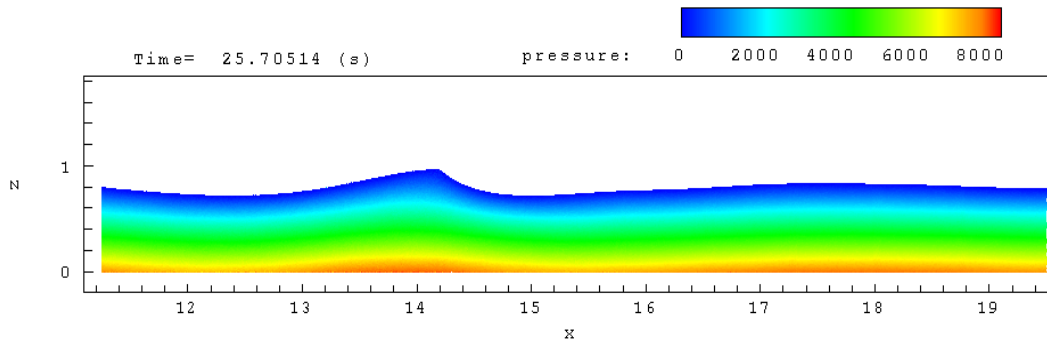
Figure 3.29. SPH-simulated pressure field (N/m^2) around the focal point at focal time.
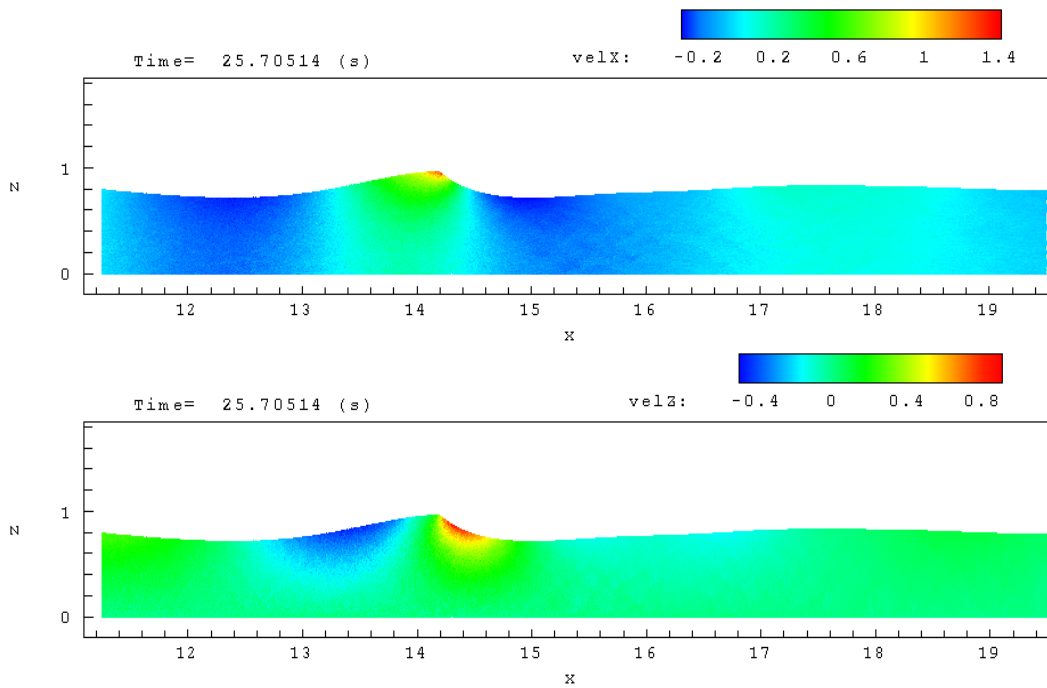
Figure 3.30. SPH-simulated horizontal (velX) and vertical (velZ) velocity field (m/s) around the focal point at focal time.

3.5   Conclusion

Above calibration and sensitivity studies have shown that the current SPH program can yield good results if suitable setting parameters are used. It is apparent that the higher resolution is used, the better result can be obtained. However the resolution is usually constrained by the computational resources. At a given resolution dx, the smoothing length, $hc = h/dx,$ should be in the range of 1.55 to 2.05 and the computational time step dt satisfies the Courant number, $Cr = max(c_s) \times dt/dx < 0.2$. The suitable numerical sound speed c_s in water is around 20 m/s. Numerical sound speed in air is 20 – 40 m/s. In simulations of air dynamics with relative low pressure compared with surrounding water, the sharpness control is not necessary. These parameters will be used in the fine simulation of wave breaking in the next chapter.

Although the input signal to the wave paddle is not exactly the same as the signal used in the experiment, it generates a wave packet that agrees well with the measurement at the time prior to breaking. Hence, the wave and flow conditions at the focal time are extracted and interpolated to a much finer resolution for a nested two-phase simulation of the breaking process. The extracted domain is from $x = 11.4$ m to $x = 19.1$ m. The interpolation uses the same kernel function as that used in the SPH simulation. Results from the nested two-phase simulation are investigated and presented in Chapter 4.

Chapter 4. Numerical Simulation and Physical Investigation of a Deep Water Plunging Wave

The overall objective of this thesis is to develop a deeper understanding of the physics of plunging waves in deep water. Details and key features that are still not well understood include:

- Plunging jet at pre-breaking stage: geometry of the wave, formation and movement of the plunging jet.

- Dynamics of the wave: impingement of the plunging jet on the underneath water surface, formation of the air-tube, source of the instability/disturbance that spreads over the air-tube surface, formation of the splash-up, vertical jet and interaction of the falling vertical jet and the coming wave crest; pressure, velocity fields and turbulence.

- Dynamics of air: compression and decompression cycles of the entrapped air, formation of sprays of water, formation of air bubbles, circulation of surrounding air.

- Dissipation of wave energy.

The validation analyses in Chapter 3 have shown that the SPH methodology, with appropriate resolution, nesting and treatment of the boundary condition including the inclusion of an air layer could adequately simulate such a complex process. Based on the process to simulate a plunging wave (Section 3.4.3) further refinement is carried out to simulate the near field details of wave plunging.

4.1   Initial condition for detailed near-field simulation of wave plunging

The initial condition of the nested simulations is interpolated from the coarser single-phase simulation (presented in Section 3.4.3) at the focal time t_f = 25.7 s (Figure 3.29 and Figure 3.30). The air layer is initiated from rest with zero pressure and reference density (density of air at zero pressure). To reduce the shear stress between the water and air when the system starts, a layer of air particles near the interface is prescribed with velocities extrapolated from the water particles near the interface using the kernel approximation. This kernel interpolation uses the same kernel function and smoothing length as those used for approximating the governing equations. Both water and air particles are included in the kernel's support domain. The thickness of the air layer is chosen to be at least twice of the water depth to reduce the effect of the ceiling of the wave flume to the air dynamics near the air-water interface. The initial pressure ($p/\rho_0 gD$), density (ρ/ρ_0) and velocity (u/C, w/C) of the air-water system near the wave crest are displayed in Figure 4.1. Here, g = 9.81 m/s^2 is gravitational acceleration, ρ_0 = 1.2 kg/m^3 is the reference air density, D = 0.8 m is the initial water depth of the wave flume, and C = 2 m/s is the speed of wave crest prior to breaking. The dimension of the nested domain is $9.5D$ long and $3D$ high (= 7.6m×2.4m). The periodic boundary condition is used for the nested simulation. The duration of the simulations is t_w = 5.6. Here, t_w = $(t - t_f)(g/D)^{1/2}$ is the dimensionless time.

The SPH simulations involve 22,800,000 particles, in which the number of water particles is 6,013,907. The resolution (initial particle size) and computational time step are dx/D = 0.00125 and dt_w = 7×10^{-6}, respectively. Smoothing length coefficient is h/dx = 2.1. The numerical sound speeds in water and air are c_{sW}/C = 10 and c_{sA}/C = 20, respectively. These sound speeds correspond to 20 m/s in water and 40 m/s in air.
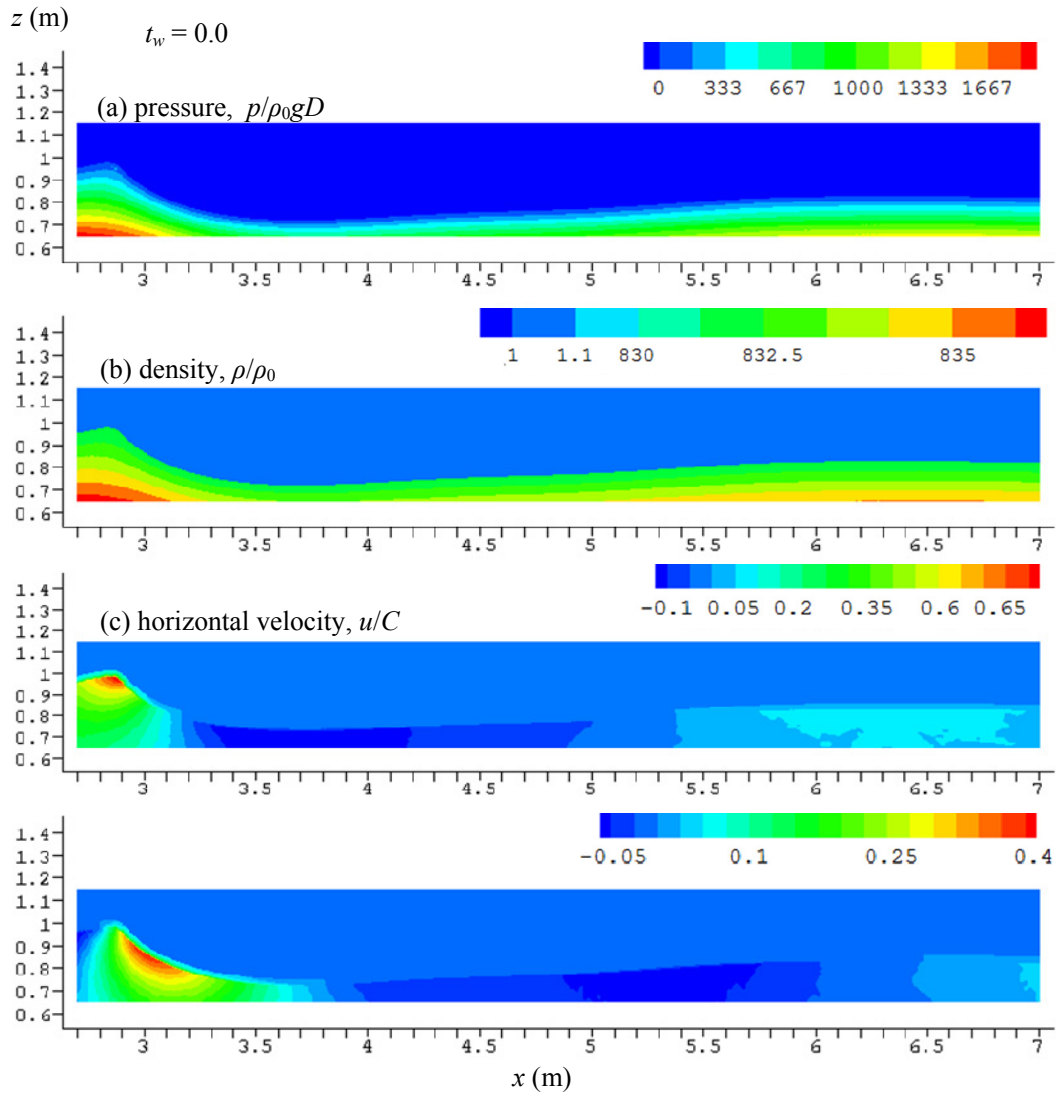
Figure 4.1. Initial conditions of the nested simulation of the air-water two-phase flow near the wave crest.

4.2 Overall wave plunging process

The overall wave plunging process and the distribution of pressures and velocities of water and air are shown in Figure 4.2 - Figure 4.3. It can be seen from the sequential snapshots in Figure 4.2 that when the wave moves from left to right, the crest becomes steeper. A plunging jet is formed at the top of vertical front face of the wave and project forward. The plunging jet curls over and impinges on the water front, entrapping an air tube and, at the same time, generating a water splash-up ahead of it. The development process of plunging jet from its formation to impingement on the water front takes an time amount of $\Delta t_w = 0.74$. The entrapped air tube, having an elongated elliptical shape initially, changes its shape while moving forward with the wave. The initial water splash-up develops to a strong vertical jet in front of the plunging jet. The top of the vertical jet projects forwards. The plunging jet keeps moving forward and impinging on the water front at the base of the vertical jet. A back flow portion develops at the rear of the vertical jet and impinges on the plunging jet, entrapping a second air pocket. Vertical sprays of water are generated above the wave crest. This whole process take an time amount of $\Delta t_w = 1.92$. The entrapped air pockets break in to smaller bubbles in the water column. Large bubbles resurface and burst off, generating foamy water surface. Small bubbles entrain deeper in the water column. At the same time with the impingement of the back flow of the vertical jet, the forward flow, which is similar to a plunging jet, impinges on the water surface ahead of it, entrapping an air pocket and generating a second water splash-up.

The water pressure distribution in Figure 4.2 shows that, in general, water pressure almost follows the distribution under a non-breaking wave, i.e. pressure increases with the increase of distance from the water surface. High pressure is also spotted near the water surface at the areas where the plunging jet impinges on the water front and where the collapsing vertical jet impinges on the water front and on the plunging jet. In the plunging jet and the vertical jet,

pressure distribution is close to zero. The distribution of air pressure shows higher pressure areas in the air tube, in front of the vertical jet and at some spots behind the wave which are at the centers of vortices.

The velocity distribution in Figure 4.3 shows that water velocity is below $0.1C$ in the water body and is as high as $1.25C$ at the plunging jet and the vertical jet. Water velocity exceeds $1C$ when the vertical wave front is formed and a jet starts ejecting. During breaking, water velocity under the wave reduces quickly. The air velocity distribution indicates a series of vortices is generated in the air above the wave crest and moves backward relatively to the wave crest. A strong shear is observed near the wave crest when the plunging jet develops. Air velocity exceeds $2.3C$ at this area. High air velocity also observed in front the vertical jet and subsequent jets.

Details of the process and physics of the phenomena observed above are discussed in the following sections.
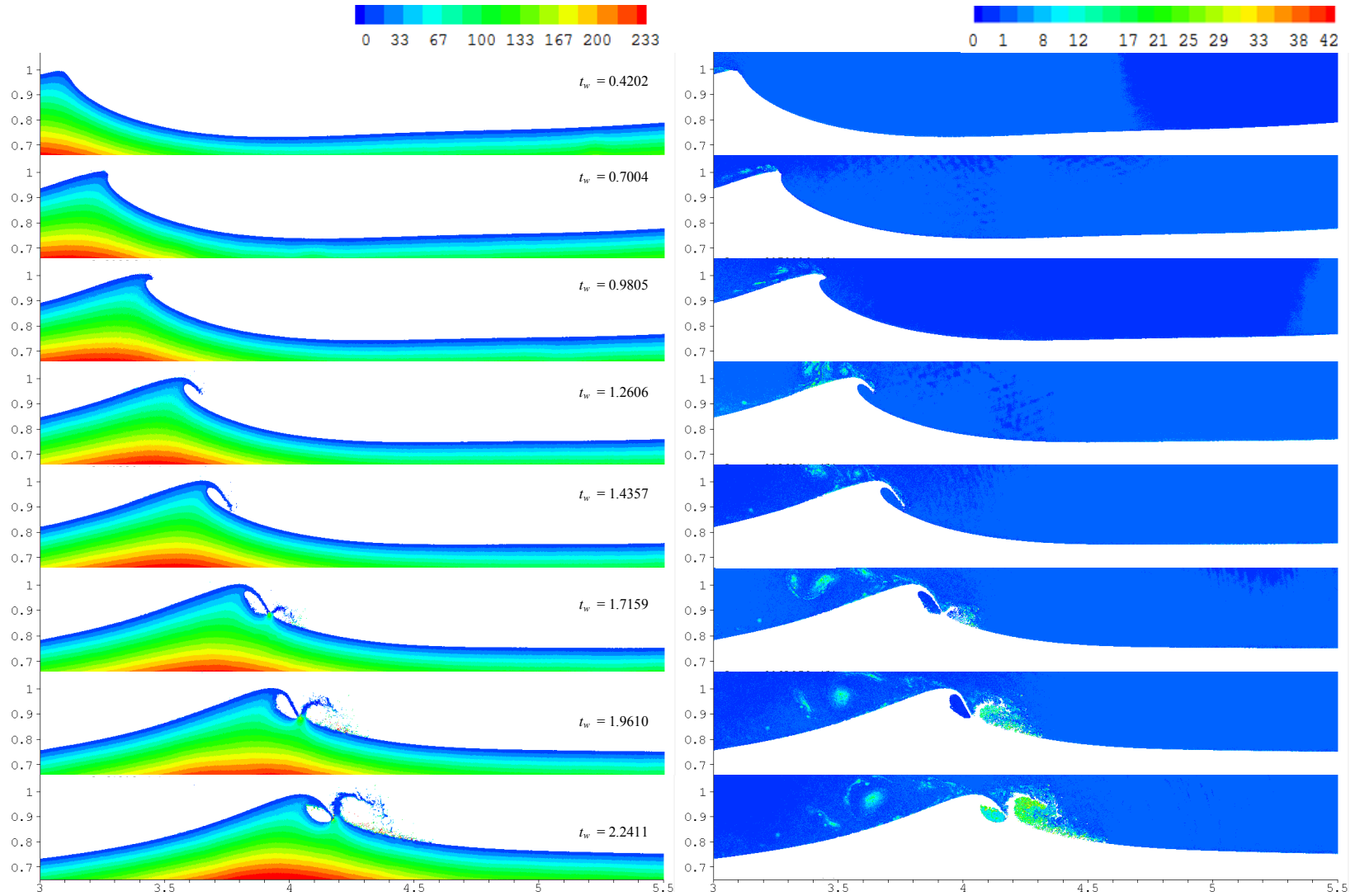
(continued on next page)
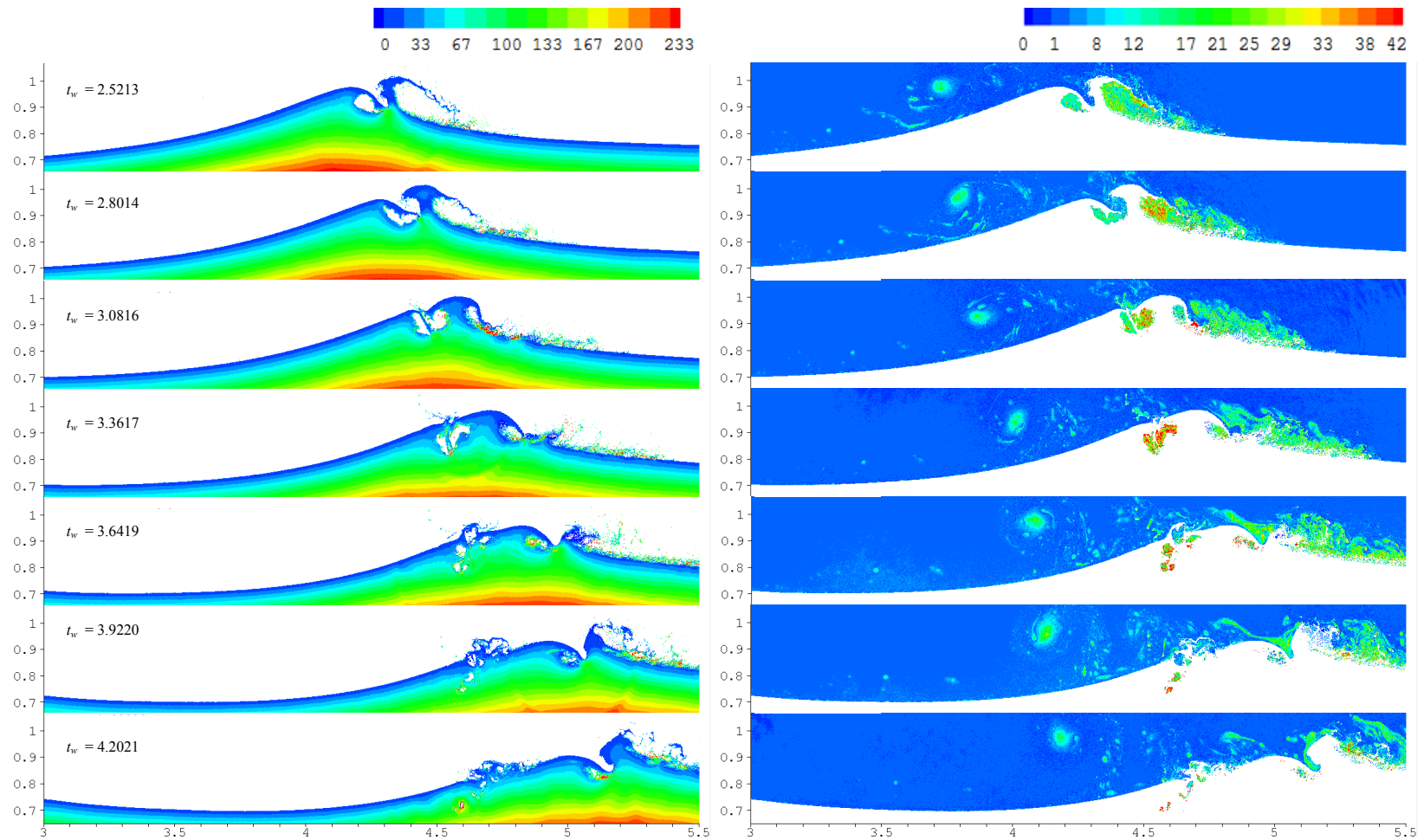
Figure 4.2. Normalized pressure ($p/\rho_0 gD$) distribution in water (left) and air (right).
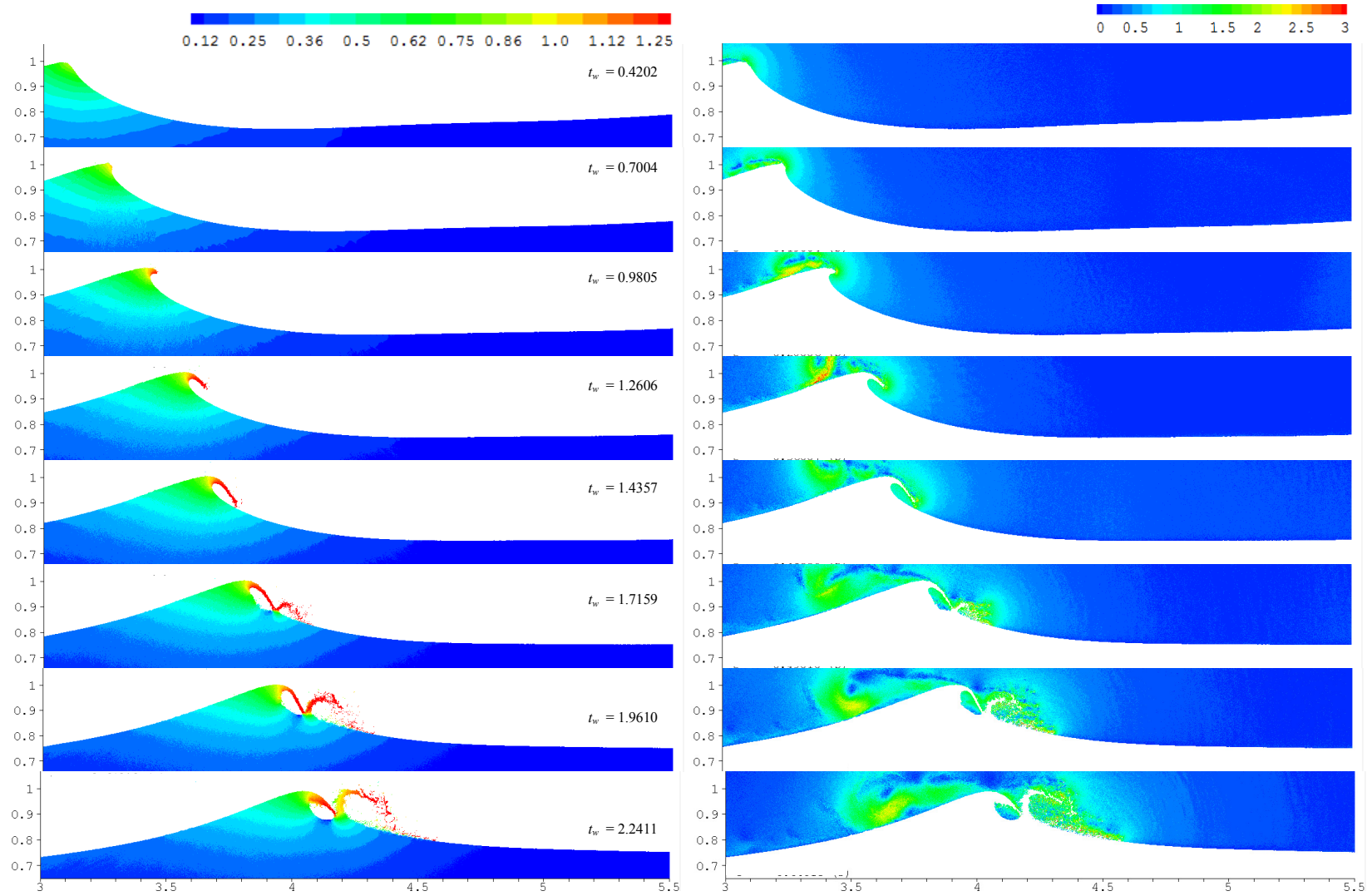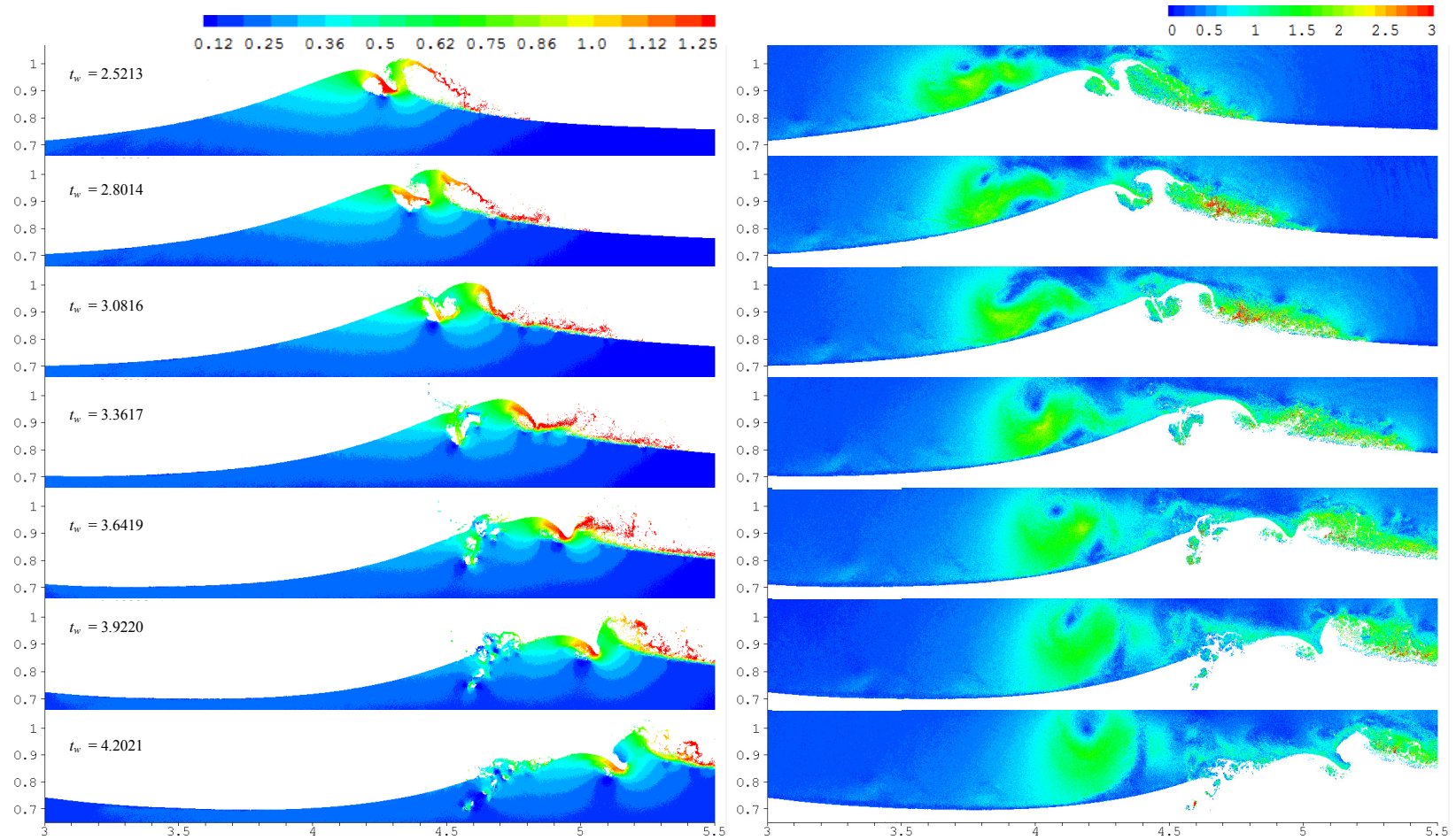
Figure 4.3. Absolute velocity (*V/C*) distribution in water (left) and air (right).

4.3   Characterization of wave breaking

The geometric parameters of the plunging wave at the inception of breaking are evaluated following the definition shown in Figure 4.4 These parameters are defined according to Bonmarin (1989). The breaking inception stage is determined by an observed visual criterion in the movie pictures. For a plunging breaker, breaking inception corresponds to the occurrence of a vertical crest front. In this study, a specific snapshot of simulated wave breaking when the crest starts to project forward is chosen. It corresponds to the snapshot of t_w = 0.7004 in Figure 4.2 and Figure 4.3.

The values of the geometric parameters of the simulated plunger are given in Table 4.1. Using these values, the breaking criterion, the degree of asymmetry and the angle ratios of the SPH-simulated breaking wave are calculated and provided in Table 4.2. These calculated values are compared with those published in Bonmarin (1989) (see Table 4.3 to Table 4.5).
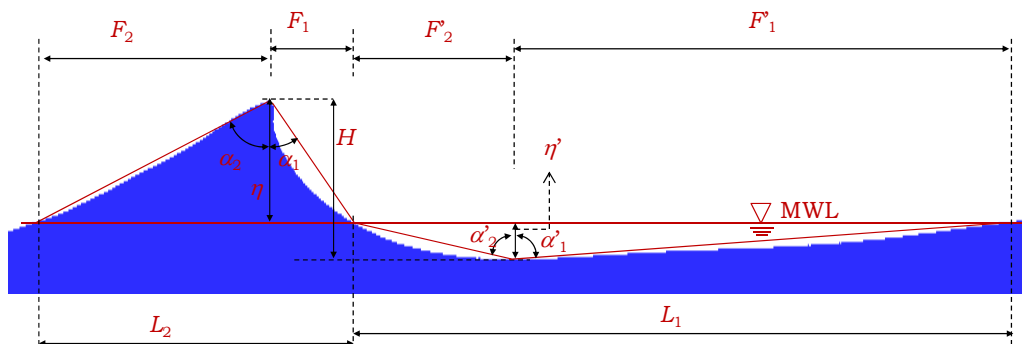
Figure 4.4. Definition of steep asymmetric wave parameters.

It was remarked in Bonmarin (1989) that the observed breakers did not correspond exactly to the theoretical definitions of plunging breakers or of spilling breakers. Therefore the term "typical breaker" was used. The observed breakers that displayed very distinctly all the characteristics of the theoretical plunging definition (Longuet-Higgins & Cokelet, 1978) were called "typical plunging breakers". A similar criterion was applied for the spilling breakers.

The breaking criterion is compared with Stokes limiting wave height, $\sigma = H/gT^2 = 0.027$. This approach has been used by different authors and results were summarized in Bonmarin (1989). The breaking criterion for this SPH-simulated plunging wave is 0.02. This is comparable with values of $0.02 - 0.022$ in Table 4.3. It is noted, however, that there is no clear criterion for wave breaking. For example, the wave breaking criterion of spilling wave in Ramberg & Griffin (1986) is 0.021 which is within the range of plunging waves. The overlap is possibly due to the difference in the estimation of parameters, especially the wave period. In our calculation, the wave period is calculated from the speed of the wave crest and wave length. By definition given in Bonmarin (1989) wave length was estimated from experimental photograph as shown in Figure 4.4, i.e. $L = L_1 + L_2$. However L_1 could vary due to different breaking conditions such as due to wave-wave interaction (L_1 could be longer), wave-current interaction or wave interference with obstacles (L_1 could be shorter). As a result, the calculated breaking wave criterion could be different for the same type of wave breaking but in different conditions. In this thesis, the wave length is taken as the distance from trough to trough at both sides of the wave crest (see Figure 4.5). As shown in Table 4.1, the wave length is 2.3 m, which is about twice of L_2. The wave crest's speed estimated from consecutive snapshots is about 2 m/s. Hence, the wave period is 1.15 s.
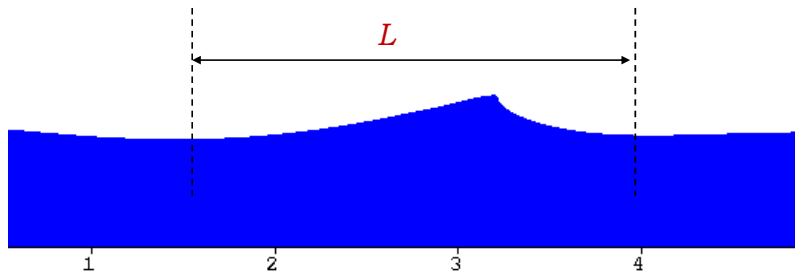
Figure 4.5. Wave length is measured from trough to trough at both sides of the wave crest.

The degrees of asymmetry computed in Table 4.3 are compared with published values shown in Table 4.4. The horizontal asymmetry factor is 0.769, which is very close to the mean value

of typical plunging wave (0.77). The vertical asymmetry factor is 2.714, which is larger than the mean value of typical plunging wave (2.14) but within the range of minimum value (0.97) and maximum value (3.09). The crest front steepness is 0.714, which again is larger than the mean value of typical plunging wave (0.61) but within the range of minimum value (0.31) and maximum value (0.85). Both the vertical asymmetry factor and crest front steepness are much closer to the maximum values. The crest rear steepness is 0.263 which is smaller than the mean value of typical plunging wave (0.29) but within the range of minimum value (0.24) and maximum value (0.33). It is noted from Table 4.4 that the mean values of first three degrees of asymmetry of the typical plunging is larger than those of general plunging. These degrees of asymmetry of the SPH-simulated breaking wave are even larger than the mean value of typical plunging, which indicate that the SPH-simulated breaking wave could be considered a strong plunging wave.

The published ratios of angles at crest and trough are given in Table 4.5. Going from spilling wave to typical plunging wave, ratios of angles reduce at crest and increase at trough. The ratio of angles of the SPH-simulated wave is 0.727 at crest (smaller than the value of typical plunging) and is 1.049 at trough (larger than the value of typical plunging). It is consistent with the typical of asymmetry discussed above and the SPH-simulated breaking wave maybe considered a strong plunging wave.

Table 4.1. Wave parameters of the simulated breaking wave.

η	0.2 m	F_2	0.76 m	α_2	66 deg	H	0.26 m
η'	0.06 m	F_1	0.28 m	α_1	48 deg	L (wave length)	2.3 m
L_2	1.1 m	F'_2	0.55 m	α'_2	81 deg	C (wave speed)	2 m/s
L_1	2.3 m	F'_1	1.82 m	α'_1	85 deg	V (particle speed)	2.1 m/s

Table 4.2. Breaking criterion, degree of asymmetry and angle ratios of the simulated breaking wave crest.

		Present study	Kway (2000)
Breaking criterion	$\sigma = H/gT^2$	0.02	
Wave steepness	$\gamma = H/L$	0.113	0.115
Horizontal asymmetry factor	$\mu = \eta/H$	0.769231	0.8
Vertical asymmetry factor	$\lambda = F_2/F_1$	2.714286	2.4
Crest front steepness	$\varepsilon = \eta/F_1$	0.714286	0.69
Crest rear steepness	$\delta = \eta/F_2$	0.263158	0.33
Crest steepness	$\gamma' = \eta/L$	0.08696	
Angle ratio at crest	α_1/α_2	0.727273	
Angle ratio at trough	α'_1/α'_2	1.049383	

Table 4.3. Breaking coefficients (Bonmarin, 1989).

	Plunging	Spilling	Unclassified
Stokes (theoretical limit)	-	0.027	-
Ochi and Tsai (1983)	0.020	-	-
Duncan (1983)	-	0.016	-
Ramberg and Griffin (1986)	0.022	0.021	-
Bonmarin (1989)	0.020	0.020	0.019
Koga (1986)	-	-	0.020

Table 4.4. Degrees of asymmetry of wave crest (Bonmarin, 1989).

	Breaker type	Minimum	Maximum	Mean
Horizontal asymmetry $\mu = \eta/H$	Typical plunging	0.65	0.93	0.77
	Plunging	0.62	0.93	0.76
	Spilling	0.59	0.91	0.75
	Typical spilling	0.60	0.80	0.69
Vertical asymmetry $\lambda = F_2/F_1$	Typical plunging	0.97	3.09	2.14
	Plunging	0.78	2.52	1.61
	Spilling	0.78	2.37	1.38
	Typical spilling	0.81	1.72	1.20
Crest front steepness $\varepsilon = \eta/F_1$	Typical plunging	0.31	0.85	0.61
	Plunging	0.29	0.77	0.47
	Spilling	0.24	0.68	0.41
	Typical spilling	0.31	0.51	0.38
Crest rear steepness $\delta = \eta/F_2$	Typical plunging	0.24	0.33	0.29
	Plunging	0.20	0.42	0.30
	Spilling	0.19	0.42	0.31
	Typical spilling	0.26	0.48	0.33

Table 4.5. Ratios of angles at crest and trough (Bonmarin, 1989).

Breaker type	α_1/α_2 (crest)	α'_1/α'_2 (trough)
Typical plunging	0.80	1.02
Plunging	0.89	1.01
Spilling	0.93	1.01
Typical spilling	0.97	0.99

4.4   Kinematics of the plunging jet at the initial stage of wave breaking

At the initial stage of wave plunging, the wave crest is steepened and a jet starts to eject from front face near the top of the wave crest and projects forward (as shown in Figure 4.6). The velocity magnitude of the water particles at the wave crest at $t_w = 0.56$ (just before the steepening) is less than $1C$. Velocities of some particles reach $1C$ at time $t_w = 0.63$ and exceed $1C$ at time $t_w = 0.7$. A vertical front face of the wave crest is seen. The velocity magnitude increases and a jet is projecting forward could be observed at $t_w = 0.77$. The velocity magnitude reduces toward the water in the front. Water in this region is also moving forward but with a velocity magnitude less than $1C$.

Snapshots of the velocity field relative to the wave crest during the developments of the plunging are shown in Figure 4.7. The relative velocity is calculated by subtracting the wave crest speed from the horizontal component of the absolute velocity. Prior to the wave plunging, water particles near the wave crest are moving backward relative to the wave crest. When the crest is steepening, an upward movement of water relative to the wave crest is observed. Just prior to the jet formation, the upward movement of water diverges (relative to the wave speed) at the top of the wave crest. A part of the upward flowing water moves forward, creating the plunging jet. The trajectories of the water particles relative to the wave crest suggest a clockwise circulation following the plunging jet and the front face of the wave. The direction of the relative velocity is parallel to the direction of the plunging jet, suggesting that the plunging jet is mainly generated by the circular movement of the water at the front face of the steepening wave crest.

Acceleration of the water particles on the interface are shown in Figure 4.8. At the top of the wave crest, the acceleration is close to zero. Water acceleration at the tip of the plunging jet points downward with magnitude of about $1g$, suggesting that the motion of the tip is close to

free fall. At the curved part of the inner face of the plunging jet, the acceleration is highest with magnitude reaching 4g (see Figure 4.8k). This may be attributed to the centrifugal force acting on the circulating water mass in the wave crest and the plunging jet. Further away from the plunging crest, the acceleration reduces. Figure 4.8 also shows some irregularities under the wave crest. In particular, neighbouring particles appear to exhibit contrasting properties (e.g. mixture of high acceleration and low acceleration particles). This is mainly due to the spurious oscillations associated with SPH, especially for higher order kernels. It is noted, however, that smoothing every 40 to 100 time steps would be able to contain the spurious oscillations and maintain stability.

The distribution of normalized pressure in the wave crest and the plunging jet is shown in Figure 4.9. Away from the plunging jet, pressure is regular and almost follows non-breaking wave distribution, i.e. near zero at the water surface and increase with distance from the water surface. At the curved part of the inner face of the plunging jet, pressure increase faster with distance from surface due to the presence of high water acceleration. In the plunging jet, pressure is close to zero which is due to the near-free-fall of the plunging jet.
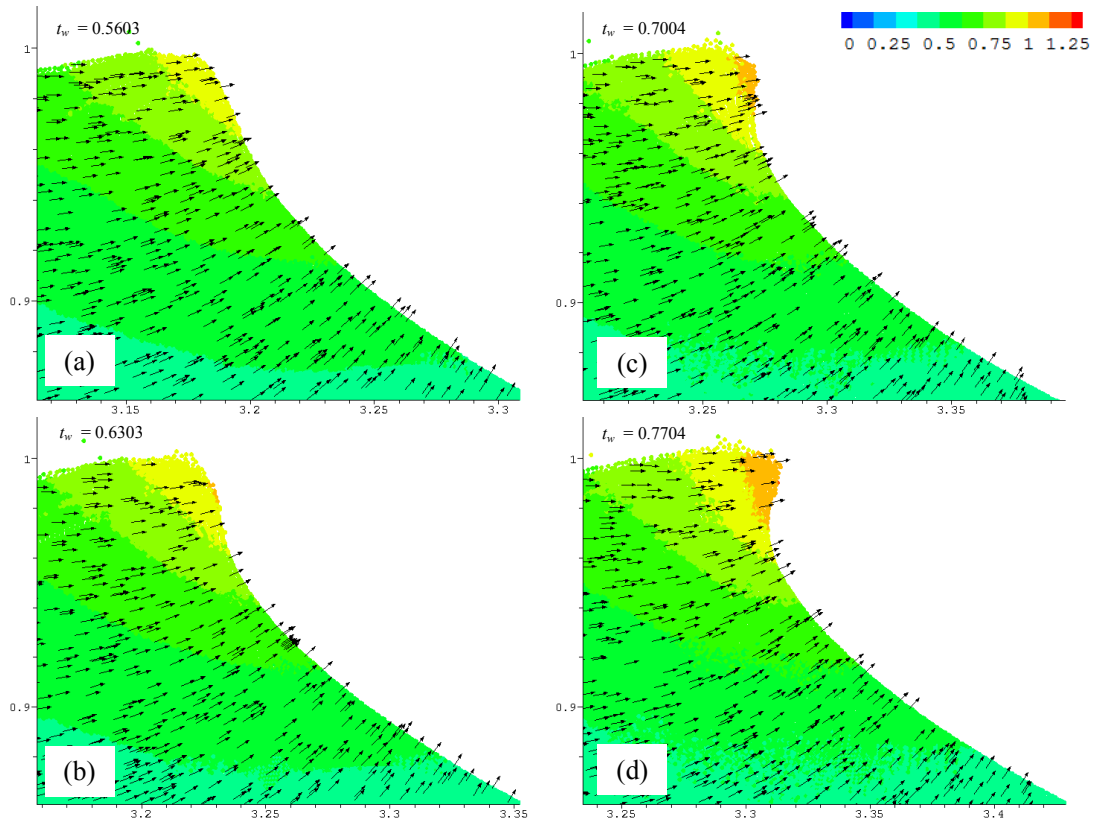
Figure 4.6. Velocities of water particles in the crest when the crest is steepening and the jet starts ejecting. Color code represents the absolute velocity (*V*/*C*), arrows indicate directions.
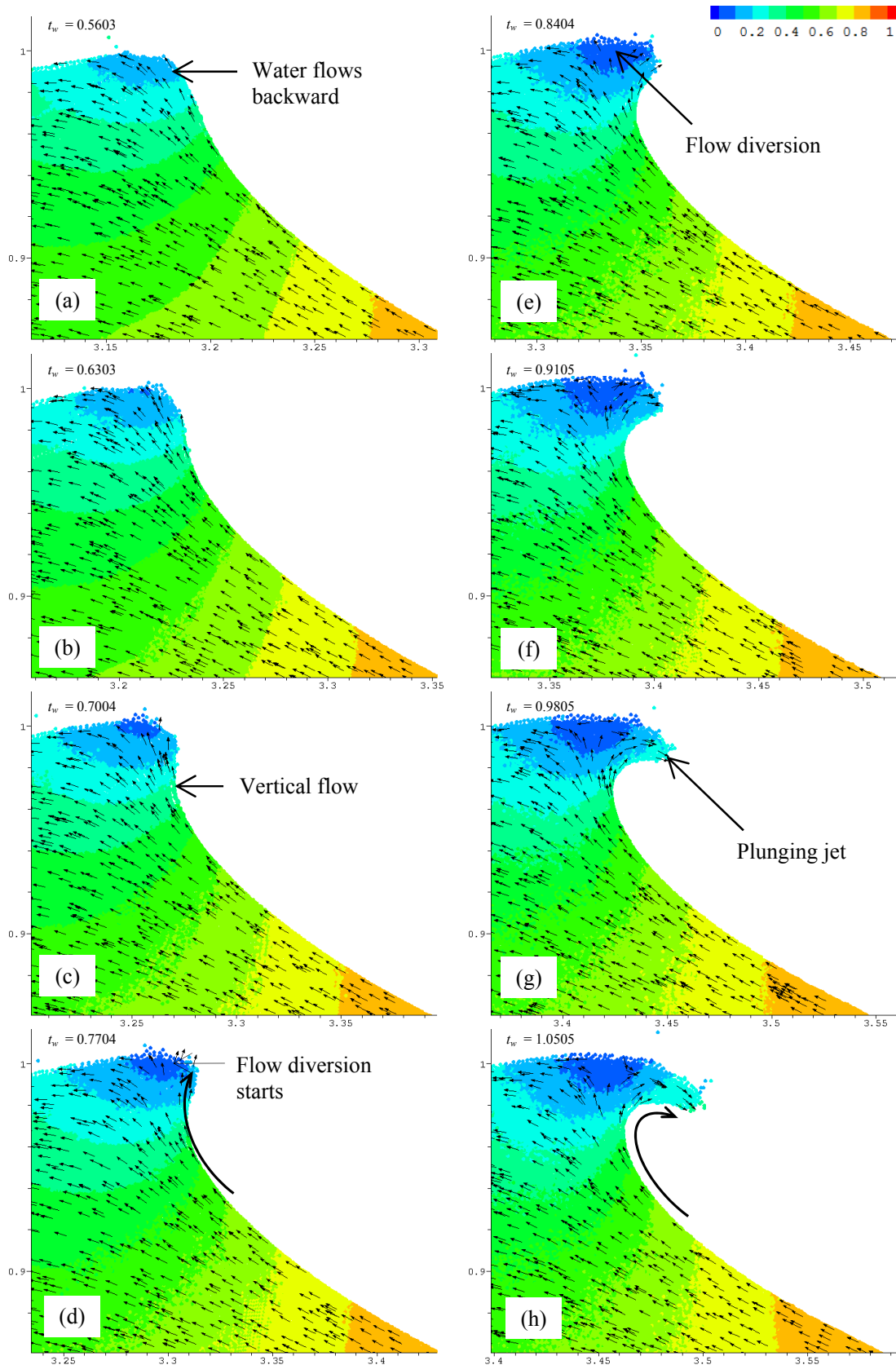
Figure 4.7. Plunging jet development and the relative velocities of the water particles (V/C-1) in the crest and plunging jet in prior to impingement. Color code represents magnitude of the relative velocity, small arrows indicate directions.
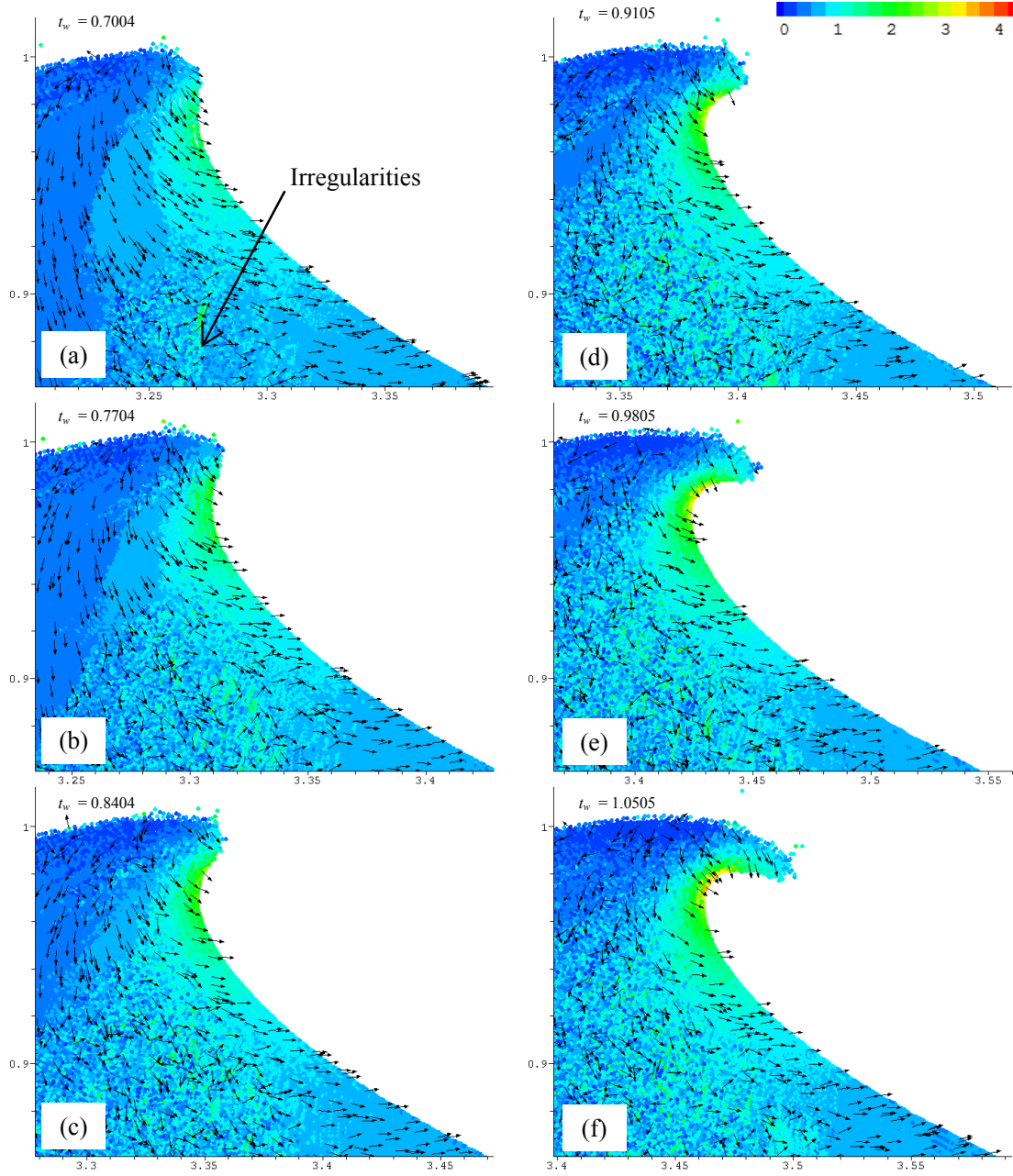
(continued on next page)
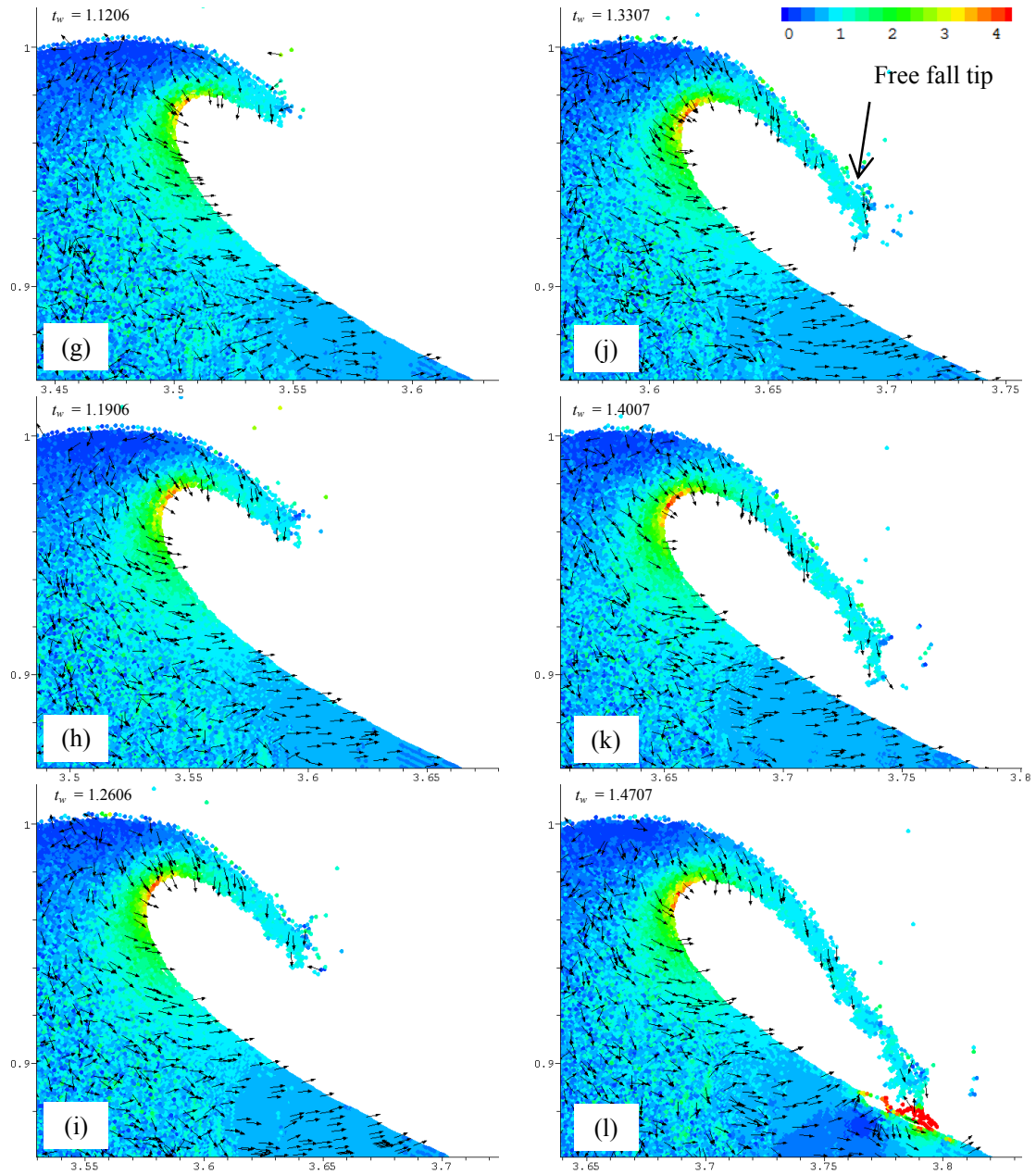
Figure 4.8. Acceleration (a/g) of the water in the wave crest and plunging jet in prior to impingement. Color code represents magnitude of the acceleration, arrows indicate directions.
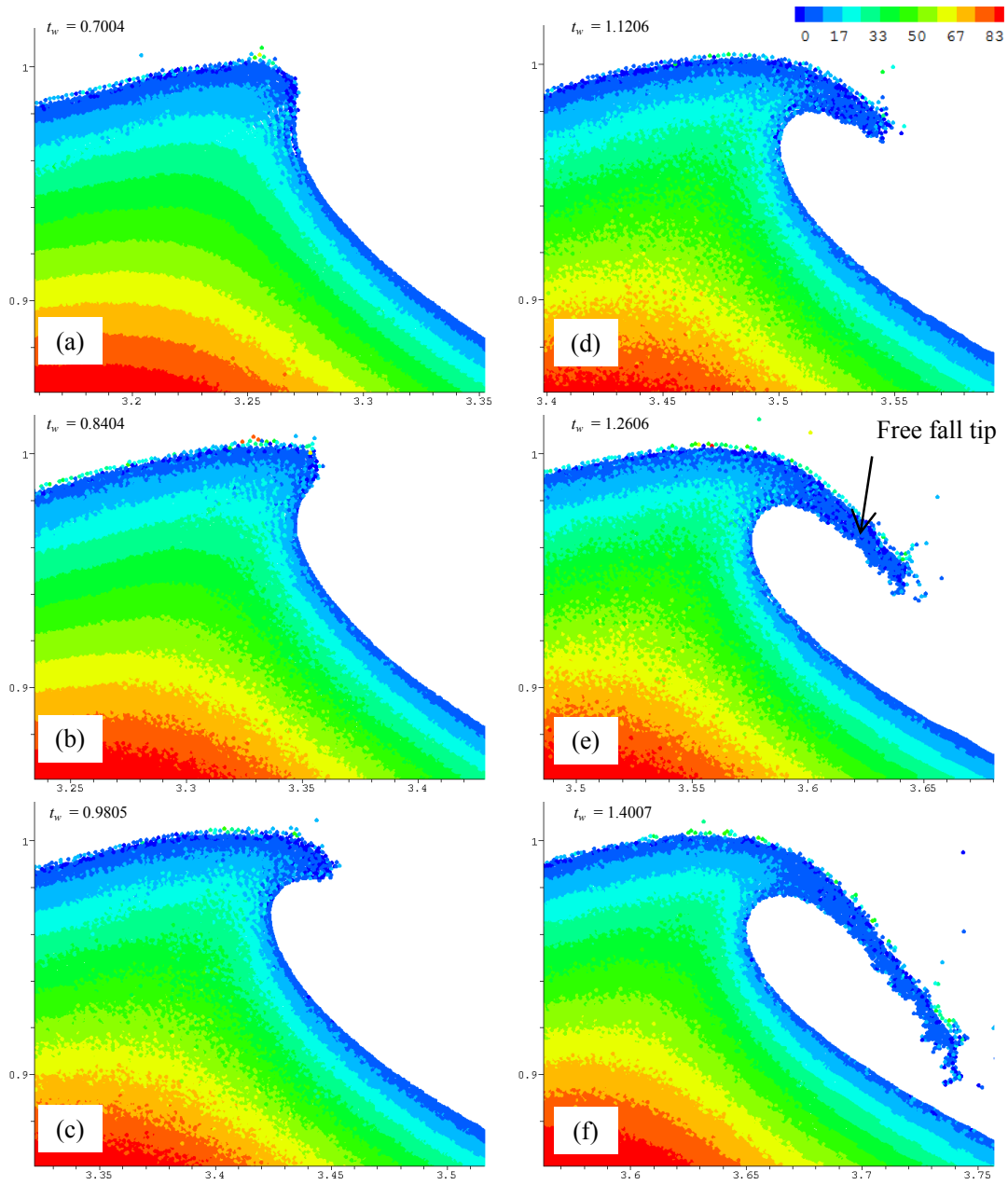
Figure 4.9. Pressure distribution ($p/\rho_0 gD$) in the wave crest and plunging jet in prior to impingement.

4.5   Dynamics of wave breaking

Three key features of the plunging wave during breaking are: (i) formation of the air tube and evolution of the water body surrounding the air tube; (ii), formation of the vertical jet and its interaction with the plunging jet; and (iii) collapse of entrapped air tube and vertical sprays of water. These features were observed and some were described in the past researches (Miller, 1976; Peregrine, 1983; Bonmarin, 1989; Kway, 2000).

Details of the simulated air entrapment process corresponding to Kway (2000) are presented in Figure 4.10 to Figure 4.25. In these figures, only water phase is plotted. A color code is used to demarcate values of the velocity, pressure or band of water particles, permitting a better understanding of the plunging process.

Figure 4.10 shows the plunging jet entrapping a tube of air just prior to impingement back into the wave front. Initially, the air tube has the shape of an inclined and elongated ellipse (dash red curves in Figure 4.11). During the early stages, the surface of the tube is relative smooth except some disturbances near the contact region (as shown in the dash circles in Figure 4.11). Experiment studies by Kway (2000) showed that the instabilities start to set in at this stage and the surface of the tube becomes wavy. The series of photographs in Figure 1.5 suggests that disturbances near the contact area roll up and eventually spread over the tube. It is now clearly seen in Figure 4.11 that the disturbances originate from the collision of the plunging tip and the base (indicated by the dashed circles). The disturbances then are carried with the circulation of the water and quickly spread over the inner surface of the tube as shown in the series of snapshots in Figure 4.12.
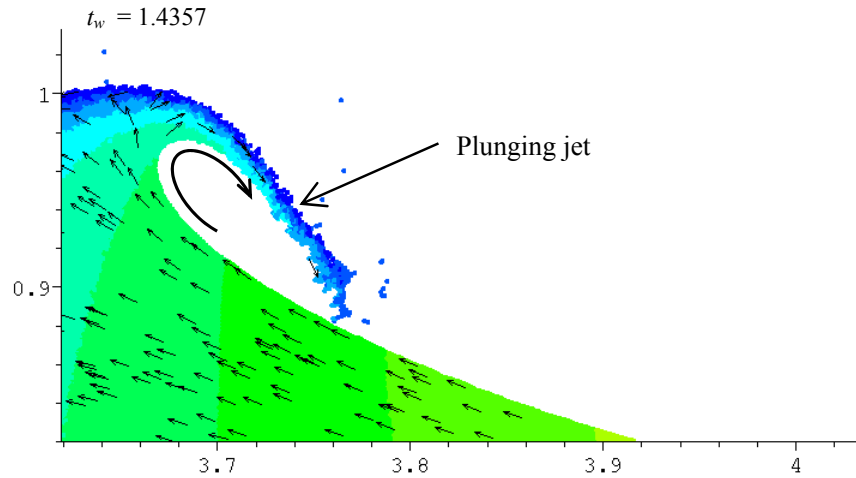
Figure 4.10. Water surface is initially smooth at the front before the impingement. Color code represents the particle id, small arrows denote direction of relative velocity.
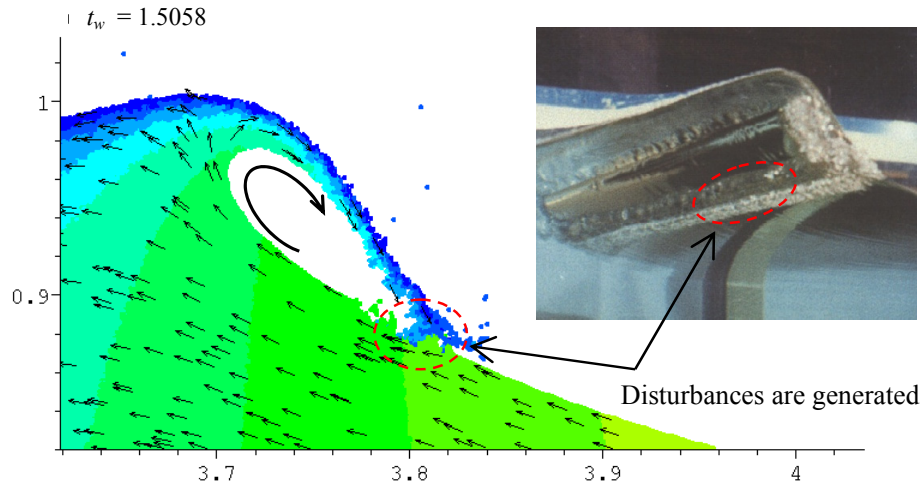
Figure 4.11. Disturbances appear at the contact area just after the plunging jet impingement onto the water front. Color code represents the particle id, small arrows denote direction of relative velocity. Photographs are observations (Kway, 2000).

It is clear from Figure 4.12 that the tube changes its shape when rolling forward. In Figure 4.12a, the tube has a shape of long, thin ellipse. In Figure 4.12b, the tube is thicker and shorter. In Figure 4.12c, a more rounded tube is observed. These results are consistent with the observations in the experiments by Kway (2000), which are displayed next to the numerical results in Figure 4.12a-c.

From the numerical results, it is also clear that the plunging jet does not penetrate deeply into the water column, but is bifurcated on impingement. The inner part is bent backward and follows the tube surface's rolling motion and the disturbances (shown in Figure 4.12 by a layer of blue particles). The outer part is projected forward on re-bounce. Due to the inclined impingement, water from the wave front (shown as green and yellow particles) is pushed forward, en-massed with the water particles from the plunging jet to form a splash-up. The process is illustrated in Figure 4.12a. The plunging jet continuously impinges on the water front, peeling off the top layer of the water front to form a big vertical jet as shown in Figure 4.12c. It can be seen from the arrows in the water body, which denote velocity directions, that water flow relative to the wave crest is bifurcated at the top of the wave crest and at the base of the vertical jet where it joins with the plunging jet. Two clockwise circulations, indicated by the two bold black arrows in Figure 4.12c, are observed in the plunging jet and the vertical jet. The closed circulation in the wave crest and the plunging jet provide the continuity for the rolling motion of the air tube. This closed circulation of the surrounding water provides the centrifugal force while the entrapped air provides pressure support to the surrounding water body. These two factors perhaps are the main reason for the tube to persist while rolling forwards with the wave.

While the tube is rolling, the entrapped air goes through the compression and decompression. The changes in the shape of air tube and the pressure of the entrapped air can be seen in Figure 4.13. In Figure 4.13a,b the entrapped air is at low pressure. The air pressure then increases (as shown in Figure 4.13c,d) and decreases (Figure 4.13e) and increases again (Figure 4.13f).
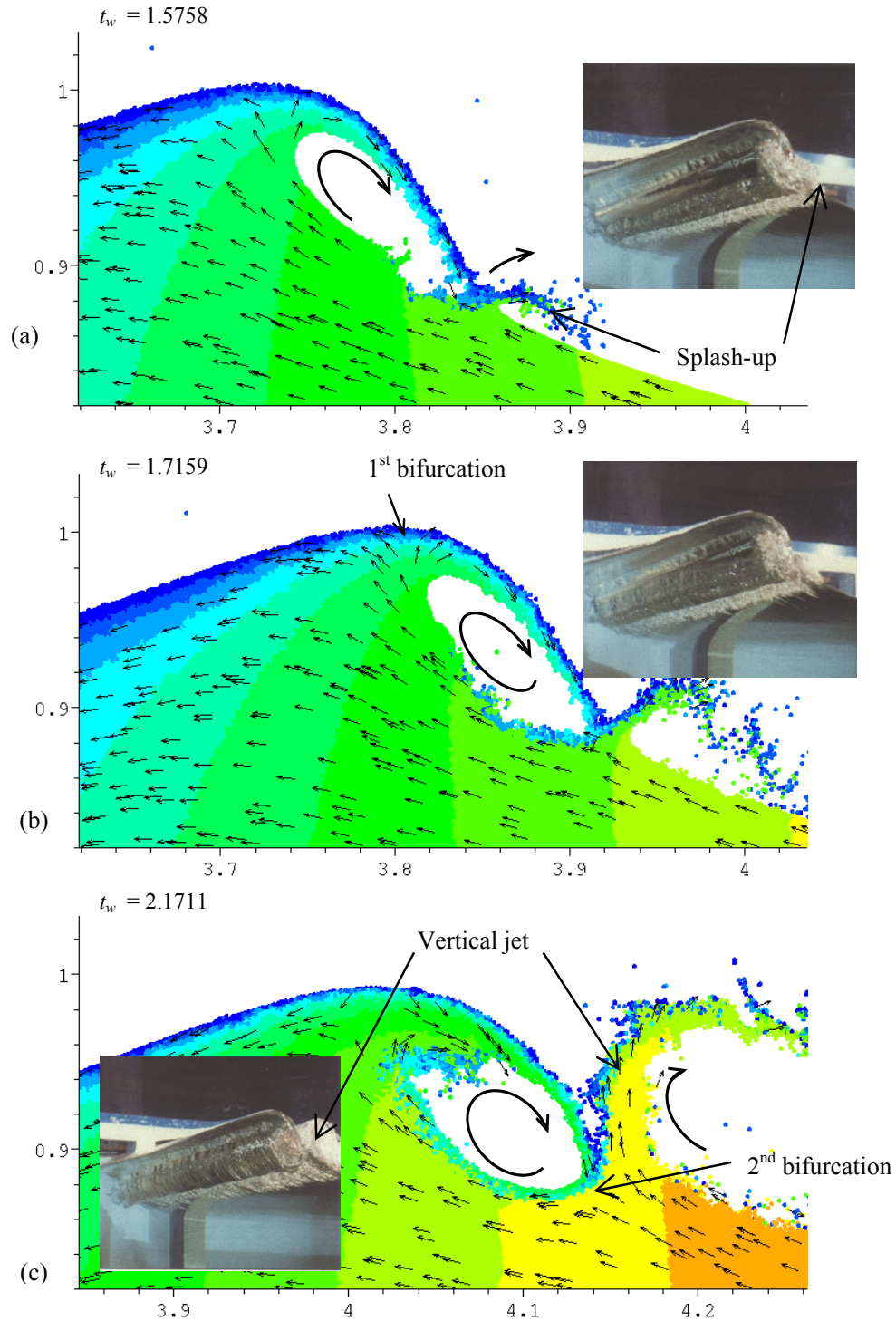
Figure 4.12. The splash-up and vertical jet are formed composing of water from the plunging jet (blue) and the base (yellow). Part of water from the plunging jet is carried with the rolling tube to spread over the whole surface of the tube. Color code represents the particle id, small arrows denote direction of relative velocity. Photographs are observations (Kway, 2000).
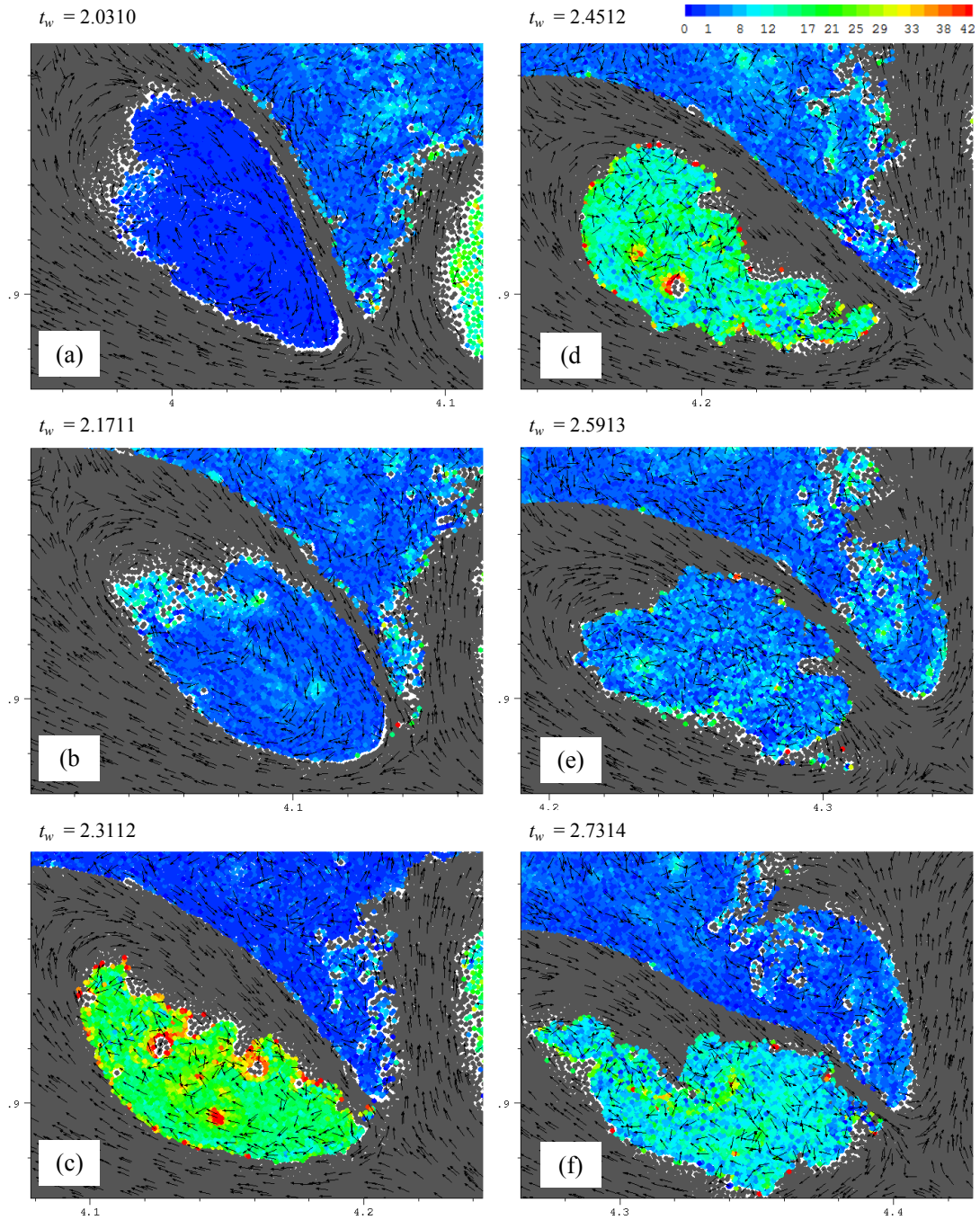
Figure 4.13. The air tube change its shape and the entrapped air is compressed (c,d), decompressed (e) and then compressed again (f) while the tube rolling and moving forwards. Color code represents air pressure ($p/\rho_0 gD$), arrows denote directions of the relative velocities.

As the wave plunging progresses, the upper part of the surrounding water becomes thinner and weakens, and thus is not able to hold the compressed air inside. At some points, the plunging jet is broken and a part of the entrapped air quickly squirts out through the gap. This process can be observed in Figure 4.14 (color codes are air pressure in the left column and relative air velocity in the right column). The gap is opened near the base of the vertical jet where it joins with the plunging jet. The water layer is thinnest at this area (see Figure 4.14b). The velocity of the jet is as large as $3C$ as shown in Figure 4.14c. Entrapped air is compressed before the tube is broken. In Figure 4.14c, it can be seen that the air jet squirts out through the narrow gap at a high pressure. After the entrapped being released, the air tube's volume and pressure reduce.
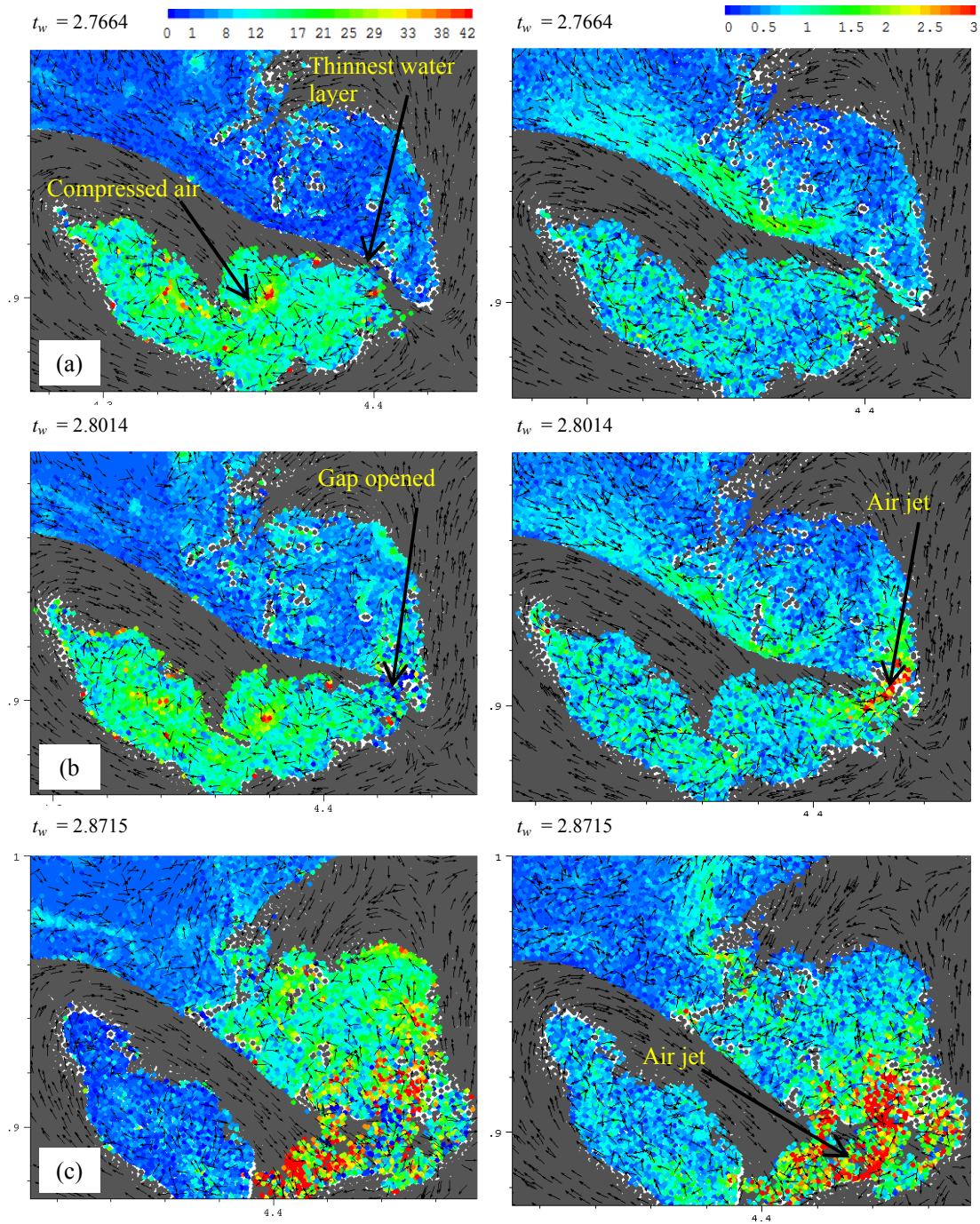
Figure 4.14. Close view of the air squirted out from left pocket to the right through an opened gap on the plunging jet. Color codes are air pressure ($p/\rho_0 gD$) (left column) and relative velocity (V/C - 1) (right column). Arrows denote velocity direction.

As the plunging jet continues impinging on water front, the initial vertical jet receives more water from the plunging jet and the wave front to grow to a large and powerful vertical jet. The vertical jet comprises of water mainly from the water front and, to a smaller extent, from the plunging jet. The vertical jet can rise as high as the original wave crest (see see Figure 4.15). It also can be seen in photographs taken by Kway (2000) and **Error! Reference source not found.** (description by Bonmarin, 1989) that the vertical jet can rise higher than the wave crest. It is because a large amount of kinetic energy carried by the plunger is transferred to potential energy in the vertical jet. When the vertical jet attains its maximum height, it starts to split backward and forward. The development and collapse of the vertical jet are shown in sequences in Figure 4.15 to Figure 4.19. The small arrows these figures indicate the movement of the water in the wave crest, vertical jet and in the wave front. A third bifurcation of the water flow is seen at the top of the vertical jet where it slits into backward and forward flows. The back flow formed a third water circulation. As indicated by the bold arrows in Figure 4.15c, the 3rd circulation is counter clockwise and lies in between the previous two clockwise circulations.

Figure 4.15 and Figure 4.16 show how the backward diversion of the vertical jet closes up with the forward moving plunging jet to entrap a second air pocket. The entrapping air is pressurized because of the quick fall of the backward flow of the vertical jet on the plunging jet and the air jet squirting out from the original entrapped air pocket on the left. As a result, air quickly escapes through the gap between the backward flow of the vertical jet and the plunging jet. As shown in the velocity plots in Figure 4.16, the air squirted out creates a strong vertical jet with a speed exceeding $3C$.

An unexplained feature of the plunging process, observed in Kway (2000), is the vertical sprays (see Figure 1.6). Figure 4.16 to Figure 4.18 depict how the sprays could have been formed. Figure 4.16 shows a speed air jet squirted out through the gap between the backward

flow of the vertical jet and the plunging jet. In Figure 4.17, it can be seen that the sprays are shooting upward, comprising mainly of particles having blue color. The blue particles were seen at the tip of the back flow portion of the vertical jet in Figure 4.15b while the plunging jet has mainly green and cyan particles. In a close view of the sprays shown in Figure 4.18 (the color code is the absolute velocity magnitude of water particles and the arrows denote the velocity directions), the particles at the tip of the back flow portion of the vertical jet probably slightly impacted on the plunging jet and bounced up when the air is squirting out (t_w = 2.8715 – 2.9765). Although the figure shows an incline shape of the sprays, the arrows of the actual velocity show that particles are indeed shooting upward. The velocities of the particles are in the direction of the air jet at the gap. The existence of the high speed air jet (as shown in Figure 4.16) and the particle movement following the jet indicate that the air jet is the main cause for the formation of the upward spray. The velocity magnitudes of the sprays are around $0.2C – 0.4C$.

At the later stages, t_w = 3.0115 – 3.1516, velocities of water particles of near the wave crest point forward and having higher magnitude (~$0.6C$), suggesting that these additional sprays are mainly caused by the collision of the plunging jet and the back flow portion of the vertical jet.
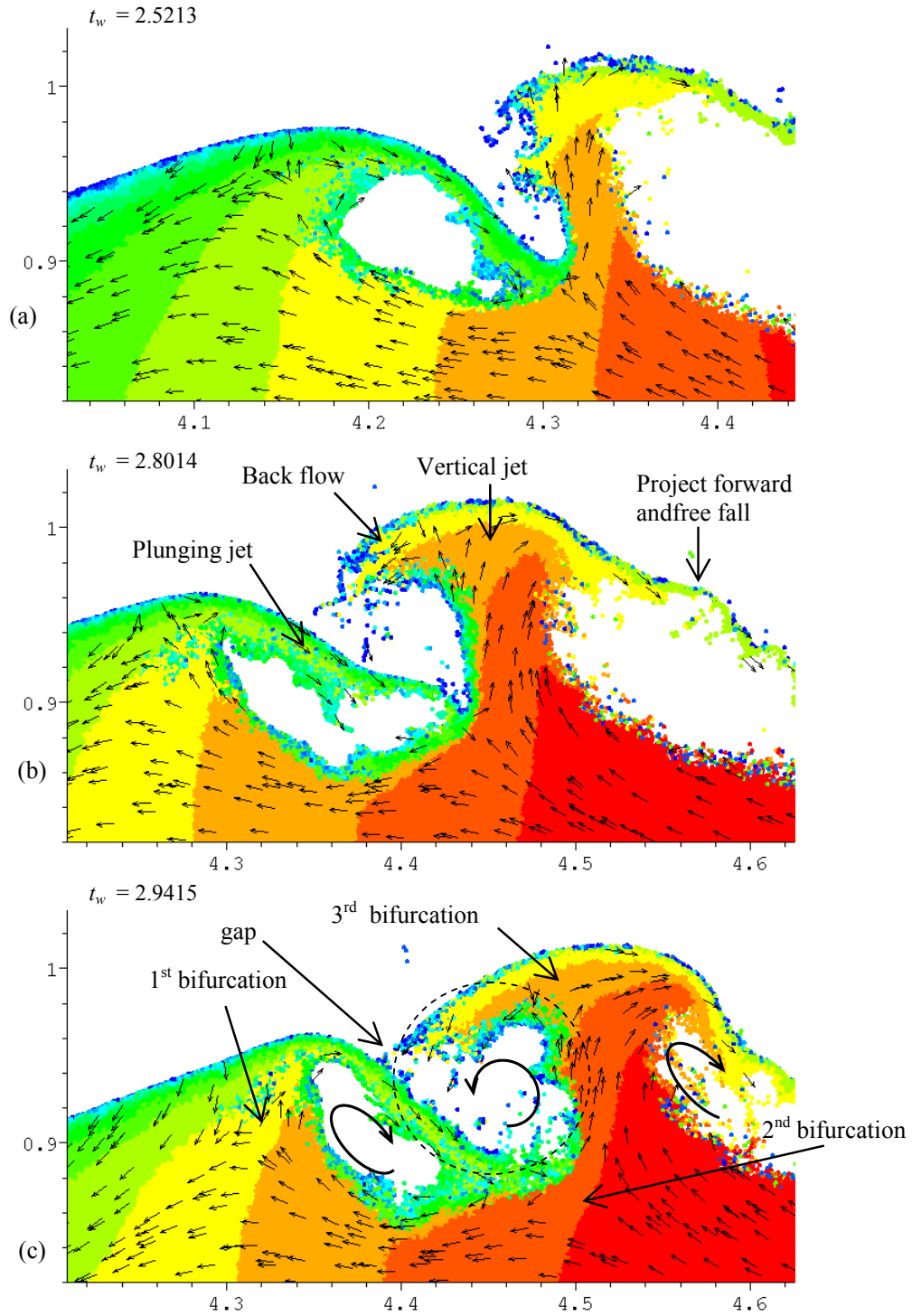
Figure 4.15. Impingement of the back flow of the vertical jet onto the plunging jet closing up an additional air pocket (circled). The rear part of the vertical jet composes of water droplets. Color code represents the particle id, small arrows denote direction of relative velocity.
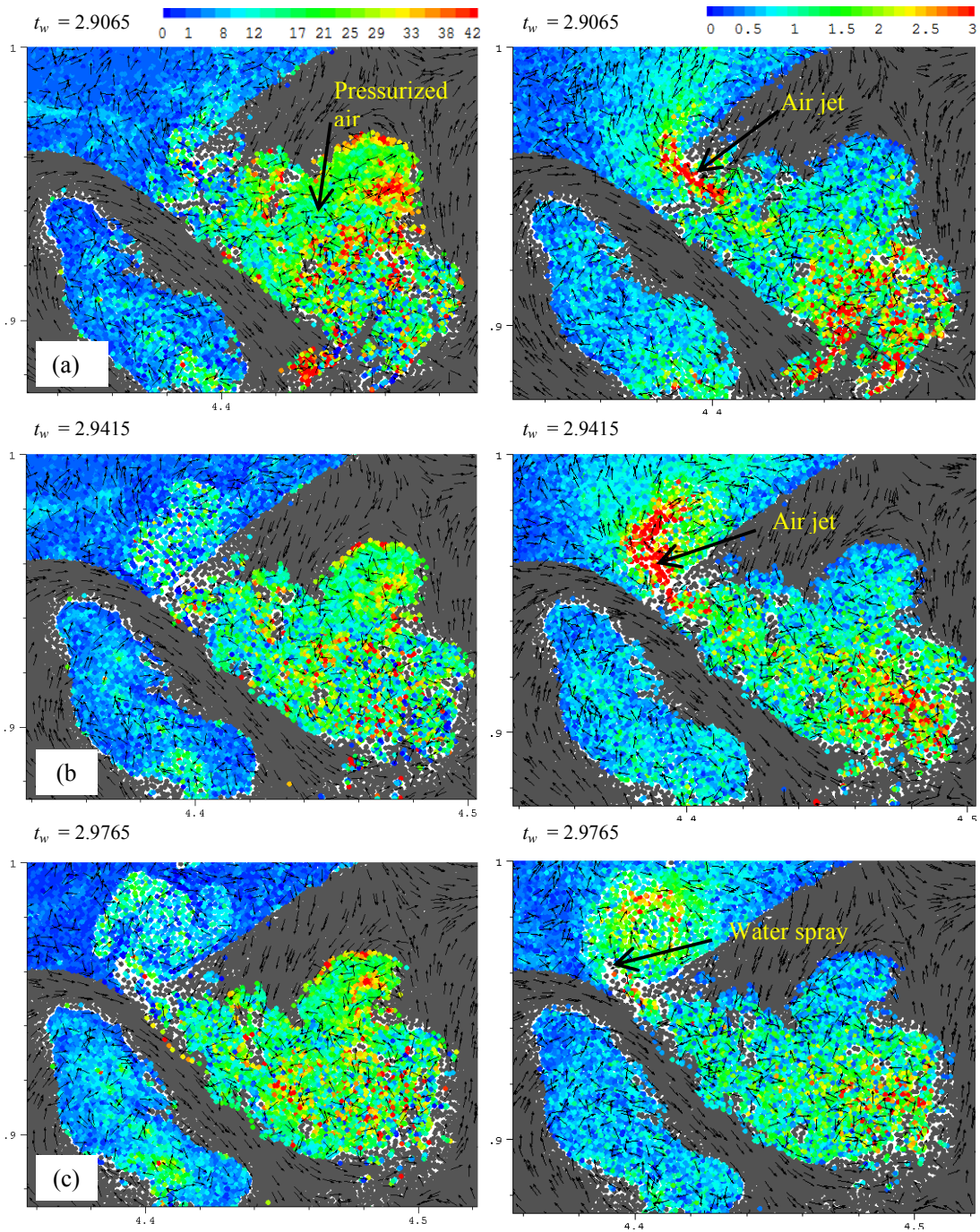
Figure 4.16. Close view of the air squirted out from the right pocket through a gap between the back flow portion of the vertical jet and the plunging jet. Color codes are air pressure ($p/\rho_0 gD$) (left column) and relative velocity of air (V/C - 1) (right column). Arrows denote velocity direction.
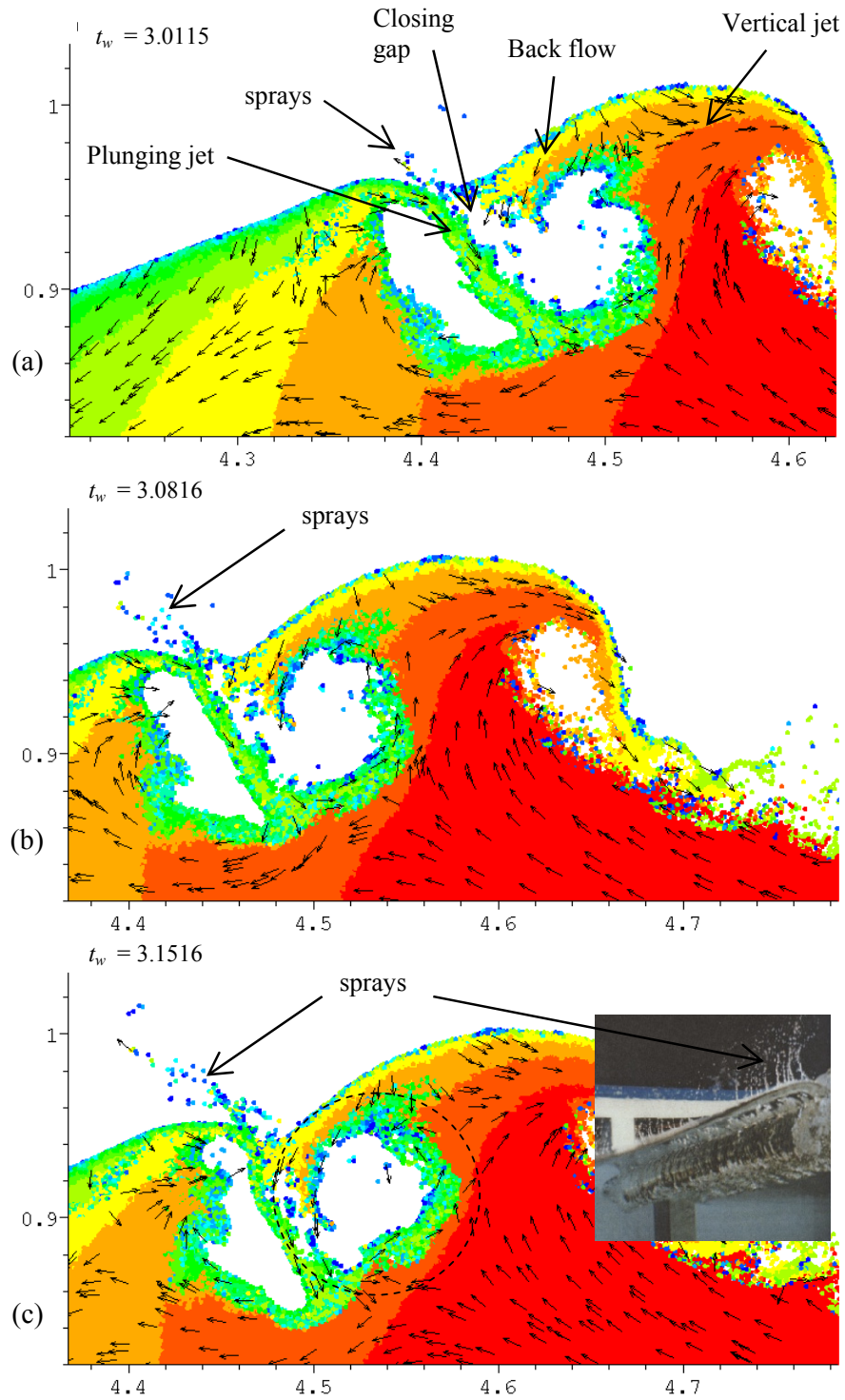
Figure 4.17. Water particles from the back flow portion of the vertical jet and surface of the plunging jet shooting up, creating sprays. An additional air pocket is formed (circled). Color code represents the particle id, arrows denote direction of relative velocity.
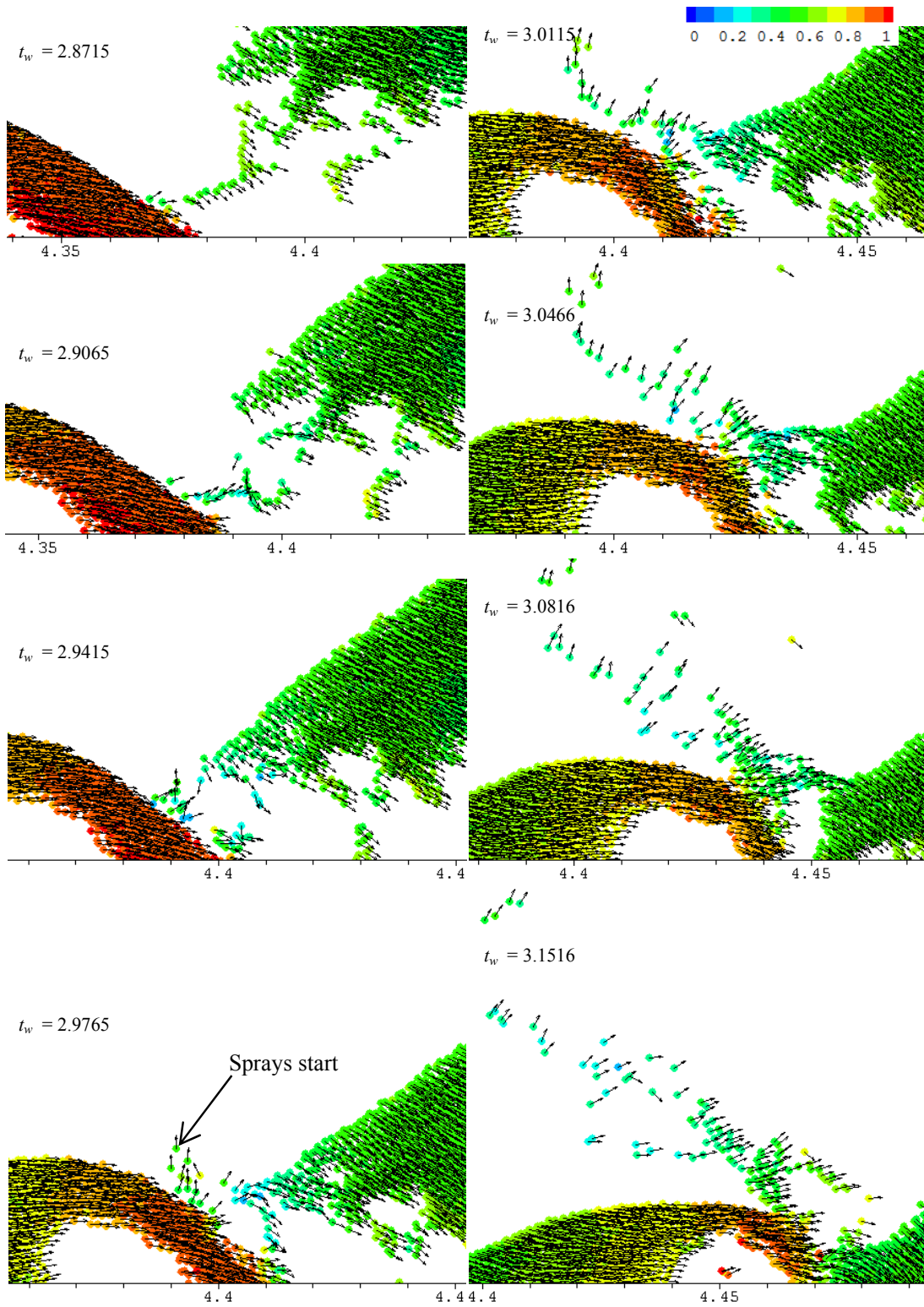
Figure 4.18. Close views of the vertical sprays of water. Color code and arrows represent the absolute velocities of water particles (*V/C*).

When back flow of the vertical jet impinges on the plunging jet, water is strongly splashed creating violent fragmentation of water above water surface (see Figure 4.19b-c). It can also be seen in the photograph in Figure 4.19c, larger water splashing is observed near the wave crest compared to the photograph in Figure 4.17c, suggesting that this water splash is due to the collision of back flow of the vertical jet and the plunging jet. Close views of this collision are shown in Figure 4.20. The water splash is pushed forward with a speed of $0.5C$ faster than the speed of the wave crest. It can also be seen from the figure that water particles from the previous sprays are falling down behind the wave crest.

It can be seen in Figure 4.15c that the original air pocket reduces its volume because a part of air has escaped. As shown in Figure 4.19a, a second air pocket having an equivalent size is created when the back flow of the vertical jet has impinged on the plunging jet. The two air pockets rotate in opposite directions and then break into smaller bubbles in the water column.
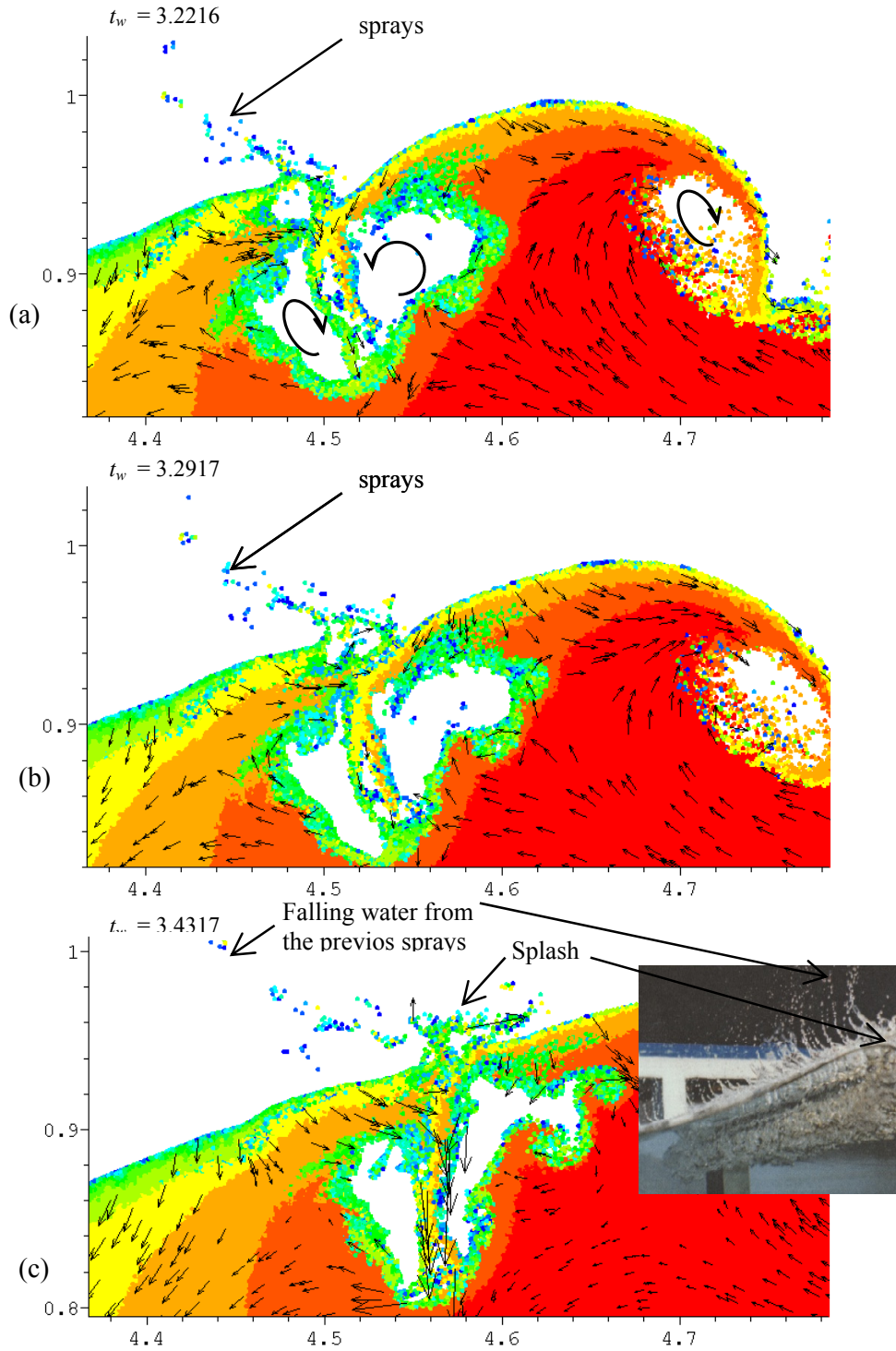
Figure 4.19. Water splashes near the wave crest due to the collision of the back flow of the vertical jet onto the plunging jet. Color code represents the particle id, arrows denote direction of relative velocity.
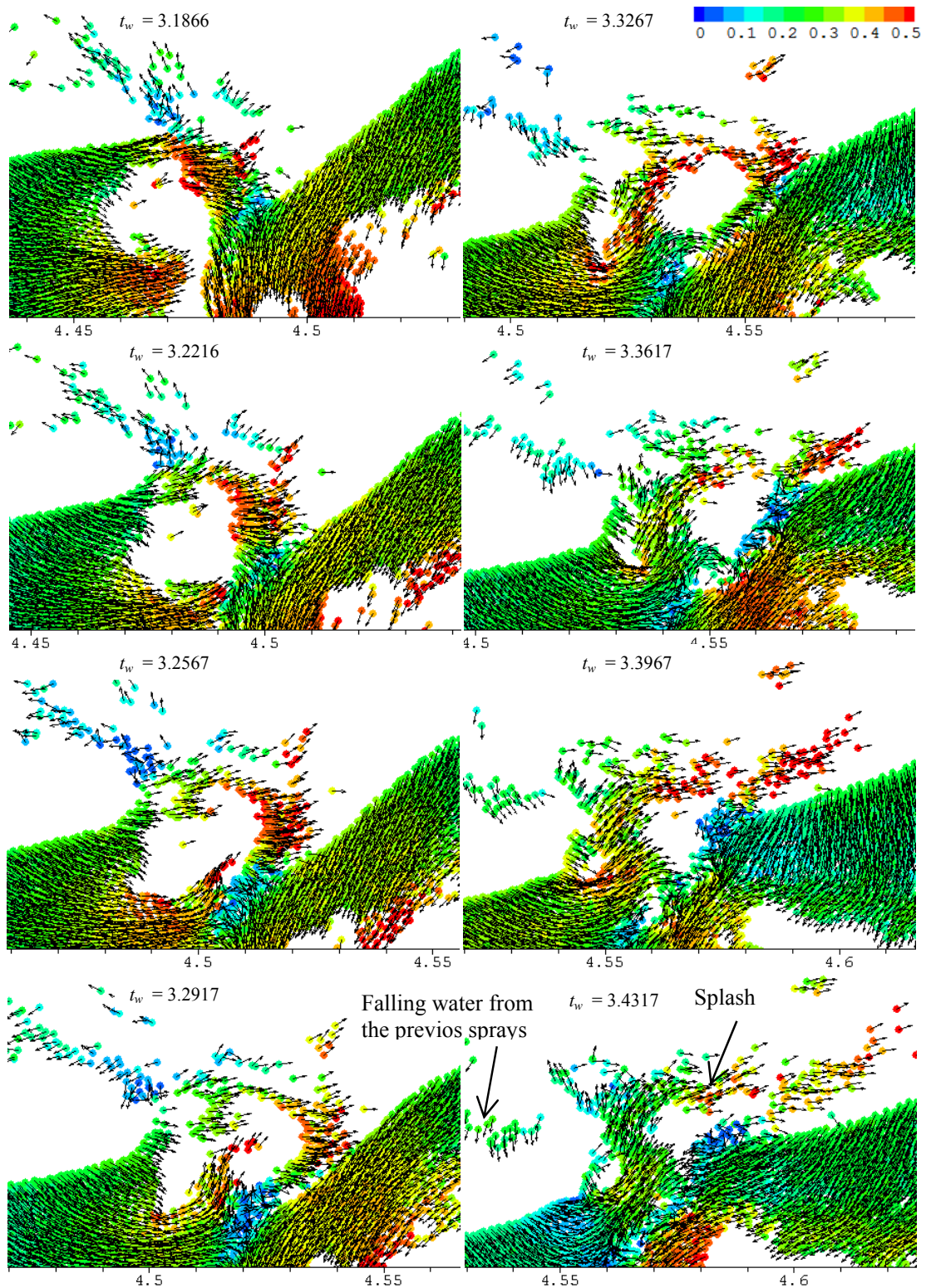
Figure 4.20. Close views of the collision of the vertical jet onto the plunging jet, breaking the water surface, creates violent water fragmentation at the surface. Color code and arrows represent relative velocities of water particles (*V/C* - 1).

Details of the pressure distributions in the plunging jet, in the vertical jet and under wave crest before and during the collapse of the vertical jet are shown in Figure 4.21 - Figure 4.23. Water pressures are low in the plunging jet and in the vertical jet. High pressures are observed at impact areas such as at the impingement of the plunging jet onto the water front and the collision of the vertical jet on the plunging jet (Figure 4.22c). The spinning vortices in the water column also increase the pressure of the surrounding water (see Figure 4.23).

The vorticity and subgrid turbulent kinematic eddy viscosity inside water are provided in Figure 4.24 and Figure 4.25. We can see large vorticity and turbulence intensity are located at the breaking region. Large values appear at some spotted areas where velocity gradient is large such as the impinging areas, counter-spinning vortices. The spinning structures of the vortices generate high turbulence and carry it deeply into the water column. The more vortices are generated, the more energy will be dissipated through turbulence. Except for the vortex-generated part being brought down, turbulent mixing is mainly confined to near the water surface.
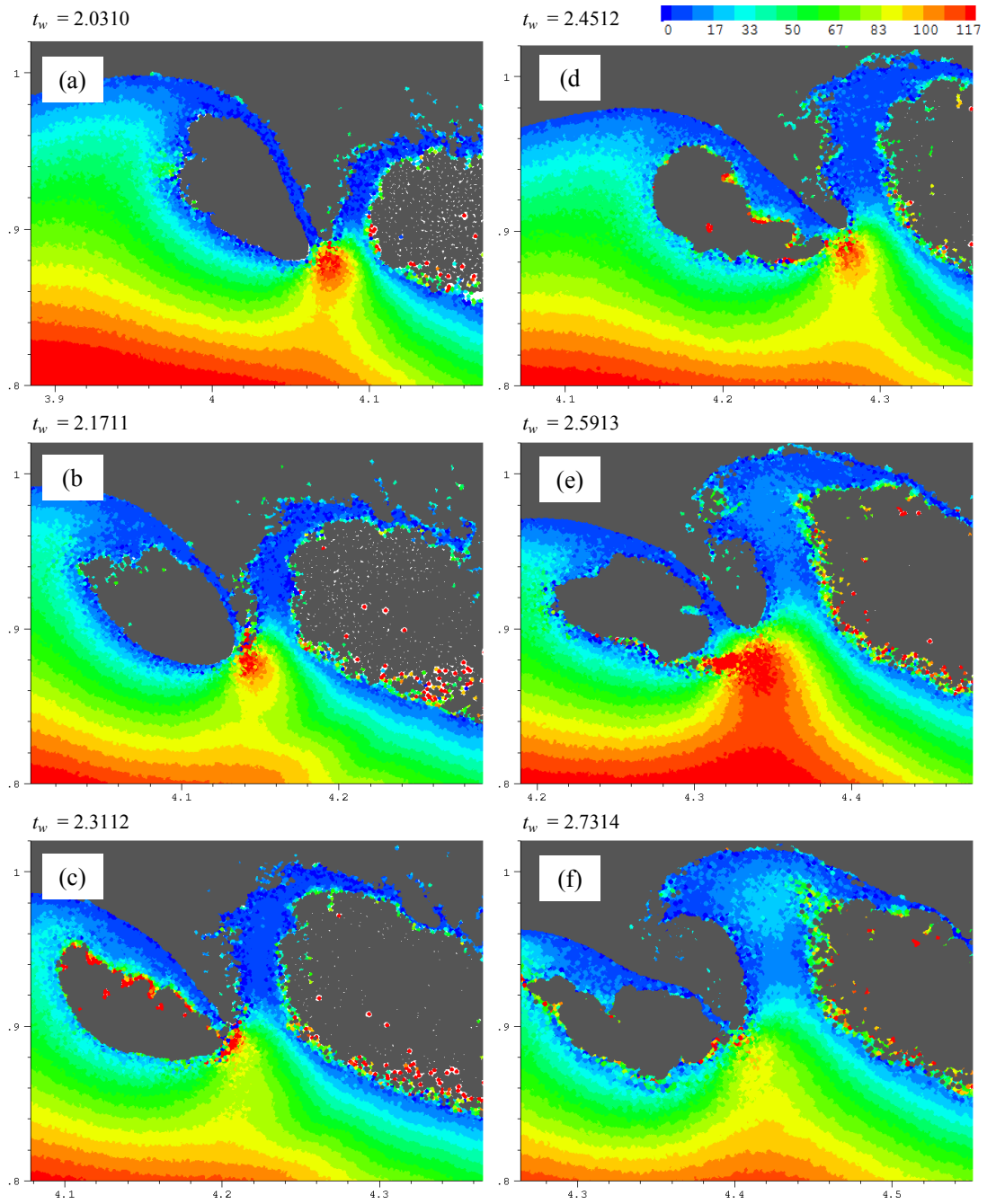
Figure 4.21. Pressure distribution ($p/\rho_0 gD$) in the plunging jet, in the vertical jet and under wave crest before the vertical jet collapse.
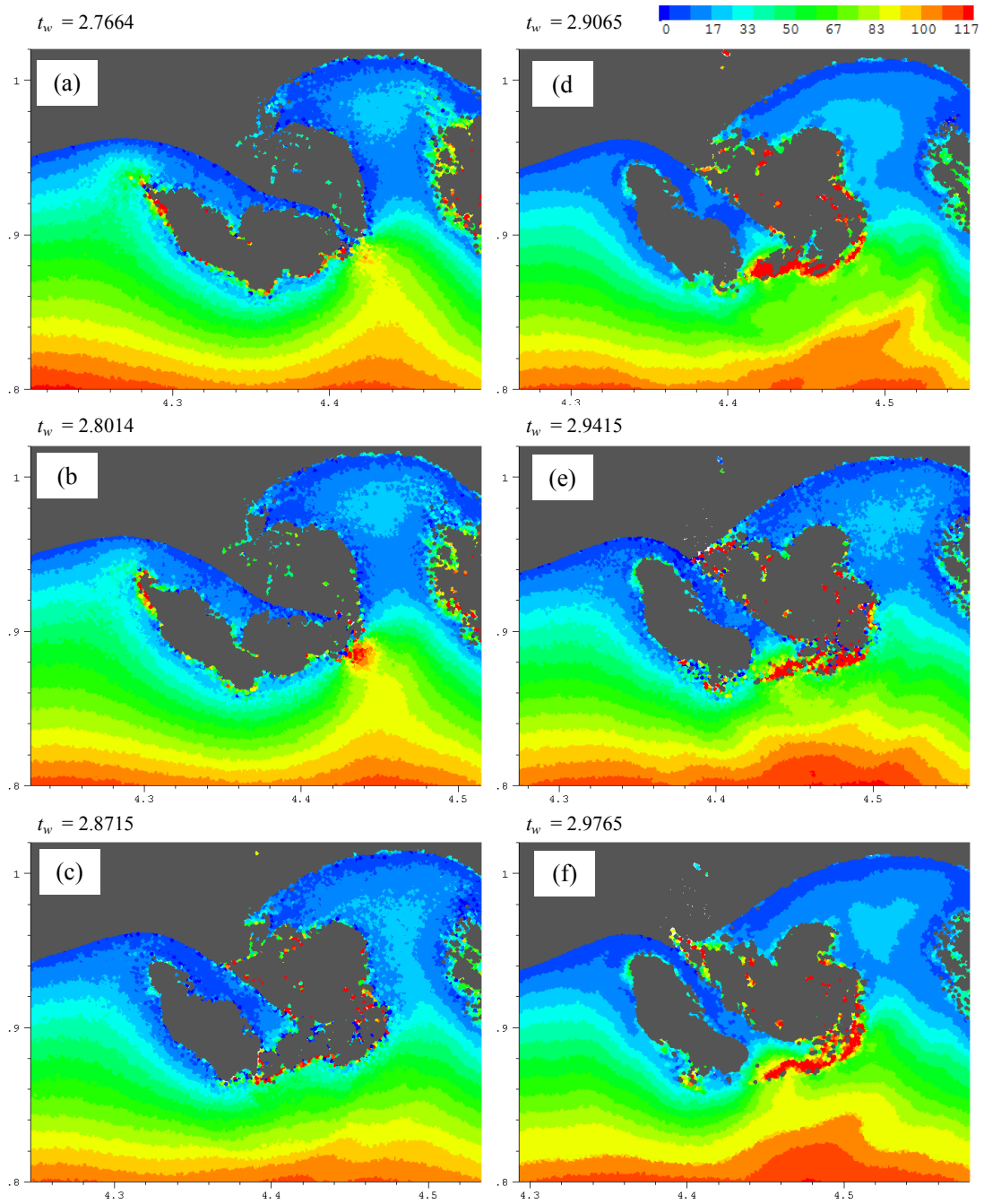
Figure 4.22. Pressure distribution ($p/\rho_0 gD$) in the plunging jet, in the vertical jet and under wave crest during the collapsing of the vertical jet.
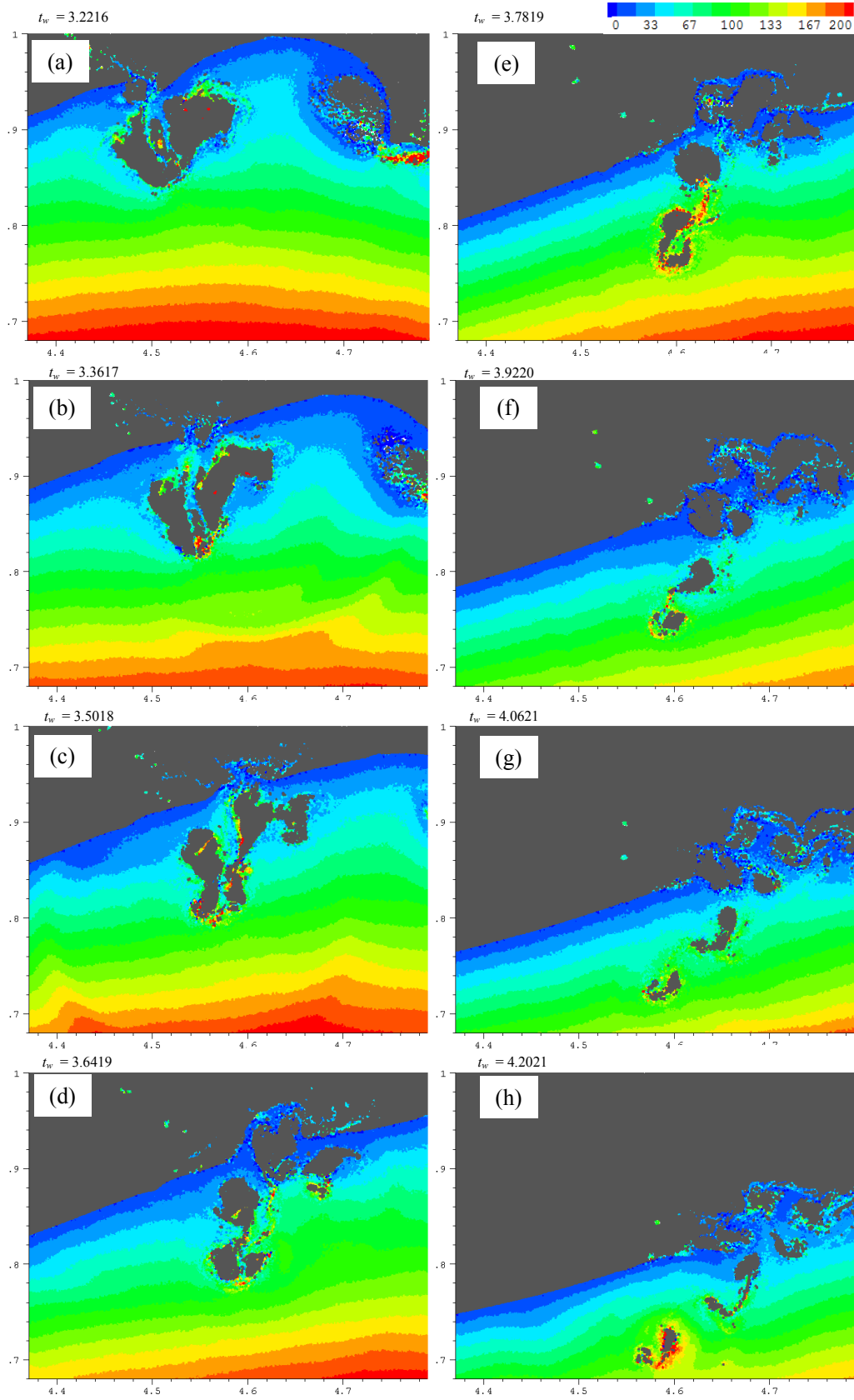
Figure 4.23. Pressure distribution ($p/\rho_0 gD$) in the water column under the breaking wave.
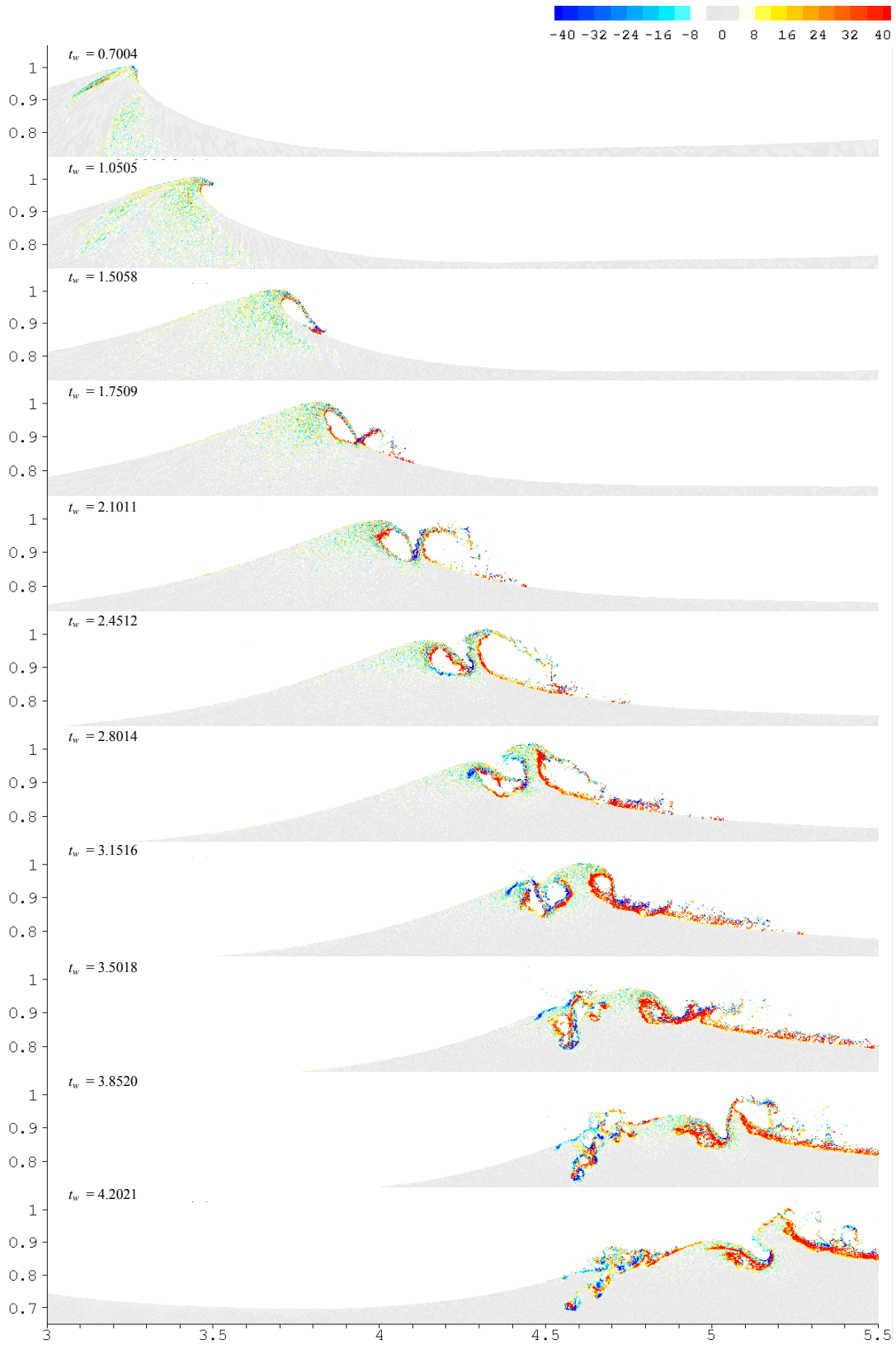
Figure 4.24. Vorticity (s⁻¹) generated in the water column.
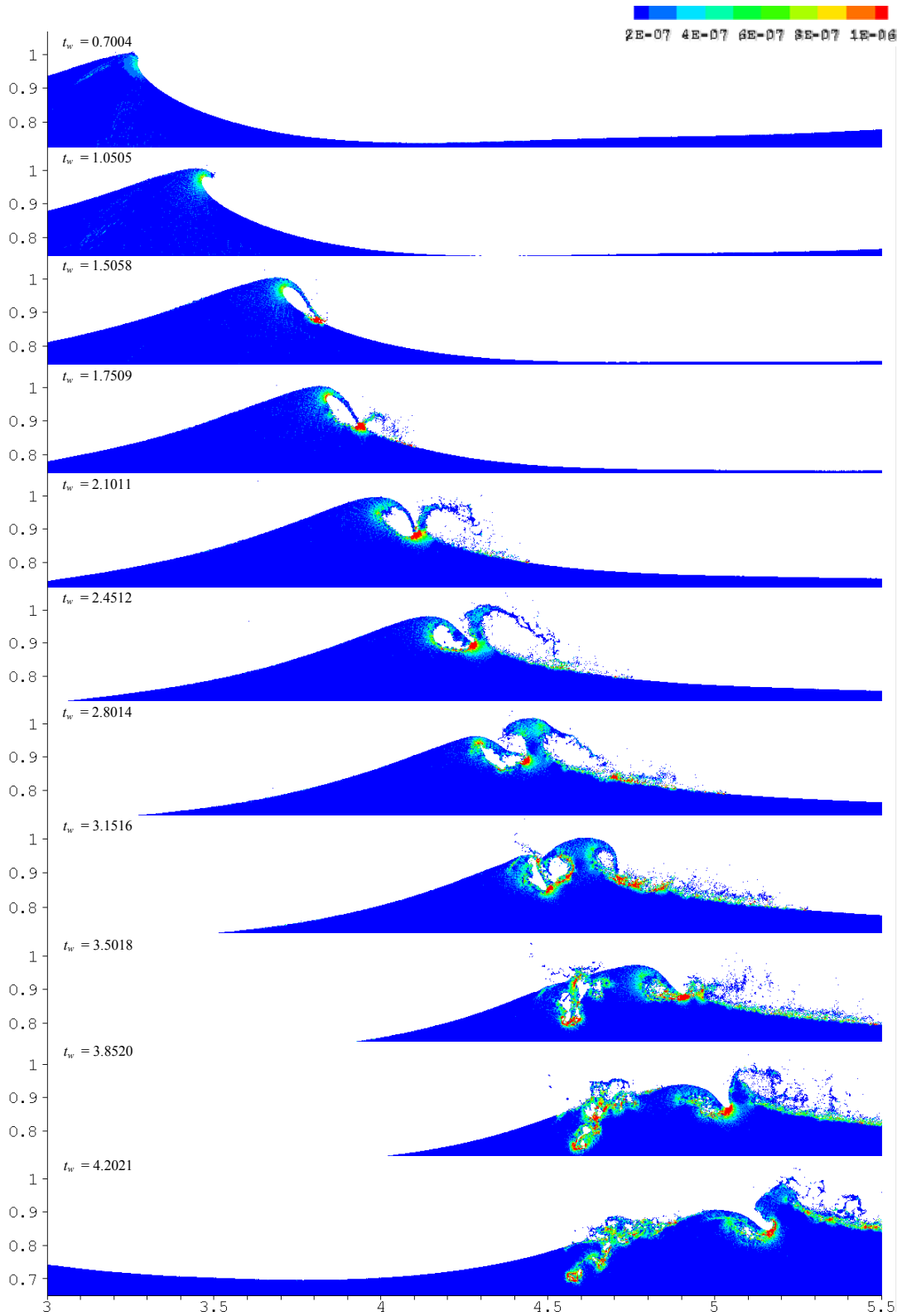
Figure 4.25. Subgrid turbulent kinematic eddy viscosity in water, ν_t (m²s⁻¹)

4.6   3D perspectives of wave plunging

The 3D perspectives of wave plunging photographs presented in Kway (2000) provide valuable benchmarks for verifying the numerical results. Profiles of the breaking wave derived numerically are extracted to create 3D perspectives as shown in Figure 4.26. The projected wave breaking profile is compared with Kway's results the same viewing angles. The projection procedure and comparison of 3D views are shown in Figure 4.26 to Figure 4.28. In this projection, the roughness of the water surface is ignored. Hence the resulted surface of the tube is smooth.
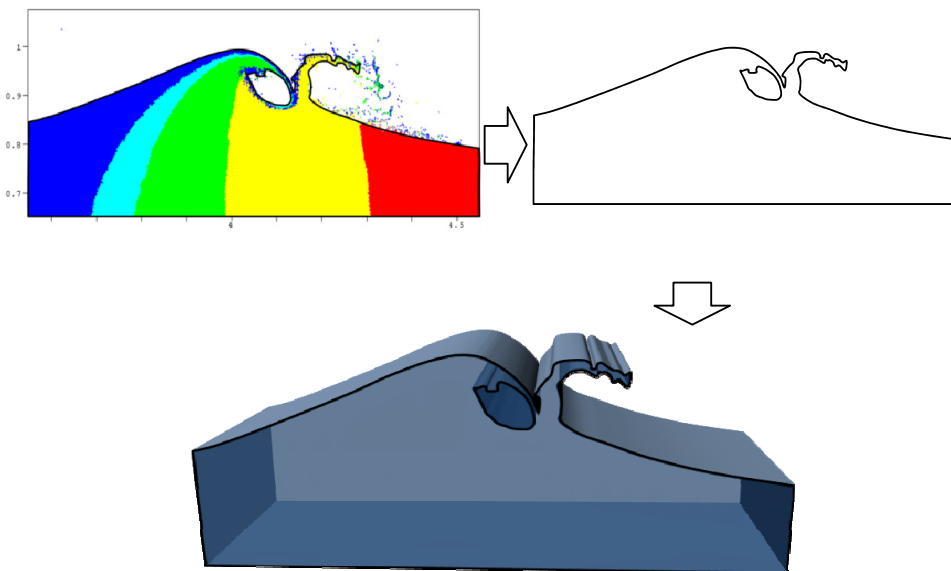
Figure 4.26. 3D projection of a breaking profile of the simulated plunging wave.

The photograph in Figure 4.27b shows a clear wall inside the water column. It was initially suggested that the plunging jet penetrates deeply into the water column, entraining a large amount of air and creating the wall. However, the numerical simulation shows that the plunging jet does not penetrate deeply. When the 3D profile of the simulated wave is created and viewed from the same angle, it is clear that "the wall" is the envelop of the air tube (Figure

4.27a). From another view angle, the 3D profile of the simulated wave also matches very well with the photograph taken from experiment (see Figure 4.28).

Excellent agreements between numerical simulation and experiments are observed in Figure 4.11 to Figure 4.28 which indicates that the SPH model reproduces correctly the highly nonlinear breaking process.
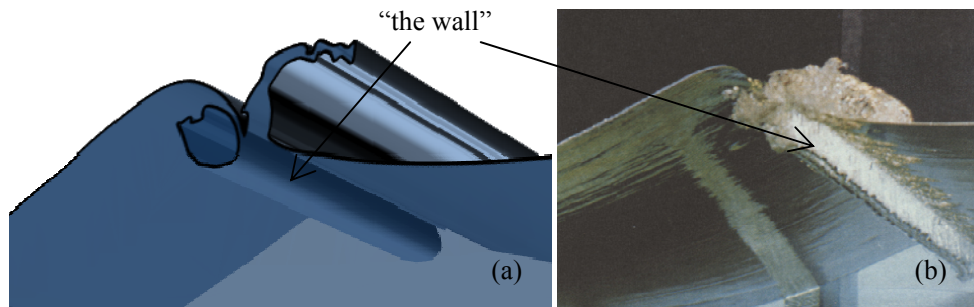
Figure 4.27. The air tube viewed from front, below. (a) 3D projection of the simulated wave, (b) photograph taken from the same viewing angle.
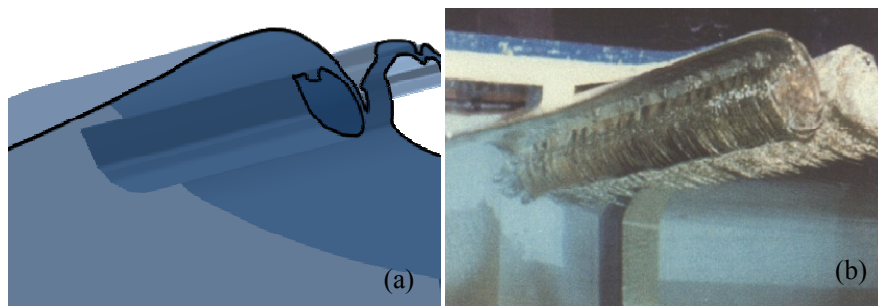
Figure 4.28. The air tube viewed from behind, below. (a) 3D projection of the simulated wave, (b) photograph taken from the same viewing angle.

4.7   Dynamics of the air layer during wave plunging

The circulation of the air above the water is illustrated in Figure 4.29. The colour code in the figure denotes the id of the air particles which is uniquely assigned and fixed for each particle. The air particles are initialized with uniform position and zeros velocity. It is noted that this numerical simulation does not take wind into account. When the wave propagates from

left to right, the strong shear at the interface drives the air particles near the interface to move in the same direction while particles higher above moves lesser. More air particles are carried forward near the wave crest ($t_w = 0.70$). When the wave starts curling over ($t_w = 0.105$), some small eddies are generated above the plunging tip and detached from the interface. The eddies could grow to larger eddies as the one shown in the dashed black circle in Figure 4.29l.
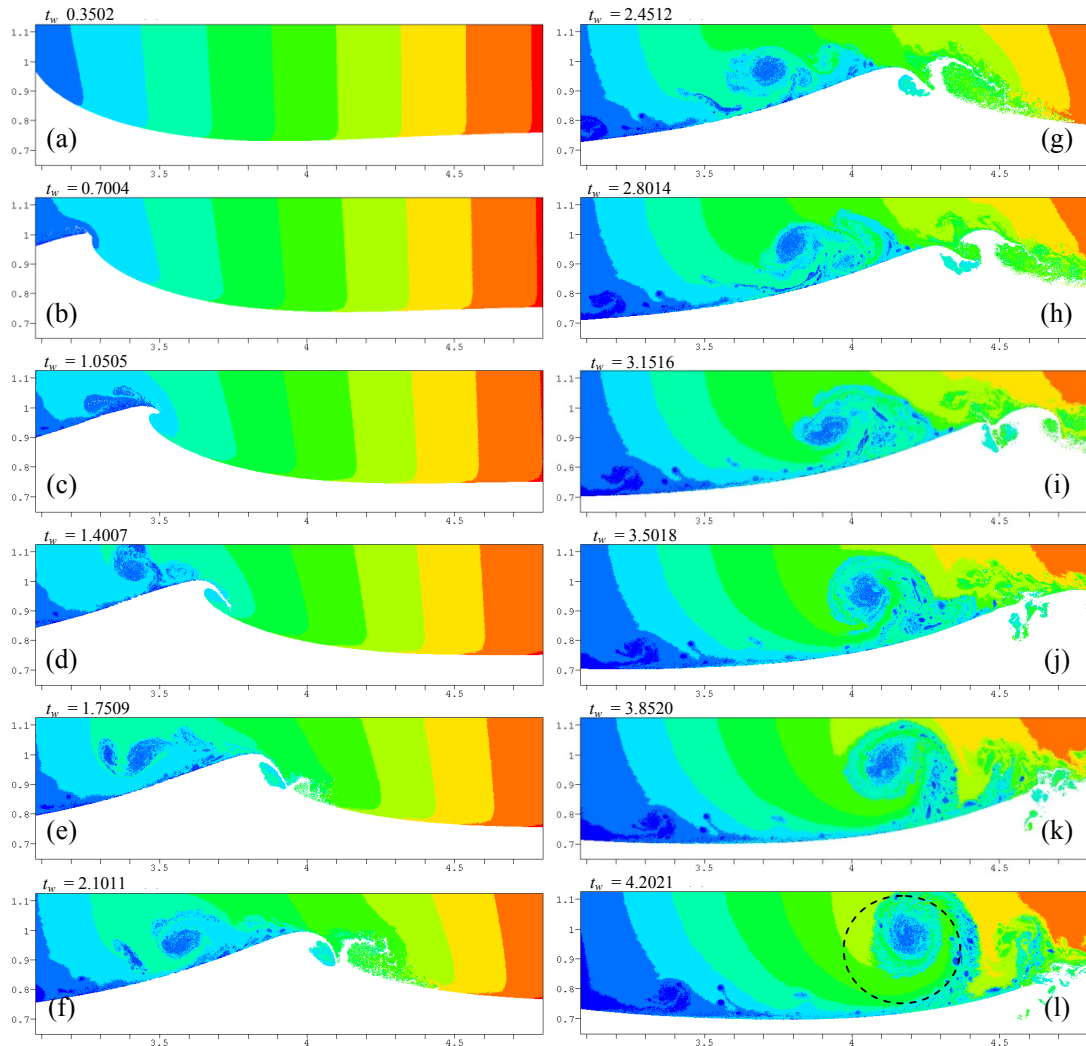
Figure 4.29. Circulation of surrounding air during the wave breaking.

4.8   Importance of air dynamics in wave plunging simulation

In the discussion above, many phenomena are related to the dynamics of air. In order to have better understanding the influences of the air dynamics on the process of wave breaking, the two-phase simulation is compared with a one-phase simulation. In the two simulations, all the numerical settings of the SPH models are the same except that one model does not include the air particles. Snapshots of the two simulations are plotted side by side in Figure 4.30. The color code is the id of water particles which is uniquely assigned and fixed to each particle.

At the time before the impingement of the plunging jet, the shapes of the plunging jets from the two simulations show a little difference: the plunging jet from the single-phase simulation develops faster than that from the two-phase one. The small difference suggests that the air dynamics plays a minor role at this stage except for providing additional drag force which slows down the plunger's development.

After the plunging tip has impinged onto the water in the front, the single-phase simulation shows remarkable reduction of the tube's volume and a quick collapse of the tube. The tube in the single-phase simulation retaining its volume for a short time is probably due to the centrifugal force acting on the surrounding water of the tube when it is rolling. This rolling motion slows down quickly. As a result, the centrifugal force reduces and the tube abruptly collapses.

A significantly different behaviour of the tube is observed in two-phase simulation. The tube in the two-phase simulation maintains its volume for a longer time. The air acts as a cushion, providing pressure in addition to the centrifugal force to hold the tube longer. Once the rolling motion slows down, the centrifugal force reduces and the tube starts to collapse. The collapse of the tube squeezes the air that breaks the water surface. Part of the compressed air then escapes though a gap on the broken surface, contributing to the formation of water

sprays (illustrated in Figure 4.30-right column, t_w = 2.8). The remains of the air tube later break into several bubbles.

There is also a significant difference in the shape of the vertical jet generated by the plunger's impingement. The water particles composing the vertical jet in single-phase simulation seem to be flying freely like marbles. In the two-phase simulation the presence of air produces friction and pressure force on the water surface. The pressure force acting on the front face of the vertical jet in opposite to the wave propagation direction results in the vertical jet being built up vertically and eventually breaking reversely relative to the forward motion of the wave. The impingement of the back flow of the vertical jet onto the coming wave contributes significantly to the subsequent collapsing of the air-tube, additional air entrainment and generation of sprays of water (Bonmarin, 1989). The bifurcation of the vertical jet is not reproduced in the single-phase simulation.

The comparison of the two simulations does indicate the highly important role of the air dynamics in the simulation the breaking process of water wave. Without the presence of air in the simulation, many important physics would be missed. These include the build up and collapse of the vertical jet and the entrapment of the two large air pockets.
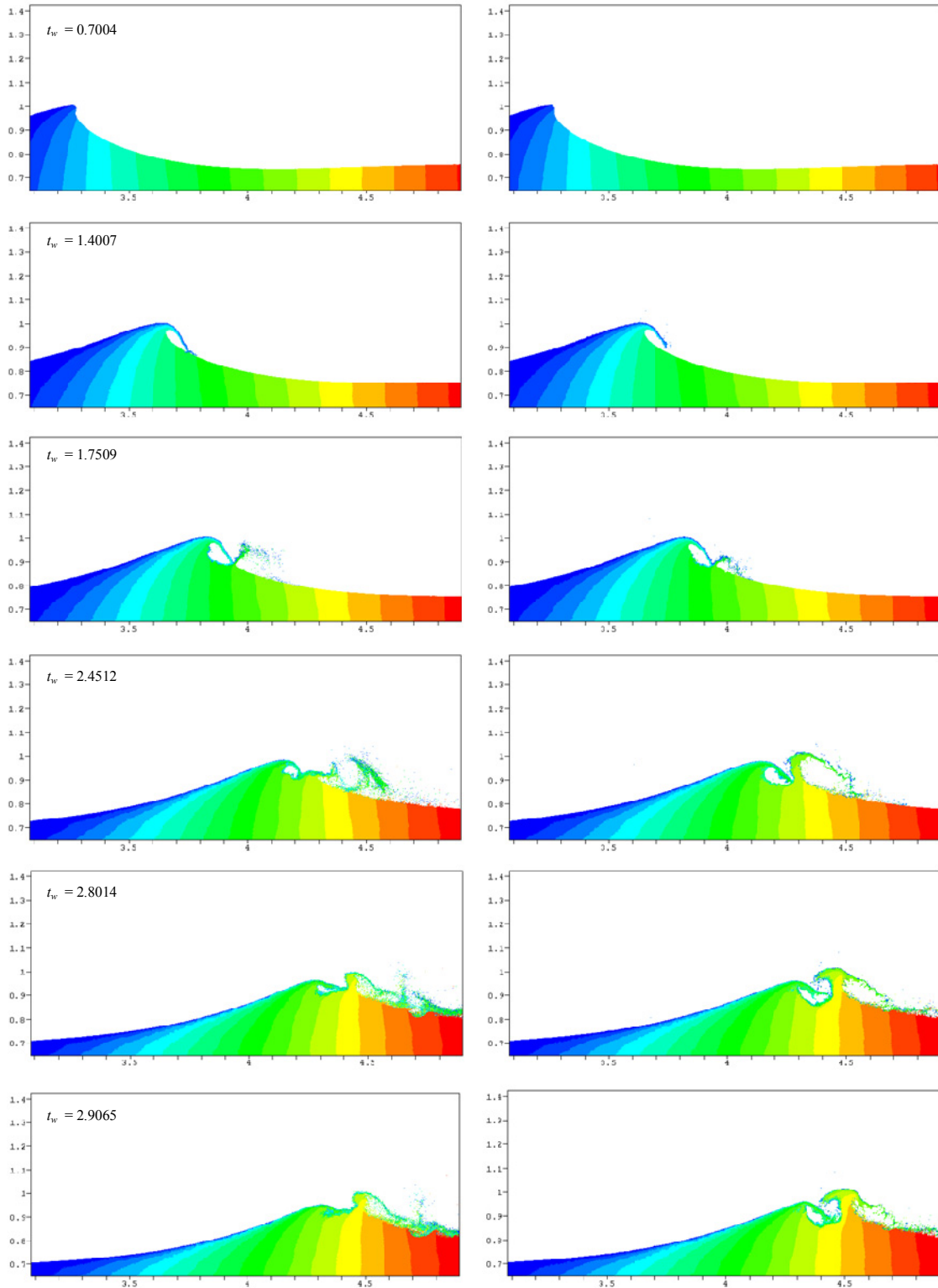
Figure 4.30. Snapshots of wave breaking simulations: without air dynamics (left) and with air dynamics (right). Only water phase is plotted. Color code is particle id.

4.9   Wave energy dissipation

The energy dissipation due the breaking wave is evaluated over a time period of $t_w = 10.5$ since the focal time. As the computation domain is periodic, flow left the domain through the right boundary and entered the domain through the left boundary may interact with the wave and may not reflect the correct pattern of energy dissipation. During the simulation period, the errors, however, are located at thin regions near the two lateral boundaries (see Figure 2.29) and thus is expected to contribute little to the evaluation of wave energy.

The total energy is calculated over all the water particles in the nested domain. We define E_0 to be the energy of all water particles in the nested domain (defined in Section 4.1) when they are at balance positions and rest. In other words, E_0 is the minimum energy of the water in the nested domain. Other definitions of relative potential, kinetic, total energy, initial total energy and energy for normalization are similar as those used in previous chapters. Here, they are normalized by their initial values (computed at the start of the nested simulation).

$$E_P = \frac{E_P - E_0}{E_{P0}} \; ; E_K = \frac{E_K}{E_{K0}}; \; E_T = \frac{E_T - E_0}{E_{T0}} \; ;$$

The time series plots of the normalized energy components are presented in Figure 4.31 together with snapshots of breaking stages at respective times. In this case of plunging breaking about 60% of total energy within the nested domain is kinetic energy.

During the first $\Delta t_w = 1.4$ from the focal time, $t_w = 0$, the total energy is almost conserved. Kinetic energy is transformed to potential energy. The energy decay rate starts to rise after the time $t_w = 1.4$ which is the instance of the plunging jet about to impinge on the water front. When the breaking intensity increases, the decay rate increases. During the first $\Delta t_w = 2.8$ of the studied period of the wave breaking, kinetic energy increases while potential energy decreases. At time $t_w = 2.8$, about 12% of potential energy converted to kinetic energy and dis-

sipated. It results in 5% increase of kinetic energy. After $t_w = 3.5$, when the two large air pockets start to collapse to small bubbles, kinetic energy starts to decrease. The decrease of kinetic energy could be attributed to the kinetic energy partly transforming to potential energy and partly dissipated through the strong turbulence generated during this stage. After $t_w = 4.2$, several cycles of energy transform between kinetic and potential forms are observed. In overall, the total energy keeps decreasing monotonically. About 18% of the total energy contained in the water is dissipated through this period of wave breaking. Similar patterns of energy transformation and dissipation (which are the oscillation of potential and kinetic energies and monotonically dissipation of the total energy) were observed in the experimental study in Rapp (1986) and the numerical study in Lubin (2004).
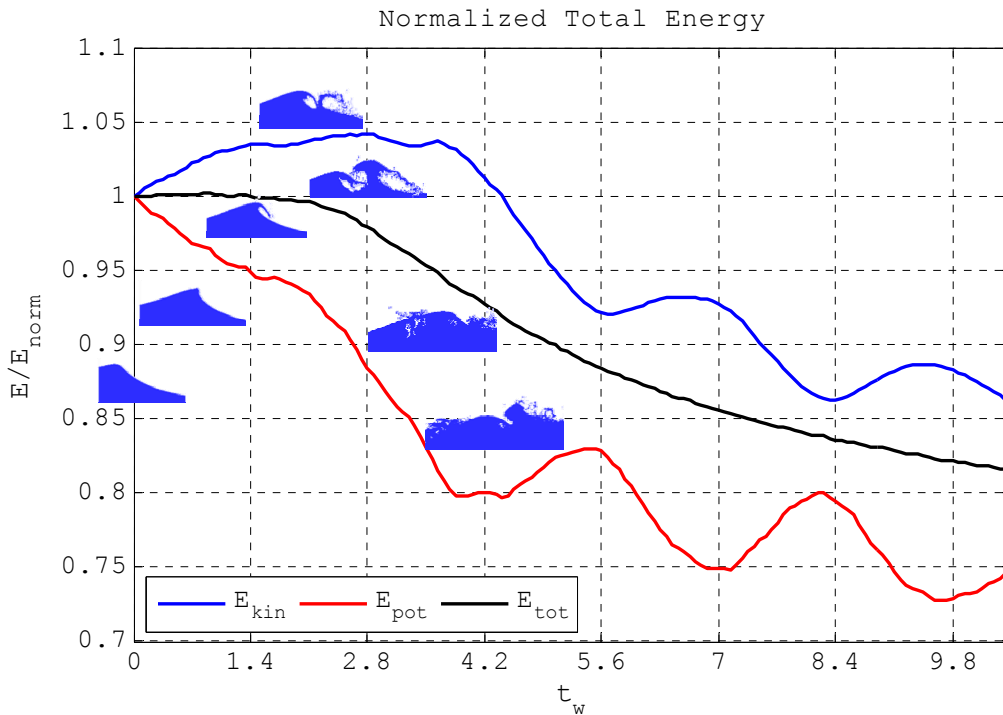
Figure 4.31. Time series of calculated normalized energy components of the water in the nested domain. Snapshots of the breaking stages of the wave are shown at respective times.

Chapter 5. Conclusion

In this thesis, an enhanced Smooth Particle Hydrodynamics (SPH) methodology has been successfully developed to study specific details of wave plunging, air entrapment and turbulent mixing.. The numerical study has led to a deeper understanding of the mechanics of wave plunging, especially in the near-field of the plunging jet. These include the details of the air entrapment process, formation of a secondary vertical jet and its interaction with the plunging jet, evolution and collapse of the entrapped air tube, development of a vertical water spray and the subsequent turbulent mixing in the wake of wave plunging.

5.1   Development of the numerical methodology

The numerical methodology has been developed based on the Smoothed Particle Hydrodynamics methodology developed by Gingold and Monaghan (1977) and Lucy (1977) including the serial code SPHysics v1.0 (http://wiki.manchester.ac.uk/sphysics) for general free surface flows. Significant modifications and enhancements have been developed and incorporated into the SPH model in order to improve its stability, accuracy and ability to simulate a multi-scale complex process at a high resolution. The work includes selective implementations of developments from other researchers, the developments of enhanced "ghost" method, multi-scale nesting and parallel computing by the author, extensive calibration, validation and sensitivity studies to select the key controlling parameters of the SPH model.

An SPH formulation for air-water two-phase flows, similar to that used in Colagrossi and Landrini (2003), was incorporated into the SPH model. The use of this formulation has

helped to reduce the error associated with the large difference in fluid densities at the air-water interface. Enhancements were also made to the XSPH correction for particle velocity and the density regularization considering this large density difference.

A "ghost" particle method was used in the SPH model for the treatment of solid boundaries. Enhancements to the mirror procedure were introduced to improve the consistency of the "ghost" and fluid particles. Using the hydrostatic hypothesis, computations of pressures and densities of the ghost particles took into account accelerations of the fluid counterparts. A formulation for the slip condition at solid boundaries was derived. By using a slip coefficient, the non-slip, full-slip or intermediate-slip condition at the boundaries could be imposed. In addition, different mirror patterns at boundary corners were introduced to maintain the consistency; trajectories of the ghost particles have to be consistent with those of the fluid counterparts. As a result, accuracy of flow near a solid boundary was significantly improved.

Two significant developments successfully introduced are the coding of the methodology for parallel computation and the multi-scale nesting. Through these modifications, the size of the computation domain has been increased to several hundred times larger than a normal simulation in a single computer and the resolution was refined by ten folds.

Numerical simulations of tank sloshing, dam break and wave propagation in a long flume revealed that the high dissipation rate in SPH simulations may be attributed to the low resolution and small smoothing length being used. At high resolutions, and with a careful selection of numerical parameters, the SPH model yields smaller dissipation rates compared with other gridded methods. Results from the benchmarking problems agreed well with those from the Boundary Element Method, analytical solutions and experiments. The use of the parallel SPH model allows the simulation of wave breaking to be conducted at finer resolutions to reduce the numerical dissipation.

At a very high resolution, a simulation of a two-phase wave breaking in a full laboratory-scale water flume could involve hundreds of millions of particles. Thus, it is impractical even if the parallel SPH model on hundreds of processors is used. The one-way nesting procedure introduced, therefore, has enabled the simulation of a two-phase flow wave breaking process at high resolution. The nesting procedure was implemented in the SPH model through two steps. The wave generation and propagation in a long water flume were simulated at a coarse resolution. This simulation was performed until the wave starts to break. At this stage, a smaller domain that covers the breaking area was extracted from the coarser simulation in the first step. A much finer resolution was used for the simulation of identified domain.   The initial condition of the water was interpolated from the coarser simulation. The area above the water surface was filled up by a layer of air. Initial gauge pressure and velocity of the air layer were set to zero. Air velocity near the interface with water was extrapolated from the velocity of the water to reduce the inconsistency. The nested domain was then simulated with a periodic boundary condition applied at its lateral boundaries. The procedure has proven to be effective and accurate, evident in the comparison between simulated results and experimental measurements.

The calibration, validation and sensitivity studies of the SPH model have been conducted using well-known benchmark problems. The chosen benchmark problems include sloshing in an enclosed tank, dynamics of a high pressure air bubble rising in water, dam break with impact on a vertical wall, and wave propagation in a flume. The numerical results converge to the analytical solutions as the resolution increases. The studies also showed that, at a given resolution dx, the smoothing length, $hc = h/dx$, should be in the range of 1.55 to 2.05. The computational time step dt satisfies the Courant number, $Cr = max(c_s) \times dt/dx < 0.2$. The suitable numerical sound speed (c_s) in water is around 20 m/s and the suitable numerical sound speed in air is in the range of 20 – 40 m/s.

Through the above modifications and enhancements, the SPH methodology was able to reproduce accurately the results obtained in a laboratory simulation of wave plunging.

5.2   Numerical simulation and analysis of the plunging wave breaking

The evolution of a frequency and amplitude modulated wave packet leading to a plunging wave, studied in substantial details by Kway (2000) and Lim (2001) in laboratory experiments, has been successfully simulated using the numerical wave tank developed in this thesis. The length of the wave flume is 30 m. The input signal to the wave paddle in the SPH model has been derived from the prescribed input signal to the wave paddle used in the laboratory experiment conducted by Kway (2000). The signal comprises 28 wave components with frequencies in the range of 0.56 Hz to 1.1 Hz and designed to generate a wave that would break at a distance of 15.2 m from the paddle mean position after 26 seconds. The simulation of the entire wave tank is performed at with a resolution of 0.005 m. The nested inner domain, 7.6 m long and 2.4 m high (including the air layer), is simulated with a resolution of 0.001 m.

The degrees of asymmetry of the simulated plunging wave are compared with the values derived and classified by Bonmarin (1989). The results suggest that the simulated plunging wave may be classified as a strong plunging wave. At the initial stage of wave plunging, water particles near the wave front typically flow backwards relative to the wave crest. When the crest steepens further to form a vertical wave front, the upward movement of water particles (relative to the crest) bifurcates at the top of the wave crest. A part of the upward flowing water particles on the wave front moves forward at the crest, creating the plunging jet. The plunging jet projects forward and curls towards the water surface on the wave front. Relative to the wave crest, the water particles on the wave front and the plunging jet clearly develop a well-defined vortex that "rolls" forward along with the crest.

Water acceleration at most parts of the plunging jet is about 1g and pointing downwards, suggesting that water particles within the plunging jet fall freely due to gravity. At the curved part of the inner face of the plunging jet, accelerations are much higher with magnitudes exceeding 4g. This is probably due to the centrifugal force acting on the circulating water mass on the inner surface of the wave front enclosed by the plunging jet. The obtained results agree fairly well with those derived using the Boundary Integral Method in Lim (2001).

The process of plunging jet also leads to a characteristic air entrapment. The tube of entrapped air has the shape of an inclined and elongated ellipse. The surface of the tube is initially smooth except for some roughness near the contact region between the tip of the plunging jet and the wave front. The disturbances originate from the collision of the plunging tip and the water surface. These features "roll" up the wave front, consistent with circulation of the water particles on the surface of the entrapped air tube. The tube changes its shape when rolling forward and the entrapped air in the tube goes through compression and decompression. These results are consistent with the observations in the experiments by Kway (2000). The pressure support from the air tube and the centrifugal force due to the circulation of the water perhaps are the main factors for the tube to persist while rolling forwards with the wave. When wave plunging progresses further, the plunging jet becomes thinner and weakens. A gap opens near the base of the air tube and a part of the entrapped air quickly "squirts" out through the gap at a speed as large as three times of the wave speed. With the release of entrapped air, the volume of the air tube and its pressure reduce substantially.

Based on the numerical results, it is clear that the plunging jet will not penetrate deeply into the water column. While part of the plunging jet splashes forward, part of it moves along with the water particles on the original wave front to continue form the air tube and rolls forward accordingly. Due to the inclined impingement, however, part of the water mass from the wave front is pushed forward, en-massed with the water particles from the plunging jet to

form a vertical jet. The vertical jet comprises of water mainly from the water front and, to a smaller extent, from the plunging jet. The jet could rise as high as the original wave crest before collapsing. A characteristic vertical water spray, earlier observed in Kway (2000) appears to be due to the interaction between the tip of the vertical jet and the plunging jet and in conjunction with the release of the entrapped air. The numerical results show that that water particles could attain a vertical speed of around a half of the wave speed.

The presence of the vertical jet ahead of the plunging jet also leads to the formation of a second air pocket of comparable volume compared to the collapsed entrapped air tube. The two air pockets, however, appear to be rotating in opposite directions and broken into smaller bubbles in the water column. Larger bubbles quickly rise to water surface rapidly, releasing air and creating a foamy surface. Smaller bubbles are entrained deeper into water column due to the counter-spinning vortices associated with the two phase fluid. The spinning bubbles could be carried as deep as half a wave height into the water column. As the study has been conducted using a two dimensional model, the numerical results is not able to yield any three dimensional features that may be formed. Given the fact that the vertical jet, in a real three dimensional scenario, is likely to be uneven in the lateral direction, the entrapped air formed between the plunging jet and the vertical jet is likely to be in the form of larger air pockets rather than an air tube. The breakdown into bubbles at this stage of the plunging is also evident in the experimental results obtained by Kway (2000).

Based on the analysis of the energy dissipation associated with the wave plunging process, it is clear that a significant proportion of the wave energy is lost during wave breaking. The numerical results are similar to those observed earlier in experimental studies conducted by Rapp (1986) and in numerical studies conducted by Lubin (2004). While the total wave energy decreases monotonically, the kinetic and potential energy oscillated as observed in earlier experiments. During plunging and prior to jet impingement, a significant portion of the

wave potential energy is converted into kinetic energy. While part of the wave energy is imparted into the air flows and water sprays generated by the breaking wave, part of the energy is also dissipated through the turbulent mixing generated in the water column.

In this thesis, a numerical methodology based on SPH has been successfully developed to capture the essential physics of the wave plunging process. It is evident that a two-phase simulation is necessary, especially for the modelling of the entrapped air dynamics. Up to the stage before jet impingement, air dynamics would have a minor role and a one-phase simulation would have been adequate. However, this would not be true for the complex process after jet impingement. Before the impingement of the plunging jet, the air dynamics only played a minor role. After the plunging tip had impinged onto water in the front, the entrapped air tube provided pressure in addition to the centrifugal force of the circulating water mass to hold the tube longer. The thesis has also shown that the enhanced SPH methodology, coupled with multi-scale nesting and coding for parallel computing, is able to model the finer details of the complex breaking process.

Although it is not done in the thesis, the methodology could be easily extended to three dimensional simulations, hence enabling the simulation even more complex features of the complex process. An obvious advantage of the SPH model is its ability to capture the details of flow within the water mass. With the expected improvement in computing resources, the extension into a detailed simulation of 3D features would indeed be feasible. For a deeper understanding of energy dissipation through wave breaking, future studies could also focus on different breaking intensities. An extension to understand the physics of wave impacts on offshore structures is now being pursued by a fellow student.

Reference

Abadie S., 2001. Numerical modelling of the flow generated by plunging breakers. Proceedings Coastal Dynamics 2001, pp. 202-211.

Autodyn, http://www.ansys.com/Products/autodyn.asp

Batchelor G.K., 1967. An Introduction to Fluid Dynamics. Cambridge University Press. ISBN 0521663962.

Bate M.R., Bonnell I.A. and Price N.M., 1995. Modelling accretion in protobinary systems. Monthly Notices of the Royal Astronomical Society, 277, 362-76

Bate M.R., Bonnell I.A. and Bromm V., 2003. The formation of a star cluster predicting the properties of stars and Brown Dwarfs. Monthly Notices of the Royal Astronomical Society, 399, 577-99

Battjes J.A., 1988. Surf-zone dynamics. Annual Review Fluid Mechanics, vol. 20, p. 257-293.

Belytschko T., Krongauz Y., Organ D. and Gerlack G., 1998. On the completeness of meshfree particle methods. International Journal for Numerical Methods in Engineering, vol. 43, No.5, p. 785-819

Benz W., 1990. Smooth particle hydrodynamics: a review. In: J.R. Buchler (Ed.), The Numerical Modelling of Nonlinear Stellar Pulsation, Kluwer Academinc Publishers, Dordrecht, p. 269-288.

Benz W. and Asphaug E., 1994. Impact simulations with fracture: I. Method and tests. Icarus, 1233, 98-116.

Benz W. and Asphaug E., 1995. Simulations of brittle solids using smoothed particle hydrodynamics. Computer Physics Communications, 87, 253-65

Benz W., Slattery W.L. and Cameron A.G.W., 1986. The origin of the moon and the single impact hypothesis, Icarus, 66, 515-35.

Biausser B., Grilli S.T., Fraunie P., Marcer R., 2004. Numerical analysis of the internal kinematics and dynamics of three-dimensional breaking waves on slopes. International Journal of Offshore and Polar Engineering, 14 (4), 247-256.

Boneva L.I., Kendall D. and Stepanov I., 1971. Spline transformations: three new diagnostic aids for statistical data analysis. Journal of the Royal Statistical Society, Series B (Methodological), vol. 33, no. 1, p. 1-71

Bonmarin P., 1989. Geometric properties of deep-water breaking waves. Journal of Fluid Mechanics, 209, 405-433.

Bradford S.F., 2000. Numerical simulation of surf zone dynamics. Journal of Waterway, Port, Coastal, and Ocean Engineering, 126 (1), 1-13.

Chan ES and Melville WK, 1988. Deep water plunging wave pressures on a vertical plane wall. Proceeding of the Royal Society A417, 95-131.

Chanson H., Lee J.-F., 1997. Plunging jet characteristics of plunging breakers. Coastal Engineering, 31, 125-141.

Chanson H., Aoki S., Maruyama M., 2002. Unsteady air bubble entrainment and detrainment at a plunging breaker, dominant time scales and similarity of water level variations. Coastal Engineering, 46, 139-157.

Chen G., Kharif C., Zaleski S., Li J.J., 1999. Two-dimensional Navier-Stokes simulation of breaking waves. Physics of Fluids, 11, 121-133.

Christensen E.D., 1996. Large eddy simulation of breaking waves. Coastal Engineering, vol. 42, no. 1, p. 53-86.

Christensen E.D., Deigaard R., 2001. Large eddy simulation of breaking waves. Coastal Engineering, 42, 53-86.

Cleary P.W., 1998. Modelling confined multi-material heat and mass flows using SPH Applied Mathematical Modelling, 22, 981-993.

Cleary P.W. and Ha J., 2002. Flow modelling in casting processes. Applied Mathematical Modelling, 26, 171-190.

Cokelet E.D., 1977. Breaking waves. Nature, 267, 769-774.

Colagrossi A., 2004. A meshless Lagrangian method for free-surface and interface flows with fragmentation PhD. Thesis at Universita di Roma, La Sapienza.

Colagrossi A. and Landrini M., 2003. Numerical simulation of interfacial flows by Smoothed Particle Hydrodynamics. Journal of Computational Physics, vol. 191, p. 448-475.

Crespo A.J.C., Gómez- Gesteira M. and Dalrymple R.A., 2007. Boundary conditions generated by dynamic particles in SPH methods. Computers, materials and continua, 5(3): 173-184.

Dommermuth D.G, Yue D.K.P., Lin W.M., Rapp R.J., Chan E.S. and Melville W.K., 1988. Deep-water plunging breakers a comparison between potential theory and experiments. Journal of fluid mechanics, 189: 423-442.

Lo E.Y.M. and Shao S.D., 2002. Simulation of near-shore solitary wave mechanics by an incompressible SPH method. Applied Ocean Research (2002), vol. 24, no.5, p. 275-286.

Galvin C.J., 1968. Breaker type classification on three laboratory beaches. Journal of Geophysical Research, 73, 3651-3659.

Gingold R.A. and Monaghan J.J., 1977. Smoothed particle hydrodynamics: theory and application to non-spherical stars. Monthly Notices of the Royal Astronomical Society, 181, 375-389.

Gotoh H. and Sakai T., 2006. Key issues in the particle method for computation of wave breaking. Coastal Engineering , vol. 53, p. 171-179.

Gotoh H., Shibahara T., and Sakai T., 2001. Sub-particle-scale turbulence model for the MPS method-Lagrangian flow model for hydraulic engineering. Computational Fluid Dynamics Journal, 9(4), 339-347.

Gotoh H., Sakai T., Hayashi M. and Andoh S., 2002. Lagrangian solid-liquid two-phase flow model wave-seabed interaction. Proceeding of the 13th IAHR-APD Congress, Singapore, p. 765-770.

Goroth H., Shao S.D., and Memita T., 2004. SPH-LES model for numerical investigation of wave interaction with partially immersed breakwater. Coastal Engineering Journal, 46(1):39-63

Gotoh H., Ikari H., Memita T., and Sakai T., 2005a. Lagrangian Particle Method for Simulation of Wave Overtopping on a Vertical Seawall. Coastal Engineering Journal, Vol. 47, Nos. 2 & 3, pp. 157-181.

Gotoh H., Ikari H. and Sakai T., 2005b. Development of numerical wave flume by 3D MPS method. Ocean Waves Measurement and Analysis, Fifth International Symposium WAVES 2005, 3rd-7th, July, 2005. Madrid, Spain, p. 196

Gray J.A. and Monaghan J.J., 2004. Numerical modelling of stress fields and fracture around magma chambers. Journal of Volcanology and Geothermal Research, 135, 259-283.

Gray J.A., Monaghan J.J. and Swift R.P., 2001. SPH elastic dynamics. Computer Methods in Applied Mechanics and Engineering, 190, 6641-6662.

Greenhow M., 1983. Free-surface flows related to breaking waves. Journal of Fluid Mechanics, 134: 259-275

Grilli S.T., Svendsen I.A., and Subramanya R., 1997. Breaking criterion and characteristics for solitary waves on slopes. Journal of Waterway, Port, Coastal, and Ocean Engineering, 123, p. 102-112.

Grilli S.T., Guyenne P., and Dias F., 2001. A fully non-linear model for three-dimensional overturning waves over an arbitrary bottom. International Journal for Numerical Methods in Fluids, vol. 35, no. 7, p. 829-867.

Guignard S., Marcer R., Rey C., Kharif V., Fraunié P., 2001. Solitary wave breaking on sloping beaches: 2-d two phase flow numerical simulation by sl-vof method. European Journal of Mechanics-B: Fluids, 20, 57-74.

Gutfraind R., Savage S.B., 1998. Flow of fracture ice through wedge-shaped channels: smoothed particle hydrodynamics and discrete-element simulations. Mechanics of Materials, 28, 1-17.

Hieu P.D., Katsutoshi T., Ca V.T., 2004. Numerical simulation of breaking waves using a two-phase flow model. Applied Mathematical Modelling, 28 (11), 983-1005.

Hirt C.W., Nichols B.D., 1981. Volume of fluid (vof) methods for the dynamics of free boundaries. Journal of Computational Physics, 39, 201-255.

Iafrati A., Campana E.F., 2003. A domain decomposition approach to compute wave breaking (wave breaking flows). International Journal of Numerical Methods in Fluids, 41, 419-445.

Iafrati A., Di Mascio A., Campana E.F., 2001. A level set technique applied to unsteady free surface flows. International Journal of Numerical Methods in Fluids, 35, 281-297.

Johnson G.R., Stryk R.A. and Beissel S.R., 1996. SPH for high velocity impact computations. Computer Methods in Applied Mechanics and Engineering, 139, 347-373.

Khayyer A. and Gotoh H., 2007. Applicability of MPS method to breaking and post-breaking of solitary waves. Annual Journal of Hydraulic Engineering, JSCE, vol.51.

Khayyer A., Gotoh H., and Shao S.D., 2008. Corrected Incompressible SPH method for accurate water-surface tracking in breaking waves. Coastal Engineering, 55, 236-250.

Koshizuka S., Nobe A., and Oka Y., 1998. Numerical analysis of breaking waves using the moving particle semi-implicit method Int. International Journal for Numerical Methods in Fluids, vol. 26, p. 751-769.

Kway J.H.L, 2000. Kinematics and dynamics of deep-water wave breaking. Ph.D. thesis at the National University of Singapore.

Lemos C.M., 1992. Wave breaking: A Numerical Study. Lecture Notes in Engineering, vol. 71, Springer Verlag.

Li Y., 2000. Tsunamis: Non-breaking and breaking solitary wave run-up. Rep. KH-R-60, W.M. Keck Laboratory of Hydraulics and Water Resources, California Institute of Technology, Pasadena, CA.

Li Y. and Raichlen F., 2003. Energy balance model for breaking solitary wave runup. Journal of Waterways, Ports, Coastal, and Ocean Engineering, vol. 129(2), p. 47-59

Libersky L., Petschek A.G., 1991. Smooth particle hydrodynamics with strength of materials. In: Trease, Fritts, Crowley (Eds.), Lecture notes in physics 395: Advances in Free Lagrange Methods. Springer-Verlag, p. 248-257.

Lim W.L., 2001. Two Dimensional Simulation of Plunging Waves. B.Eng. thesis at National University of Singapore.

Lin P.Z and Li C.W., 2002. A s-coordinate three-dimensional numerical model for surface wave propagation. International Journal for Numerical Methods in Fluids, 38:1045-1068.

Lin P., Liu P.L.-F., 1998. A numerical study of breaking waves in the surf zone. Journal of Fluid Mechanics, 359, 239-264.

Liu G.R. and Liu M.B., 2003. Smoothed particle hydrodynamics: a meshfree particle method, World Scientific.

Liu M.B., Liu G.R., Zong Z. and Lam K.Y., 2003. Smoothed particle hydrodynamics for numerical simulation of underwater explosions. Computational Mechanics, 30(2):106-118.

Longuet-Higgins M.S., 1969. On wave breaking and the equilibrium spectrum of wind-generated waves. Proceedings of the Royal Society of London, A310, 151-159.

Longuet-Higgins M.S., 1982. Parametric solutions for breaking waves. Journal of Fluid Mechanics, 121, 403-424.

Longuet-Higgins M.S. and Cokelet E.D., 1976. The Deformation of Steep Surface Waves on Water. I. A Numerical Method of Computation. Proceedings of the Royal Society of London. Series A, Mathematical and Physical Sciences, vol. 350, iss.1660, p. 1-26.

Lubin P., 2004. Large Eddy Simulation of plunging breaking waves. PhD thesis at the Université Bordeaux I, in English.

Lubin P., Vincent S., Abadie S., Caltagirone, J.-P., 2003. Three-dimensional Large Eddy Simulation of air entrainment under plunging breaking waves. Coastal Engineering, 53, 631-655.

Lucy L.B., 1977. A numerical approach to the testing of the fission hypothesis Astronomical Journal, 82, 1013-1024.

Michel P., Benz W. and Richardson D., 2004. Catastrophic disruption of asteroids and family formation: a review of numerical simulations, including both fragmentation and gravitational reaccumulation. Planetary and Space Science, 52, 1109-1117.

Miller R.L., 1976. Role of vortices in surf zone predictions: sedimentation and wave forces. Chapter 24 In: Davis, R.A., Ethington, R.L. (Eds.), Special Publication-Society of Economic Paleontologists and Mineralogists, pp. 92-114.

Monaghan J.J., 1989. On the problem of penetration in particle methods. Journal of Computational Physics, 82, 1-15

Monaghan J.J., 1992. Smoothed Particle Hydrodynamics. Annual Review of Astronomy and Astrophysics, vol. 30, p. 543-574.

Monaghan J.J., 1994. Simulating free surface flows with SPH. Journal of Computational Physics, 110, 399-406

Monaghan J.J., 2005. Smoothed Particle Hydrodynamics. Reports on Progress in Physics, vol. 68, p. 1703-1759.

Monaghan J.J. and Gingold R.A., 1983. Shock simulation by the particle method SPH. Juornal of Computational Physics, 52, 374-389.

Monaghan J.J. and Kocharyan A., 1995. SPH simulation of multi-phase flow. Computer Physics Communications, 87, 225-235.

Monaghan J.J. and Kos A., 1999. Solitary waves on a Cretan beach Journal of Waterways, Port, Coastal, and Ocean Engineering, 1111, 145-54

Monaghan, J.J. and Lattanzio J.C., 1991. A simulation of the collapse and fragmentation of cooling molecular clouds. Astrophysical Journal, Part 1 (ISSN 0004-637X), vol. 375, p. 177-189.

Morris J.P., Fox P.J., and Zhu Y., 1997. Modeling low Reynolds number incompressible flows using SPH, Journal of Computational Physics, 136, 214-226.

Muller M., Schirm S., Teschner M., 2004. Interactive blood simulation for virtual surgery based on Smoothed Particle Hydrodynamics. Technology and Health Care, vol. 12, iss. 1, p. 25-31.

Mutsuda H., Yasuda T., 2000. Numerical simulation of turbulent air-water mixing layer within surf-zone. Proceeding of the 27th International Conference on Coastal Engineering, pp. 755-768.

Nadaoka K., Kondoh T., 1982. Laboratory measurements of velocity field structure in the surf zone by lDV. Coastal Engineering Japan, 25, 125-145.

New A.L., 1983. A class of elliptical free-surface flows. Journal of Fluid Mechanics, 130, 219-239

Oger L. and Savage S.B., 1999. Smoothed particle hydrodynamics for cohesive grains. Computer Methods in Applied Mechanics and Engineering, 180 (1-2), 169-183.

Parzen E., 1962. On estimations of a probability density and mode. The Annals of Mathematical Statistics, 33, 1065-1076.

Peregrine D.H., 1983. Breaking waves on beaches. Annual Review of Fluid Mechanics, 15, 149-178.

Peregrine D.H. and Thais L., 1996. The effect of entrained air in violent water impacts. Journal of Fluid Mechanics, vol. 325, p. 377-397.

Peregrine D.H., Cokelet E.D., and Melver P., 1980. The Fluid Mechanics of Waves Approaching Breaking. Proceeding of the 17th International Conference on Coastal Engineering, ASCE, p. 512-528.

Randles P.W. and Libersky L., 1996. Smoothed particle hydrodynamics some recent improvements and applications. Computer Methods in Applied Mechanics and Engineering, 139, 375-408.

Rapp J.R., 1986. Laboratory measurement of deep water breaking waves. Ph.D. thesis at the Massachusetts Institute of Technology.

Rosenblatt M., 1956. Remarks on some nonparametric estimates of a density function. The Annals of Mathematical Statistics, 27. 832-837.

Rosswog S. and Davies M.B., 2002. High resolution calculations of merging neutron stars-I. Model description and hydrodynamic evolution Monthly Notices of the Royal Astronomical Society, 334, 481-497.

Sakai T., Mizutani T., Tanaka H., Tada Y., 1986. Vortex formation in plunging breaker. Proceeding of ICCE, p. 711-723.

Reference

Schoenberg I.J., 1946. Contributions to the problem of approximation of equidistant data by analytic functions: part A. Quarterly of Applied Mathematics, IV, 45-99

Song C., Sirviente A.I., 2004. A numerical study of breaking waves. Physics of Fluids, 16 (7), 2649-2667.

Sussman, M., Smereka, P., & Osher, S. 1994. A level set method for computing solutions to incompressible two-phase flow. J. Comput. Phys. 114, 146.

Fang J., Owens R.G., Tacher L., Parriaux A., 2006. A numerical study of the SPH method for simulating transient viscoelastic free surface flows. Journal of Non-Newtonian Fluid Mechanics, 139, 68-84

Takikawa K., Yamada F., Matsumoto K., 1997. Internal characteristics and numerical analysis of plunging breaker on a slope. Coastal Engineering, 31 (1-4), 143-161.

Verlet, L., 1967. Computer experiments on classical fluids. I. Thermodynamical properties of Lennard-Jones molecules. Physical Review, 159: 98-103.

Watanabe Y., Saeki H., 1999. Three-dimensional large eddy simulation of breaking waves. Coastal Engineering Japan, 41 (2), 281-301.

Watanabe Y., Saeki H., 2002. Velocity field after wave breaking. International Journal for Numerical Methods in Fluids, 39, 607-637.

Zhao Q., Tanimoto K., 1998. Numerical simulation of breaking waves by large eddy simulation and vof method. Proceeding of the 26th International Conference on Coastal Engineering, vol. 1. ASCE, p. 892-905.

Zhao Q., Armfield S., Tanimoto K., 2004. Numerical simulation of breaking waves by multi-scale turbulence model. Coastal Engineering, 51, 53-80.

Zhu Y. and Fox P.J., 2001. Smoothed Particle Hydrodynamics Model for Diffusion through Porous Media. Transport in Porous Meidia, vol. 43, no. 3, p. 1573-1634

Zhou Z.Q., De Kat J.O., Buchner B., 1999. A nonlinear 3-D approach to simulate green water dynamics on deck, in: J. Piquet (Ed.), Proceedings of the 7th International Conference on Numerical Ship Hydrodynamics, Nantes, pp. 5.1-1, 15.